AgRISTARS

E83-10020

NASA-CR-167748

SM-K2-04356

A Joint Program for
Agriculture and
Resources Inventory
Surveys Through
Aerospace
Remote Sensing

Soil Moisture

August 1982

ASSESSMENT OF RADAR RESOLUTION REQUIREMENTS FOR SOIL MOISTURE ESTIMATION FROM SIMULATED SATELLITE IMAGERY

M. C. Dobson, F. T. Ulaby, and S. Moezzi

(E83-10020) ASSESSMENT OF RADAR RESOLUTION
REQUIREMENTS FOR SOIL MOISTURE ESTIMATION
FROM SIMULATED SATELLITE IMAGERY (Kansas
Univ. Center for Research, Inc.) 109 p
HC A06/MF A01
CSCL 08M G3/43

N83-12503

Unclas
00020

Remote Sensing Laboratory
University of Kansas Center for Research, Inc.
2291 Irving Hill Drive - West Campus
Lawrence, KS 66045

NAS 9-16419

Earth Resources Research Division
Lyndon B. Johnson Space Center
Houston, Texas 77058

1. Report No. SM-K2-04356	2. Government Accession No.	3. Recipient's Catalog No.

4. Title and Subtitle
ASSESSMENT OF RADAR RESOLUTION REQUIREMENTS FOR SOIL MOISTURE ESTIMATION FROM SIMULATED SATELLITE IMAGERY

5. Report Date
August 1982

6. Performing Organization Code

7. Author(s)
M.C. Dobson, F.T. Ulaby, and S. Moezzi

8. Performing Organization Report No.
RSL TR 551-2

9. Performing Organization Name and Address
Remote Sensing Laboratory
Univ. of Kansas Center for Research, Inc.
2291 Irving Hill Drive - West Campus
Lawrence, KS 66045

10. Work Unit No.

11. Contract or Grant No.
NAS 9-16419

12. Sponsoring Agency Name and Address
NATIONAL AERONAUTICS AND SPACE ADMINISTRATION
Jack Paris, Project Monitor
Johnson Space Center, Houston, TX 77058

13. Type of Report and Period Covered
Technical Report

14. Sponsoring Agency Code

15. Supplementary Notes

16. Abstract Simulation techniques were employed to generate orbital radar imagery of a 17.7-km by 19.3-km test site near Lawrence, Kansas. The simulations were produced for a radar operating at 4.75 GHz, with HH-polarization, and over an image swath defined by an angle of incidence between 7.5° and 9.3° from an orbital altitude of 600 km above mean sea level. Images were simulated for synthetic aperture radars (SARs) with resolutions of 20 m by 20 m, 93 m by 100 m, and 1 km by 1 km, and also for a real-aperture radar (RAR) with a resolution of 2.6 km by 3.1 km. For each simulation, the power received by the radar was determined with empirically derived formulae from a static terrain model and a dynamic meteorological and agricultural model that acted on each of the 20-m by 20-m pixel elements within the test site. The terrain model included surface elevation, land-cover category, and A-horizon soil texture. The dynamic model established daily distributions of surface-layer soil moisture from rain gauge and pan evaporation data using a water-budget approach dependent upon canopy cover, stage of crop development, soil type, and a Monte Carlo synthesis of between- and within-field variability. Radar simulations were performed at five-day intervals over a twenty-day period and used to estimate

17. Key Words (Selected by Author(s))
Radar, simulation, imagery, soil moisture, resolution, satellite, microwave, terrain

18. Distribution Statement

19. Security Classif. (of this report)	20. Security Classif. (of this page)	21. No. of Pages	22. Price*
Unclassified	Unclassified	96	

*For sale by the National Technical Information Service, Springfield, Virginia 22151.

soil moisture from a generalized algorithm requiring only received power and the mean elevation of the test site. The results demonstrate that the soil moisture of about 90 percent of the 20-m by 20-m pixel elements can be predicted with an accuracy of ±20 percent of field capacity within relatively flat agricultural portions of the test site. Radar resolutions of 93 m by 100 m with 23 looks or coarser gave the best results, largely because of the effects of signal fading. For the distributions of land-cover categories, soils, and elevation in the test site, very coarse radar resolutions of 1 km by 1 km and 2.6 km by 3.1 km gave the best results for wet moisture conditions while a finer resolution of 93 m by 100 m was found to yield superior results for dry to moist soil conditions.

RSL Remote Sensing Laboratory

The University of Kansas Center for Research, Inc.
2291 Irving Hill Drive-Campus West, Lawrence, Kansas 66045

Telephone: (913) 864- 4832

ASSESSMENT OF RADAR RESOLUTION REQUIREMENTS FOR SOIL MOISTURE ESTIMATION FROM SIMULATED SATELLITE IMAGERY

Remote Sensing Laboratory
RSL Technical Report 551-2

M. C. Dobson
F. T. Ulaby
S. Moezzi

Original photography may be purchased
from EROS Data Center
Sioux Falls, SD 57198

Fawwaz T. Ulaby, Principal Investigator

Supported by:
NATIONAL AERONAUTICS AND SPACE ADMINISTRATION
Johnson Space Center
Houston, Texas
Contract No. NAS 9-16419

TABLE OF CONTENTS

ACKNOWLEDGMENTS

This research was supported by the National Aeronautics and Space Administration, Johnson Space Center, Houston, Texas 77058.

LIST OF FIGURES

LIST OF TABLES

ABSTRACT

Simulation techniques were employed to generate orbital radar imagery of a 17.7-km by 19.3-km test site near Lawrence, Kansas. The simulations were produced for a radar operating at 4.75 GHz, with HH-polarization, and over an image swath defined by an angle of incidence between 7.5° and 9.3° from an orbital altitude of 600 km above mean sea level. Images were simulated for synthetic aperture radars (SARs) with resolutions of 20 m by 20 m, 93 m by 100 m, and 1 km by 1 km, and also for a real-aperture radar (RAR) with a resolution of 2.6 km by 3.1 km. For each simulation, the power received by the radar was determined with empirically derived formulae from a static terrain model and a dynamic meteorological and agricultural model that acted on each of the 20-m by 20-m pixel elements within the test site. The terrain model included surface elevation, land-cover category, and A-horizon soil texture. The dynamic model established daily distributions of surface-layer soil moisture from rain gauge and pan evaporation data using a water-budget approach dependent upon canopy cover, stage of crop development, soil type, and a Monte Carlo synthesis of between- and within-field variability. Radar simulations were performed at five-day intervals over a twenty-day period and used to estimate soil moisture from a generalized algorithm requiring only received power and the mean elevation of the test site. The results demonstrate that the soil moisture of about 90 percent of the 20-m by 20-m pixel elements can be predicted with an accuracy of ± 20 percent of field capacity within relatively flat agricultural portions of the test site. Radar resolutions of 93 m by 100 m witn 23 looks or coarser gave the best results, largely because of the effects of signal fading. For the distributions of land-cover categories, soils, and elevation in the test site, very coarse radar resolutions of 1 km by 1 km and 2.6 km by

3.1 km gave the best results for wet moisture conditions while a finer resolution of 93 m by 100 m was found to yield superior results for dry to moist soil conditions.

1.0 INTRODUCTION

Image simulation techniques offer an ideal mechanism by which to examine radar resolution requirements for characterization of area extensive terrain features. Radar images have been realistically simulated for the Seasat L-band radar and aircraft imaging radar systems when given appropriate terrain models and statistically accurate radar cross-sections for constituent scene elements [26,27].

The validity of the image simulation approach in defining optimal sensor resolution for a given application rests, in large part, upon the realism of the terrain model with respect to the application. Since our concern rests with an accurate assessment of near-surface soil moisture, special emphasis must be placed on incorporation of credible instantaneous soil moisture distributions at a scale less than or equal to that of the sensor resolution and the modeled moisture must be distributed over relatively large extents (if the entire radar image swath is to be simulated). This is certainly a non-trivial objective.

The well-documented variability of field measured soil properties [17,18,19,20], especially in the dynamic surface horizon, even within "homogeneous" test plots precludes the use of area-extensive point measurements of surface soil moisture as adequate inputs into a data base for radar image simulation. Thus, it seems reasonable to use a modeling approach to define the surface-layer soil moisture of a given terrain element as a function of time, with the model based upon the physical properties of that element.

This report will briefly review the results of earlier satellite radar simulation studies that attempted to define resolution requirements in soil moisture estimation and will interpret these findings with respect to the procedure used to model soil moisture. Section 2 will develop a more detailed and realistic soil-water model which will feed a series of satellite radar simulations presented and analyzed in Section 3. These simulations will include three synthetic aperture radars (SAR) with nominal resolutions of 20 m, 100 m, and 1 km and also a real-aperture radar (RAR) with a nominal resolution of about 3 km.

1.1 Prior Radar Simulation Results for Assessment of Soil Moisture

An earlier examination of resolution requirements of an orbital SAR used for estimating surface soil moisture by image simulation techniques [1,2] made use of the radar configurations shown in Table 1.1. The satellite, operating at a frequency of 4.75 GHz with HH polarization, is given an orbital altitude of 600 km above mean sea level and an antenna pointing angle range from 6.4 degrees to 20.0 degrees which results in a nominal angle-of-incidence range of 7 degrees to 22 degrees, assuming a curved-earth surface as shown in Figure 1.1. Of the fourteen system design options presented in Table 1.2, three synthetic-aperture radars were chosen for simulation - Cases 2, 4, and 8 - which yielded approximate resolutions of 20 m with 12 looks. 100 m with 23 looks, and 1 km with 1,000 looks respectively.

The radar simulations operated on a data base constructed at a 20-m x 20-m grid cell resolution for a predominantly agricultural region (17.7 km x 19.3 km) located just southeast of Lawrence, Kansas [1,2]. The net percent area occupied by each target class is shown in Table 1.3. In addition to target class as interpreted from U-2 color IR photography, each of the 800,000 grid cells in the data base was

TABLE 1.1

Spacecraft Radar Configuration

Spacecraft Height	h	600 km
Radar Frequency	f	4.75 GHz
Angle of Incidence Range	θ	7° - 22°
Antenna Pointing Angle Range	δ	6.39° - 20.02° (curved earth)
Receiver Noise Figure	F	4 (6 dB)
Minimum Signal-to-Noise Ratio	S_n	4 (6 dB)
System Loss Allowance		2 (3 dB)
Minimum Scattering Coefficient	σ^o_{min}	- 21 dB
Antenna Length	D	8.7 m (8.7 m and 15 m for RAR and 5 m for RADISAR)
Antenna Radiation Efficiency	η	0.75
Ground Swath-Width	S_g	143 km
Slant Swath-Width	R_a	38.5 km

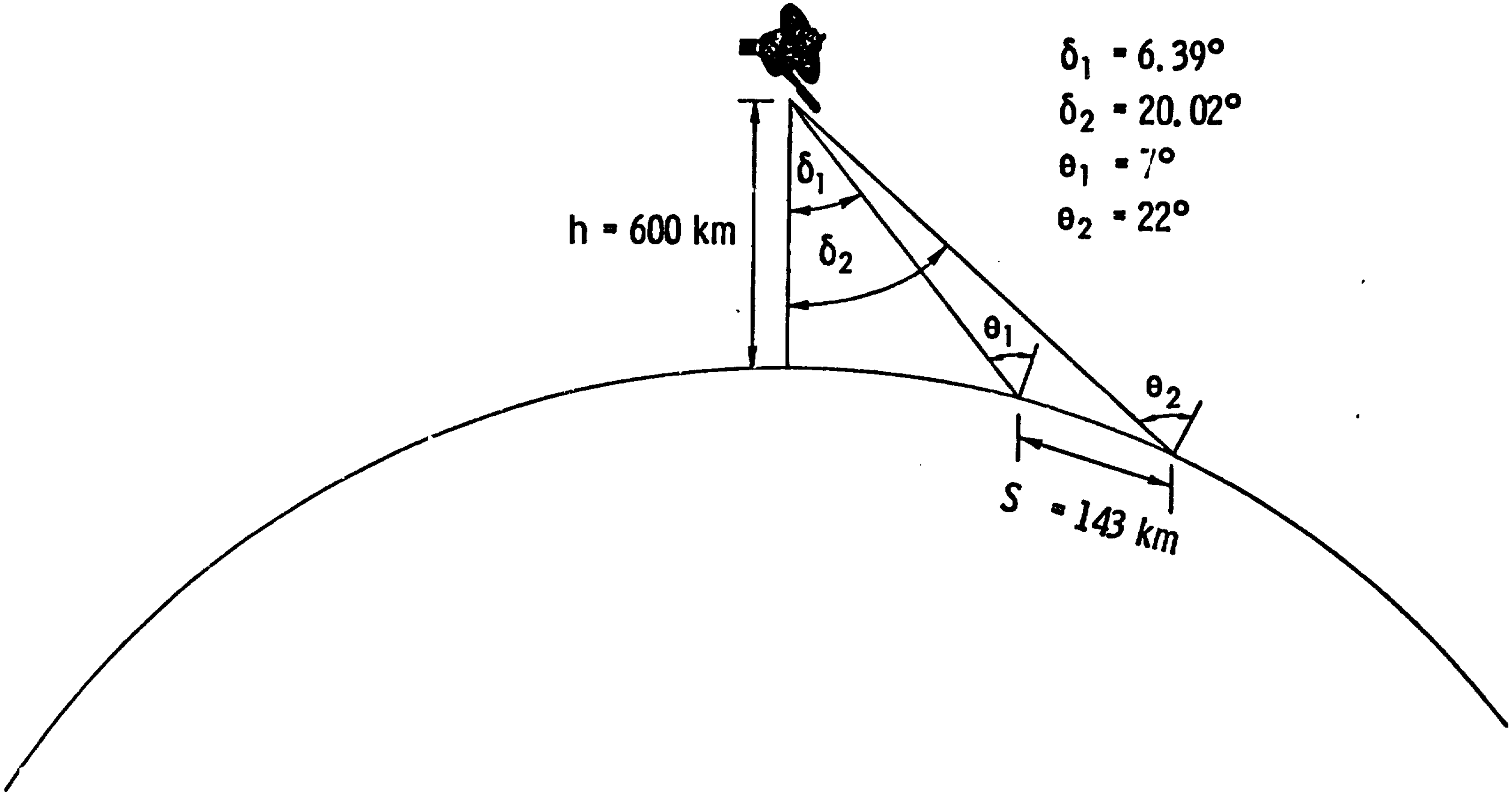

Figure 1.1. Side-looking SAR observing a curved earth from an altitude of 600 km.

TABLE 1.2

Potential System Design Options

Case #	Type	Slant Range Resolution r_R(m)	Number of Looks Available in Azimuth	Number of Looks Used N	7° $r_a \times r_y$ (m x m)	7° Equiv. Square Photo Pixel (m x m)	22° $r_a \times r_y$ (m x m)	22° Equiv. Square Photo Pixel (m x m)	Average Power (W)
1	Fully-focused SAR	0.52	1	1	4.1x4.3	19.6x19.6	4.4x1.4	11.6x11.6	9850
2	Partially-focused SAR	3.75	2.3	12	9.3x31	25x25	10x10	14.7x14.7	7198
3	Partially-focused SAR	11.2	6.9	12	28x92	75x75	30x30	44x44	800
4	Partially-focused SAR	11.2	23	23	93x92	122x122	100x30	72x72	460
5	Partially-focused SAR	37.5	23	23	93x307	223x223	100x100	132x132	138
6	Unfocused SAR	37.5	69	69	280x307	343x343	300x100	202x202	138
7	Unfocused SAR	112	69	69	280x922	594x594	300x300	351x351	46
8	Unfocused SAR	112	230	230	934x922	1010x1010	1000x300	596x596	46
8a	Unfocused SAR	375	69	69	280x3074	1084x1084	300x1000	640x640	13.8
9	RAR (D = 8.7 m)	26.6	1049	1049	4264x218	1004x1004	4564x71	592x592	194
10	RAR (D = 15 m)	45.0	363	363	2545x369	1036x1036	2724x120	616x616	38.6
11	Unfocused SAR	375	230	230	934x3074	1844x1844	1000x1000	1088x1088	13.8
12	RAR (D = 15 m)	375	363	363	2545x3074	2992x2992	2724x1000	1765x1765	4.6
13	RAR (D = 8.7 m)	562	1049	1049	4263x4611	4613x4613	4564x1500	2722x2722	9.2
14	RADISAR (5 m x 5 m antenna 19 scan positions)	213	12	12	532x532	785x785	570x173	463x463	0.66

TABLE 1.3

Area Percent of Total Data Base Assigned to Each Target Class

Target Class	Percent of Total Area	
Roads	3.76	
Railroads	0.12	
River Bridges	0.01	
City Structures	0.85	
Rivers	2.19	2.67
Lakes, Ponds, Impondments	0.48	
Smooth Bare Soil (RMS height < 2 cm)	6.63	
Medium Rough Bare Soil (2 cm < RMS height ≤ 4 cm)	4.92	
Rough Bare Soil (RMS height > 4 cm)	2.75	
Mown Pasture	7.06	
Pasture	15.93	
Alfalfa	4.15	
Wheat	6.65	
Sandbars	0.35	
Deciduous Trees	13.03	
Soybeans N/S Rows	5.46	11.08
Soybeans E/W Rows	5.62	
Milo N/S Rows	2.76	5.03
Milo E/W Rows	2.27	
Corn N/S Rows	8.32	14.93
Corn E/W Rows	6.61	

* N/S refers to crops planted with rows running north to south.
* E/W refers to crops planted with rows running east to west.

assigned an elevation from USGS 7.5-minute-series topographic maps and a surface soil texture from USDA/SCS county soil surveys.

A set of four general soil moisture conditions was computed for this data base for subsequent integration into the target-sensor interaction submodel of the radar simulation program. Surface soil moisture was calculated by a highly simplistic daily accounting of incident rainfall and evaporative losses with some limiting assumptions so that soil moisture could not exceed saturation or be less than the hygroscopic coefficient. A storm submodel generated precipitation with a very broad Gaussian distribution of intensity across a linear storm track. The water budget model did not account for the following:

- surface slope
- effects of soil type on soil bulk density or hydraulic conductivity
- transpiration by a vegetation canopy
- soil profile effects
- dependence of hydraulic conductivity on soil moisture
- presence of standing water on surface.

A summary of the postulated soil moisture conditions is presented in Table 1.4. The soil water-budget model produced 0-5-cm soil moisture values as volumetric moisture (g/cm^3) which were subsequently converted to a percent of field capacity (M_{FC}) basis by an empirical expression dependent upon soil textural components.

Elevation information was used to calculate the local angle of incidence θ_ℓ from range and slope information for each pixel. The mean backscattering coefficient $\bar{\sigma}^0$ for a cell was computed from a series of empirical relationships found to be statistically valid for each

TABLE 1.4

Values of Rainfall and Evaporation Used to Derive the Hypothetical Soil Moisture Conditions

Simulation Number, N	Day Number	Rainfall, cm	M_{rain} g/cm^3	Mean Evaporative Rate, cm/day	Number of Elapsed Days	M_{evap}, g/cm^3	M_{FC_N}, % of 1/3-bar water content	Estimate M_{FC_N}	
								Max.	Min.
1	4	not determined	>>FC	not determined	3	-	$M_{FC_1} = 100.0$	100.0	100.0
2	5	≤ 2.5	≤ 0.25	not determined	0	0.0	$M_{FC_2} = M_{FC_1} + 100(M_{rain}/FC)$ and $M_{FC_2} \leq 150.0$	150.0	100.0
3	15	0	0	0.1	10	0.2	$M_{FC_3} = M_{FC2} - 20/FC$ and $M_{FC_3} \geq 25.0$	90.7	25.0
4	35	0	0	0.005	20	0.2	$M_{FC_4} = M_{FC_3} - 20/FC$ and $M_{FC_4} \geq 10.0$	31.5	10.0

combination of θ_ℓ, M_{FC}, and target category [1]. For a given sensor configuration and terrain element area, $\bar{\sigma}^o$ of a pixel was converted into an averaged received power $\bar{\bar{P}}_r$ by the radar equation. Since, for the three resolutions simulated, the number of looks N was always less than infinity, $\bar{P}_r$ was randomized for Rayleigh fading with the appropriate number of looks to a received power P_r at the antenna.

The resultant images of P_r were then machine processed into soil moisture estimate maps using only cell position and mean elevation of the whole 17.7-km x 19.3-km data base (from which an estimate of θ_ℓ and area could be deduced for each pixel assuming a spherical earth). The moisture content of each cell was then estimated from

$$\hat{M}_{FC} = [\sigma^o - f(\theta)]/g(\theta) \qquad (1.1)$$

where

$\hat{M}_{FC}$ = estimated percent of field capacity of the 0-5-cm layer,

σ^o = scattering coefficient (in dB) as estimated from P_r and range (assuming spherical earth),

θ = angle of incidence estimated from range to target, and

$f(\theta)$ and $g(\theta)$ = empirically determined polynomial expressions [1].

Finally, the radar soil moisture estimate accuracy of a given simulation was deduced by comparing the map of $\hat{M}_{FC}$ to the spatial distribution of M_{FC} defined by the soil water-budget model. This process yielded an imperfect comparison since the radar imaging process significantly distorted the geometry, and positioning errors for even small hills in the data base often lead to offsets of 100 m between $M_{FC_{i,j}}$ and $\hat{M}_{FC_{i,j}}$ where i and j are relative positioning coordinates. This entire process and the data and assumptions on which it is based are treated in a more comprehensive fashion by Ulaby, et al. [1 and 2].

Results of the above comparison procedure for each of the 20-m x 20-m grid cells in the actual moisture distribution generated by the water-budget model are shown in Figures 1.2 and 1.3 for the whole 800,000-cell data base and the 183,000-cell river floodplain region respectively, for moderately dry to moist soil conditions. Results such as these, between angles of 7 degrees and 20 degrees, showed that estimates of soil moisture from the 100-m and 1-km resolution radar systems yielded significantly less estimate error than that afforded by the 20-m resolution radar. Furthermore, if nonagricultural categories such as buildings, roads, bridges, and water (where soil moisture is undefined on the M_{FC} map) are excluded from the comparison, and the comparison is also limited to the relatively flat floodplain of the river (where positioning errors are minimized), between 81% and 90% of the 20-m x 20-m grid cells are found to have less than 20% absolute error in the estimate in Figure 1.3. It should be noted here that these comparisons are performed on a 20-m x 20-m basis, hence all sensor resolutions are being evaluated as though they are predicting moisture at a 20-m scale.

The effect of averaging the input moisture distribution M_{FC} to a 1-km x 1-km scale is shown in Figure 1.4. Also shown are the distributions of predicted moisture $\hat{M}_{FC}$ resulting from interpretation

ORIGINAL PAGE IS
OF POOR QUALITY

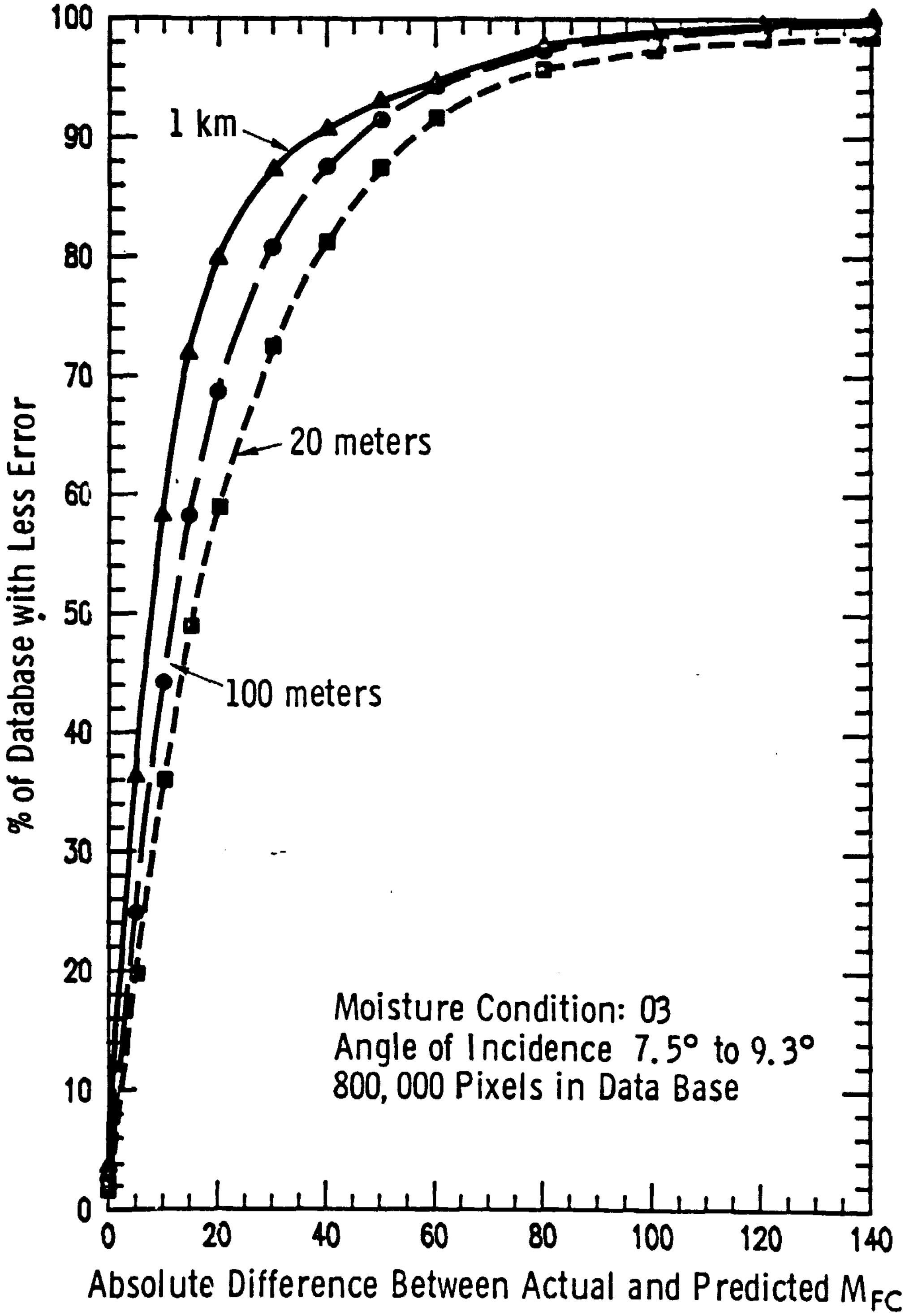

Figure 1.2. Soil moisture estimate accuracy for the entire simulation data base with moisture condition 3, ten days after thunderstorm, and at angles of incidence between 7.5° and 9.3°. Absolute difference is computed at a 20 meter resolution from [2].

ORIGINAL PAGE IS
OF POOR QUALITY

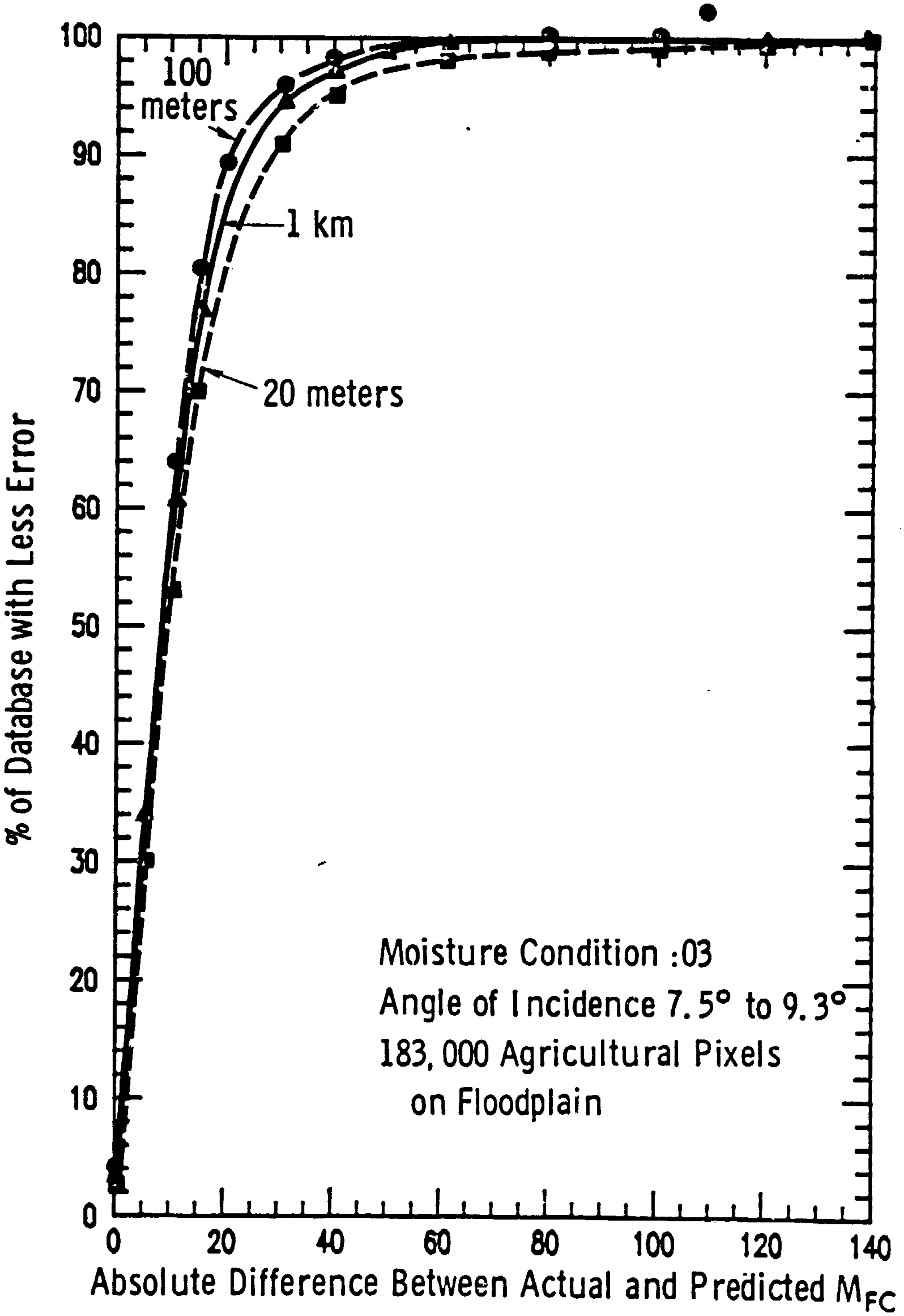

Figure 1.3. Soil moisture estimate accuracy for agricultural categories on the floodplain with moisture condition 3, ten days after thunderstorm, and at angles of incidence between 7.5° and 9.3°. Absolute difference is computed at a 20 meter resolution from [2].

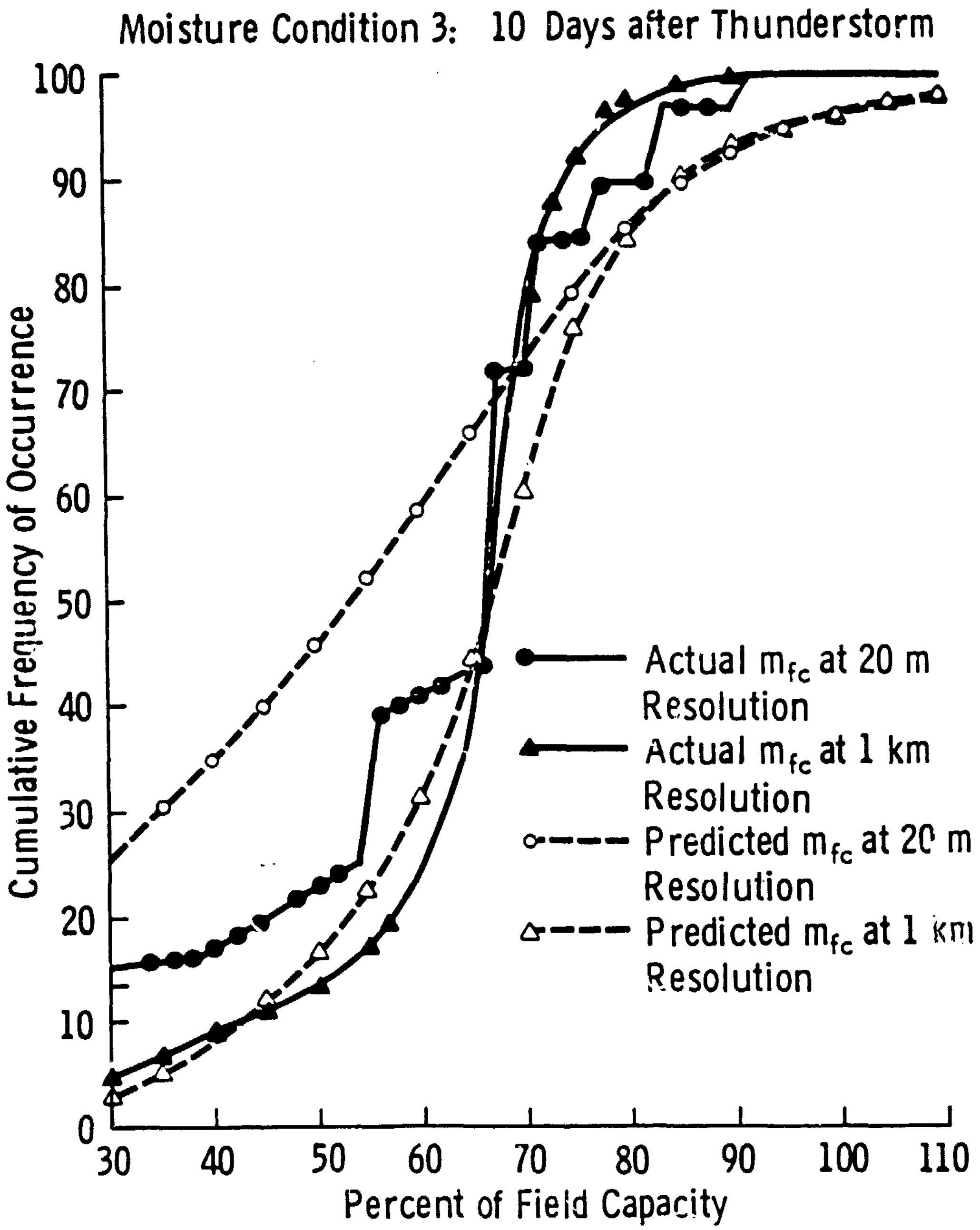

Figure 1.4. Comparison of actual soil moisture distribution (as 20 m x 20 m and 1 km x 1 km averages) with the distributions predicted from simulated radar imagery at 20 m and 1 km sensor resolutions.

of the 20-m resolution SAR and the 1-km resolution SAR. Obviously, the $\hat{M}_{FC}$ from the 1-km SAR more closely tracks the actual distributions of M_{FC} over most of the range. The combined effect of varying both radar resolution and the scale of comparison (or resolution of the moisture estimate) is demonstrated by Figure 1.5. This figure rescales the results plotted on Figure 1.2 for SAR resolutions of 20 m and 1 km (as used to estimate soil moisture at a 20-m resolution) and shows that an additional "improvement" in accuracy is achieved when the 1 km SAR is used to estimate moisture at a 1-km x 1-km scale. This apparent improvement is not unexpected and is merely a consequence of the reduction of local variance in average M_{FC}.

A summary of results for all four moisture conditions generated from the water-budget model is shown in Figure 1.6. Here the percent of 20-m x 20-m grid cells with an absolute moisture estimate error of less than 30% of field capacity is plotted as a function of resolution. The trend toward increasing estimate accuracy by using coarser resolution sensors is apparent for all moisture conditions although this trend seems to break down for extremely dry soil moisture conditions.

These findings have been attributed to several considerations [2],

1) M_{FC} as generated by the water-budget model varies dramatically only between adjacent soil types (typically a soil type is on the order of 100 m to 1 km wide);

2) the coarser resolutions act as low-pass spatial filters and average the local "noise" effects of slope, canopy cover type, row direction, and surface roughness, and

3) the effects of water bodies, cultural targets, and forested

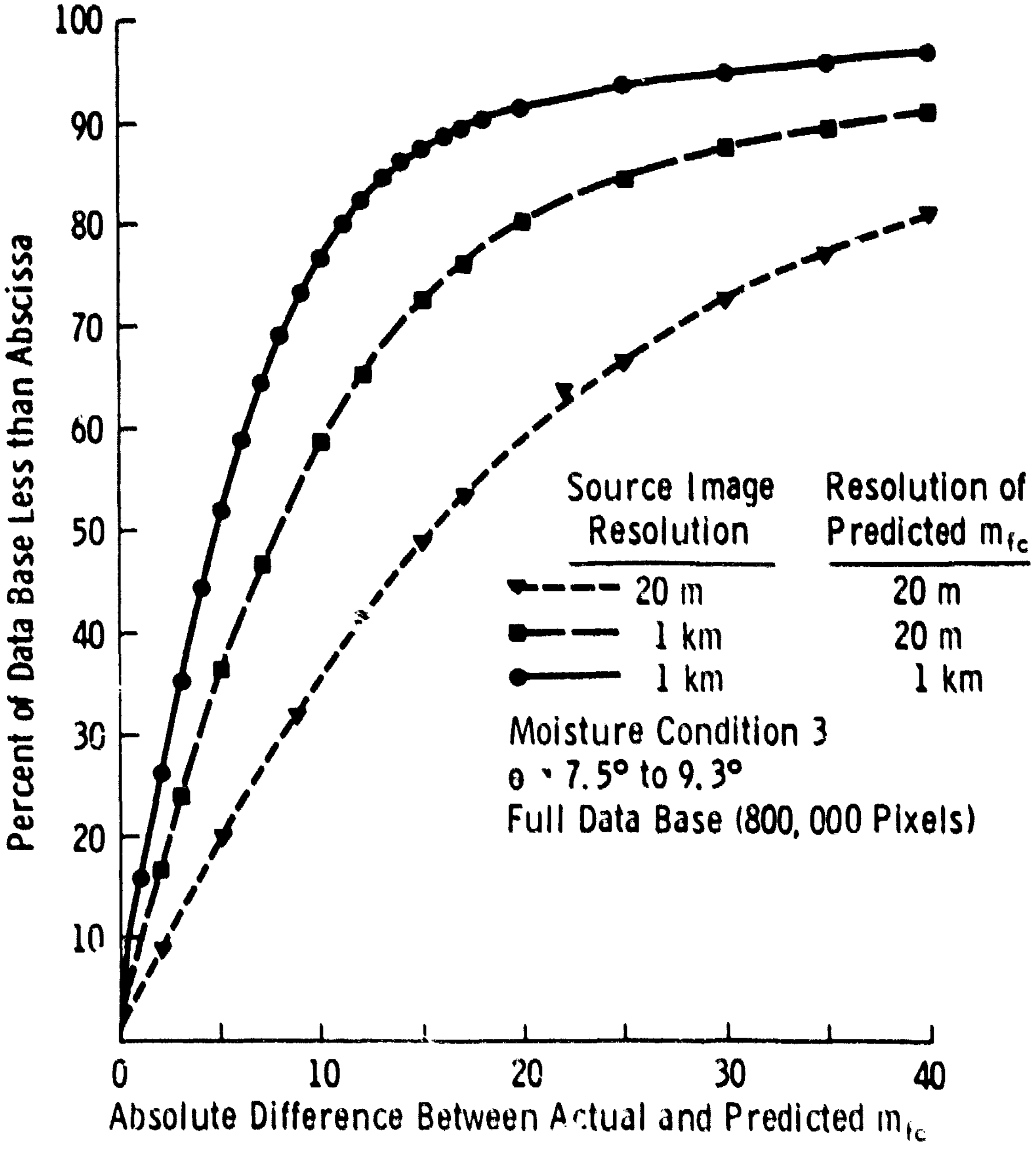

Figure 1.5. The effect on absolute soil moisture estimate accuracy of varying comparison scale from 20 m cells to 1 km cells.

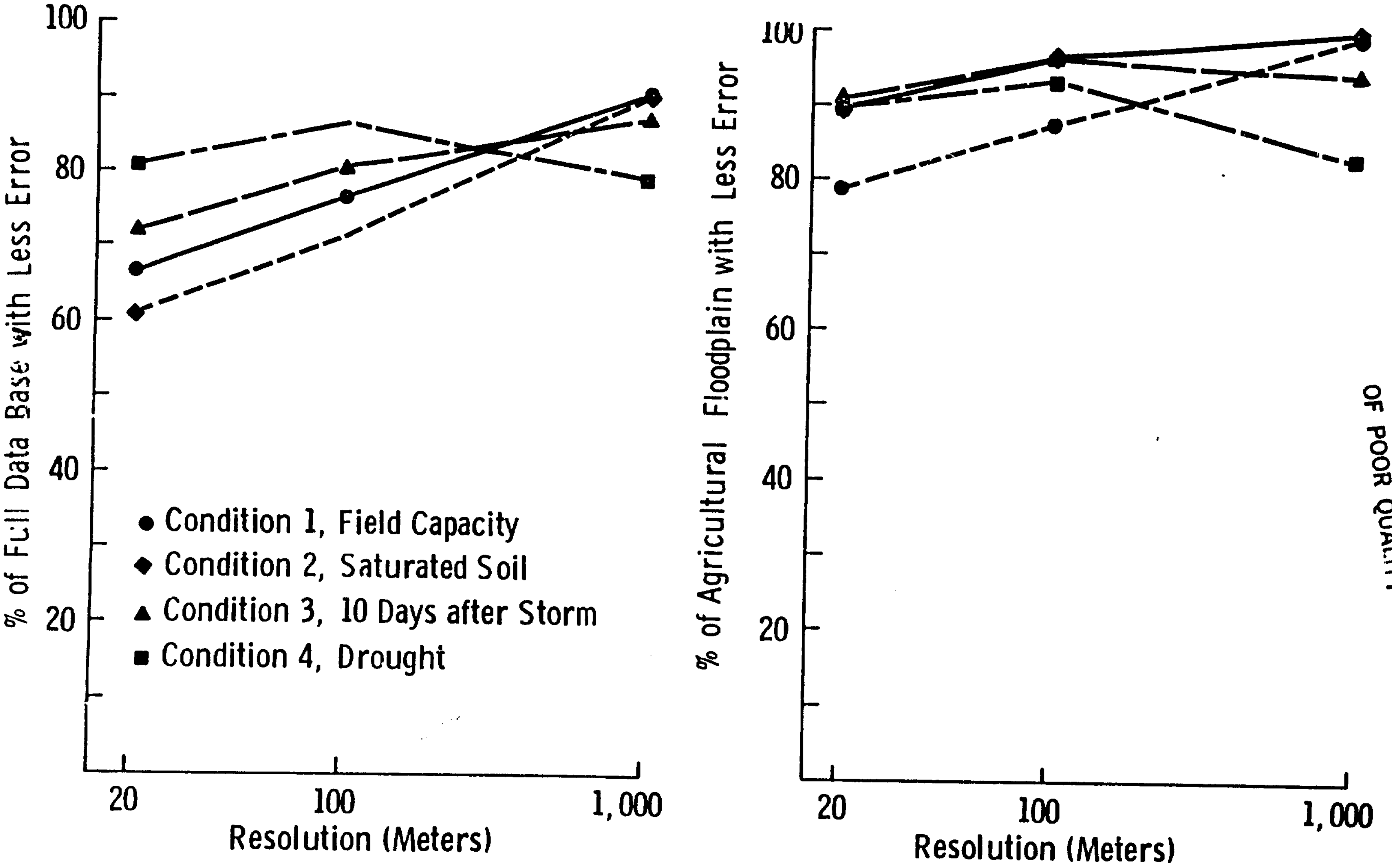

Figure 1.6. Percent of data base where estimated moisture M_{FC} is within ±30% of actual moisture M_{FC}. Angle of incidence θ is 7.5° to 9.3° relative to nadir. Accuracy level 3 is approximately ±30% of field capacity.

areas are averaged over much larger regions by a coarse resolution sensor.

Implicit in these conclusions is that the most appropriate (accurate) sensor resolution for moisture mapping is inextricably linked to the scale of variance in the target parameter of interest: soil moisture. This is further complicated by the density of the distributions of observable "noise" parameters such as cultural targets, water bodies, hills, and within-field surface roughness effects. Hence, it is possible that a different set of assumptions regarding the nature of actual moisture distribution may lead to very different conclusions.

Figure 1.7 shows the cumulative distributions of soil moisture M_{FC} produced by the simple water-budget approach described above. While the net moisture conditions are very different, ranging from saturated soil conditions on Day 5 to near the hygroscopic coefficient or Day 35, only Day 15 (Moisture Condition 3) encompasses a wide range of instantaneous soil moisture conditions. For Day 15, the discontinuities present on the cumulative graph demonstrate that variance in moisture is primarily controlled by soil type and only weakly by the minor variance in rainfall from the storm submodel.

1.2 Modifications of the Simulation Data Base

As a consequence of the simplicity of moisture distributions produced by the above water-budget model, the conclusions reached [1,2] are reevaluated using a more complicated and realistic accounting procedure as well as introducing sources of between- and within-field variance other than cover category (Table 1.3) and soil type,

ORIGINAL PAGE IS
OF POOR QUALITY

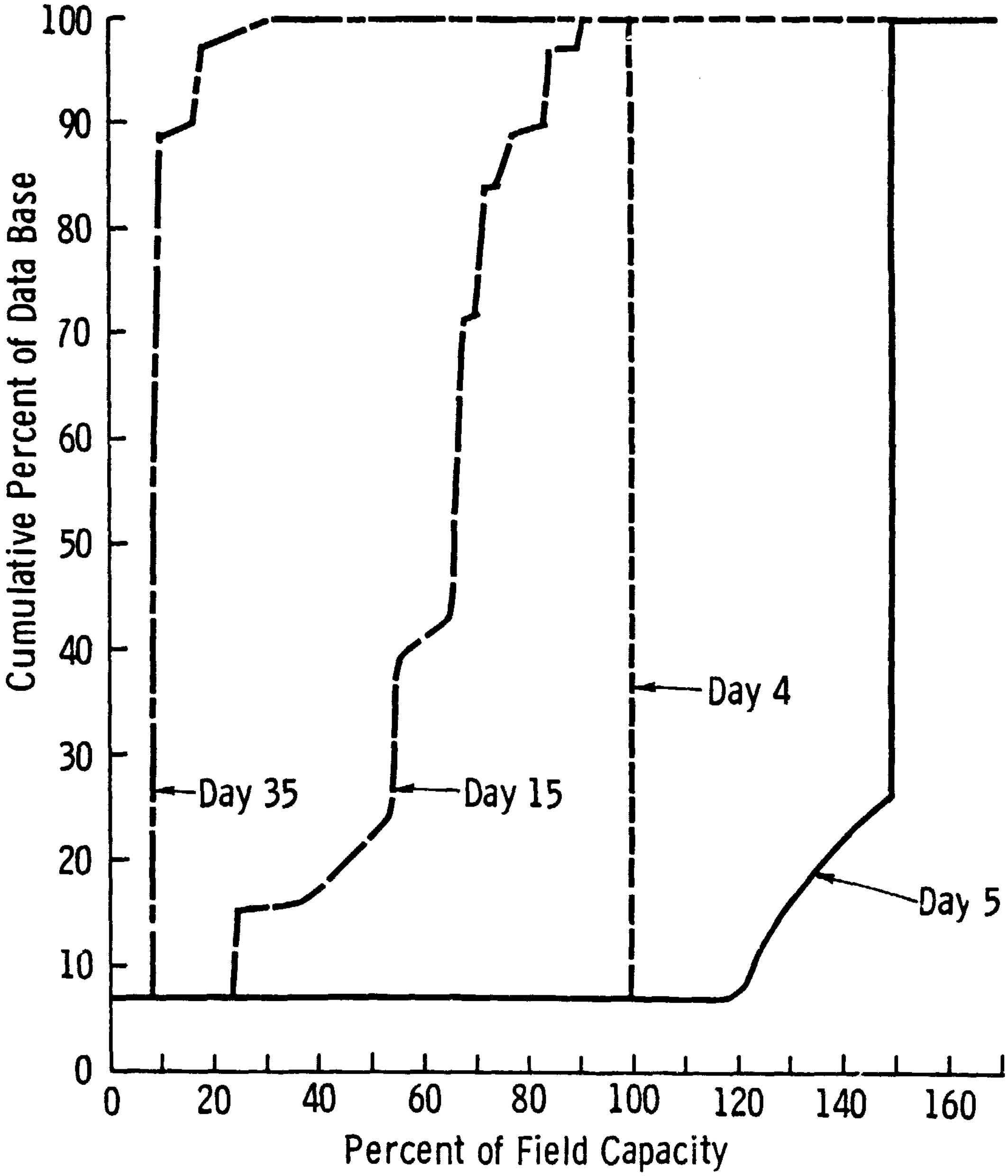

Figure 1.7. Cumulative frequency distributions of "actual" soil moisture for the four simulated conditions generated from the simplified environmental model given in Table 1.3.

respectively. Figure 1.8 presents a diagram of the simulation process modified by Section 2 and used to generate the images analyzed in Section 3.

Significant improvements in the data base as a dynamic model for radar simulation studies of agricultural terrain include:

- incorporation of cropping calendars to allow for additional between-field but within-crop variability;
- addition of within-field variability in moisture by a Monte Carlo approach;
- a more comprehensive soil water accounting model (SWAM).

A diagram of surface conditions relevant to SWAM is shown in Figure 1.9. The model basically consists of three potential layers: standing water, the upper 5 cm of the soil, and a crop root zone (nominally extending to a 1-meter depth). The water table is always treated as being well below 1 meter. The model, while still simplistic, treats both infiltration and evapotranspiration as dependent on dynamic soil and crop canopy conditions. In addition, a more robust storm model leads to a greater variability in incident rainfall, which is subsequently allowed to run off or to infiltrate depending upon the intensity of the rain, antecedent soil moisture, and local surface slope.

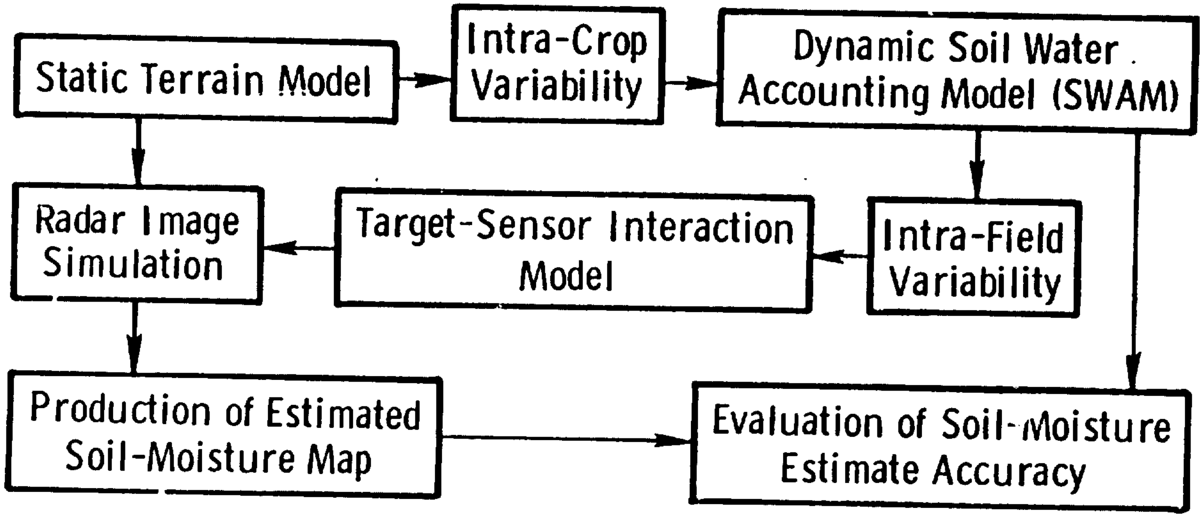

Figure 1.8. Flow chart of general simulation model.

ORIGINAL PAGE IS
OF POOR QUALITY

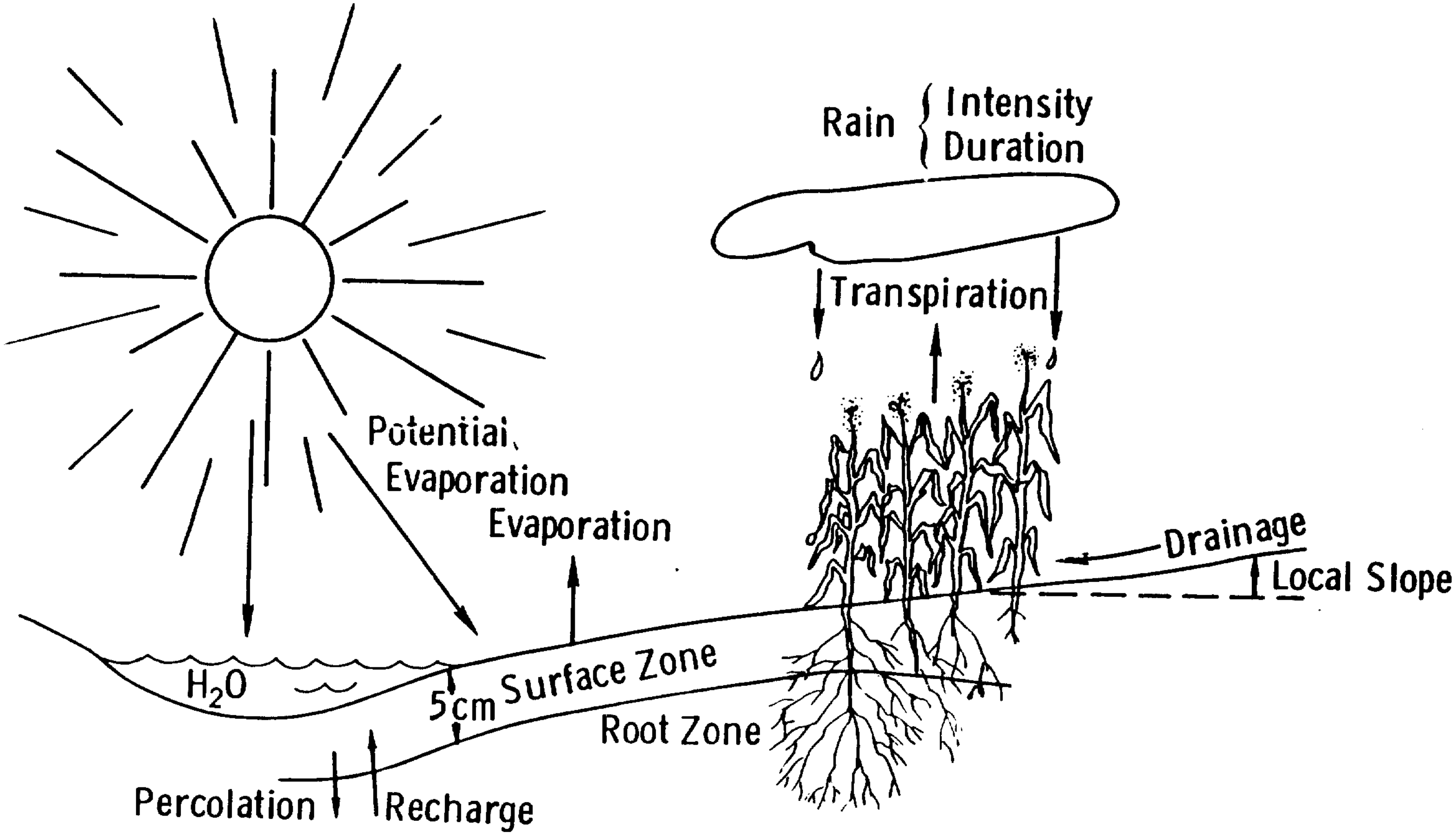

Figure 1.9. Local environmental conditions pertinent to the soil water accounting model.

2.0 DYNAMIC SOIL WATER ACCOUNTING MODEL (SWAM) AND VARIANCE IN SOIL MOISTURE

The purpose of a soil water-budget model within the context of realistic radar image simulation is to generate a distribution of near-surface (0-5 cm) soil moisture conditions at the spatial scale of the static terrain data base (20 m x 20 m) which responds to both static conditions (soil type, cover type, and surface slope) and dynamic conditions (crop stage, rain, and potential evaporation) on a time scale relevant to both the dynamics of the process and the orbital mechanics of an imaging satellite (daily basis). While many excellent water-budget models are available for various applications in agronomy and hydrology [3 to 7], no single model meets all the above criteria. Indeed, most such models require more detailed information on soil profile characteristics and weather conditions than is readily available for the simulation area and are designed to operate at a level much less than field size over time increments significantly less than one day, or conversely, they are most appropriately applied to very coarse integration times on the order of weeks for a simple set of input parameters and at a macroscopic level much larger than field size.

Because of the large size of the data base (approximately 800,000 grid cells) it is necessary to tailor a model that emphasizes the surface horizon, requires a minimum of information as to soil profile and detailed local weather conditions, and yet is still sensitive to daily variation in soil moisture. A schematic of the final process model is shown in Figure 2.1; it consists largely of the following components:

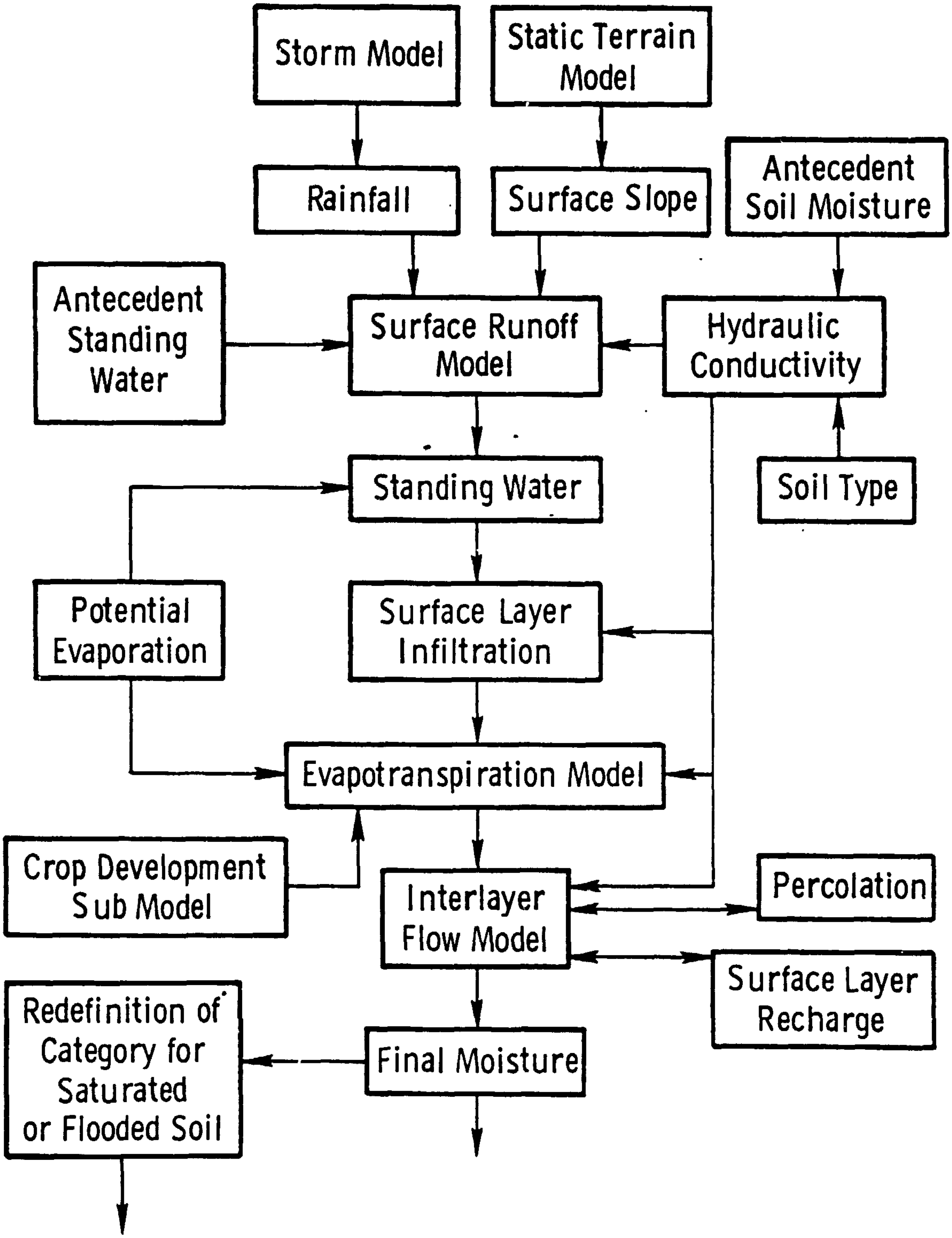

Figure 2.1. Dynamic Soil Water Accounting Model (SWAM).

- storm model,
- surface runoff model,
- crop development submodel,
- evapotranspiration model, and
- an interlayer redistribution model.

When given dynamic inputs of crop type, crop stage of development, rainfall, and potential evaporation, the model acts upon the static terrain model to yield daily projections of 0-5-cm soil moisture for each grid cell. It also governs the redefinition of canopy cover categories based on crop-calendar changes or local flooding conditions, and these categories are then used as input to the radar image simulation program's target-sensor interaction model.

2.1 Storm Model

The storm model used in SWAM combines a rain intensity distribution function determined by storm type with rain-gauge data and a Monte Carlo appraoch to storm-track positioning. For computational ease, the simplifying assumptions are made that all storm cells proceed along an east-west axis across the data-base matrix and do not begin or terminate (temporally) within the data base.

Daily rainfall in cm as recorded at Clinton Reservoir, Kansas in 1978 is shown in Figure 2.2 for a 220-day period as extracted from NOAA monthly summaries of local climatological data. For each rainfall event, the duration of the rainfall was also recorded and average rainfall intensity was computed from

ORIGINAL PAGE IS
OF POOR QUALITY

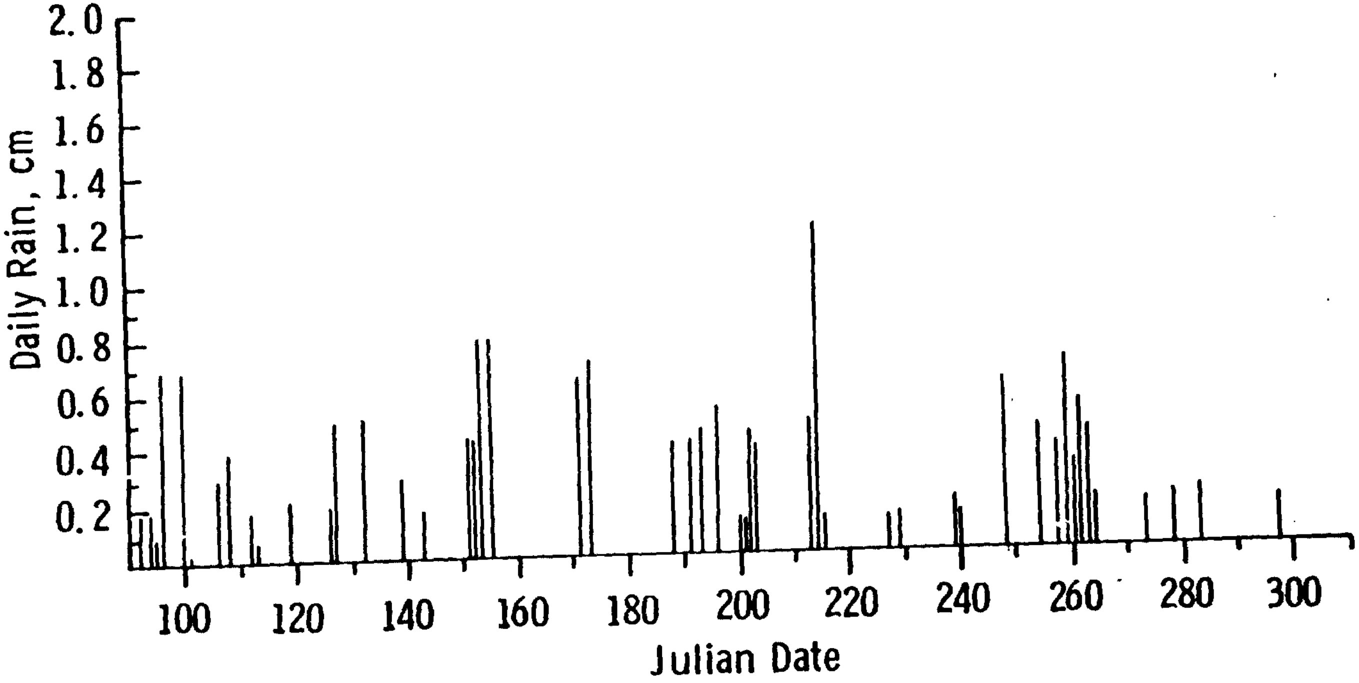

Figure 2.2 Daily precipitation recorded at Clinton Reservoir, Kansas during 1978.

$$I_g = R_g/t \tag{2.1}$$

where

I_g = rainfall intensity at the gauge, cm/hr

R = net daily rainfall, cm

t = storm duration, hours.

Each storm was also classified as a local convective event, as part of a large frontal event, or as intermediate. This three-scale storm classification serves as the basis for rain intensity functions that are based, in turn, upon results which indicate that intensity decays exponentially from the peak intensity to some minimum value at the perimeter of the rain-producing storm cell [9-12]. The function takes the form:

$$I(D) = I_{max} * [A_T + B_T * \exp(C_T * Y)]/D \tag{2.2}$$

where I_{max} = intensity at the storm center,

A,B,C = are fitted values for each storm type T (based on [10,11],

Y = the lateral radius of the storm cell, and

D = distance between I and I_{max}, km.

The range of fitted values from convective to frontal-type storms are:

10.8 to 45.7 for A,

163.5 to 90.8 for B, and

-0.20 to -0.09 for C.

Since the center of the storm cell is not known relative to the measured gauge data, it is synthesized by an equi-probability random-number generator. Intensity along the center of the storm trajectory is then computed by inverting Eq. 2.2 to the form

$$I_{max} = I_g * D/[A_T + B_T * \exp(C_T * Y)], \qquad (2.3)$$

where D = random distance between the storm track and the rain gauge.

A second randomization is then used to position the storm track with respect to the 800,000 grid cells in the data base. As a result, it is possible for specific storm events measured on the gauge data to completely miss the simulation area; however, the application of appropriate limits to the random-number generators makes this a rare occurrence.

Thus, given the maximum rainfall intensity, the trajectory of the storm cell, the storm type, and the extent of the storm, the rainfall intensity of any grid cell can be calculated from Eq. (2.2). For the 20-day portion of the rain gauge data after Julian day 153, the intensity of all storm events is plotted as a function of north-to-south distance within the simulation data base in Figure 2.3. A distance of zero designates the northern edge of the data base. Three rain events occur within this period in June, during which the simulated radar overpasses occur on a five-day revisit period. Two of the storms are local convective showers, both having measured rainfall of 0.8 cm over one-hour durations. The randomization of storm-track location separates the two events in space and gives the one on Julian day 156 a slightly higher maximum intensity. The rainfall on Julian

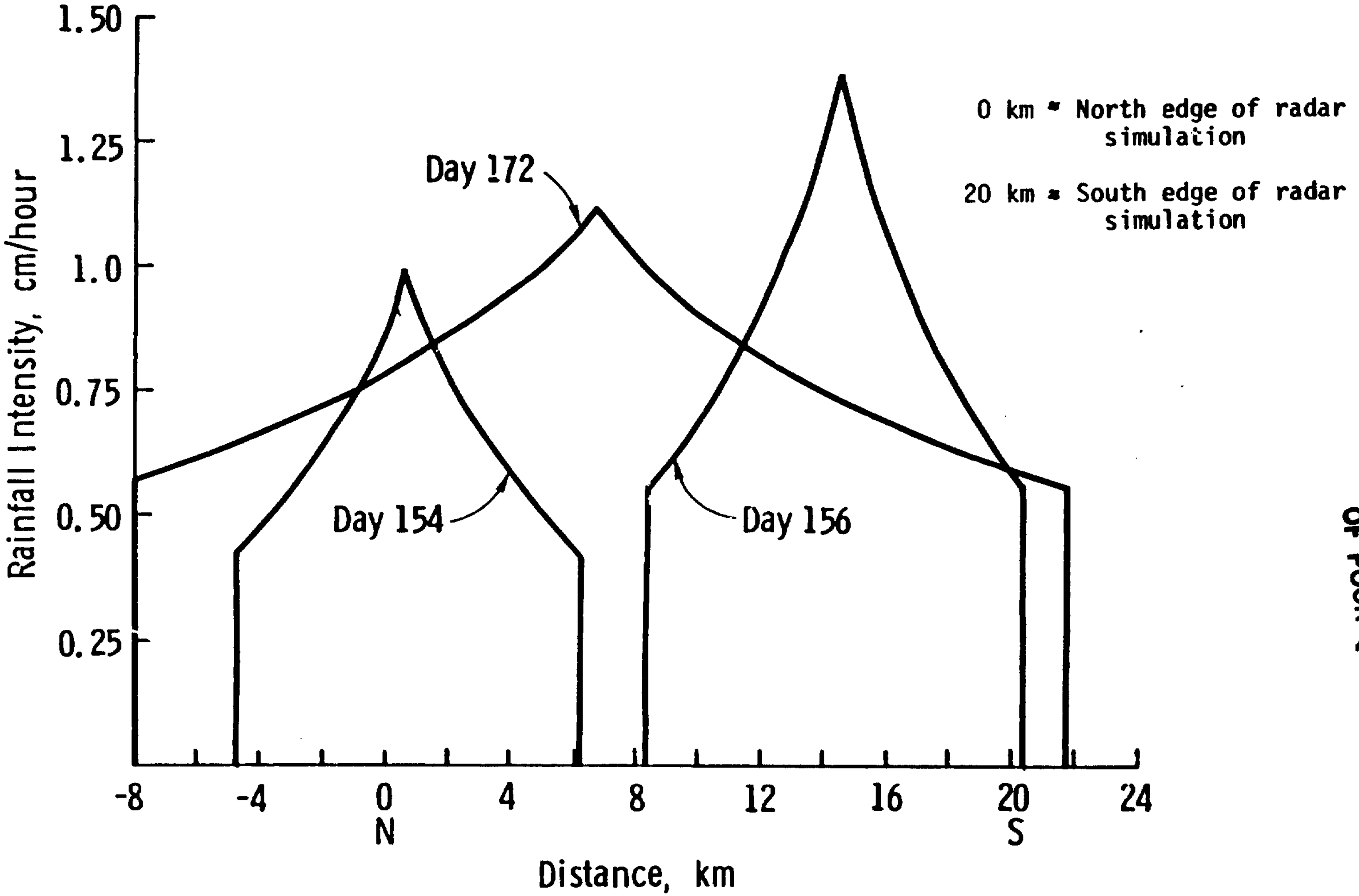

Figure 2.3. Rain intensity over the simulation area as modeled from rain-gauge data during the 20-day period covered by the radar simulations.

day 172 is much more extensive and has a duration of eight hours. The net daily rainfall as distributed by these three events over and around the simulation area is shown in Figure 2.4. The maximum incident rainfall over the 20-day period is seen to be approximately 9 cm, which is reasonable for the simulation region in mid-June.

2.2 Surface Runoff Model

The surface runoff model considers only the net effect of local surface slope and does not explicitly account for water retention and impoundment by soil surface roughness, tillage practices, and the presence of terraces. The water available for drainage as lateral surface flow is equal to the sum of standing water remaining from the previous daily accounting period plus the incident rainfall in excess of that which can infiltrate the surface layer of the soil during the rainfall event. The infiltration rate is linked to the antecedent moisture of the surface layer. Thus the potential drainage D_p becomes:

$$D_p = SW + t*(I - K) \qquad (2.4)$$

where

SW = standing water

t = duration of rain event

I = intensity of rainfall

K = hydraulic conductivity of the surface layer.

The actual drainage D_A is computed from D_p and local surface slope by:

ORIGINAL PAGE IS
OF POOR QUALITY

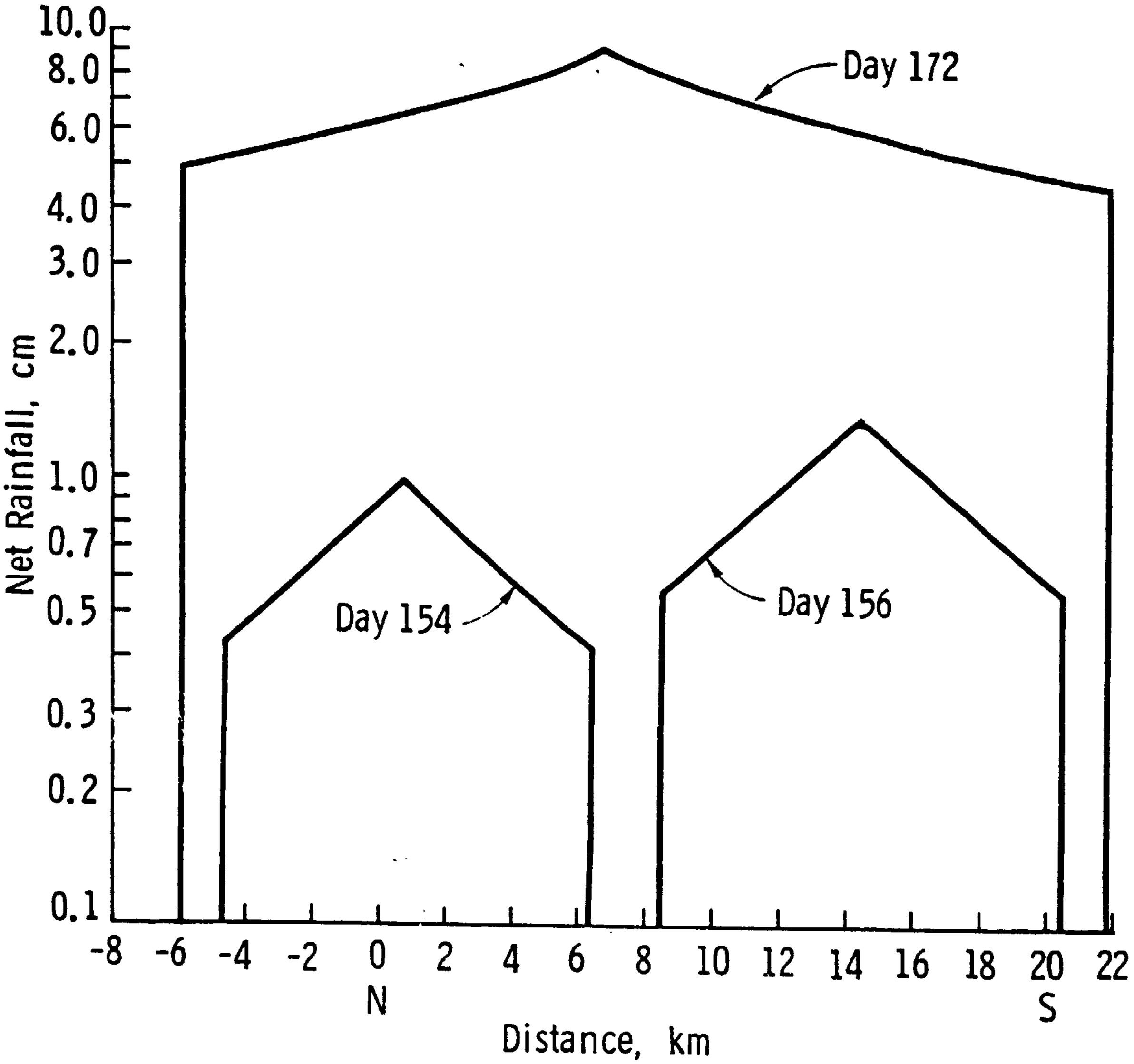

Figure 2.4. Net daily rainfall over the simulated area during the 20 day period covered by the radar simulations.

$$D_A = D_p * (1.0 - 0.8^{\alpha}) \tag{2.5}$$

where α = the slope angle of the surface from horizontal in degrees.

The term $1.0 - 0.8^{\alpha}$ is defined as the drainage coefficient and is plotted versus surface slope (in percent) in Figure 2.5. While most of the slopes in the data base are less than 6 percent for agricultural fields, local slope can exceed 15 percent for some of the hills adjacent to the Kansas River floodplain.

2.3 Evapotranspiration Model

Evapotranspiration is calculated differently for cropped and bare soil surfaces. For bare soil surfaces the actual evaporation is depleted solely from the soil surface layer, while for vegetated surfaces a static root distribution model removes 20 percent of the actual evapotranspiration from the 0-5-cm layer and removes the remaining 80 percent of actual evapotranspiration from the "root zone." For simplicity, the "root zone" is assumed to be one meter in depth and is treated as a constant with time and for all crops.

For bare soil, actual evaporation, AE, is computed from potential evaporation, PE, as limited by antecedent soil moisture in the surface layer and soil hydraulic properties. Accounting is performed on a daily basis using the daily pan evaporation recorded at Clinton Reservoir, Kansas and is shown in Figure 2.6 for 1978.

An experimental model is used to calculate actual evaporation from potential evaporation PE [13]:

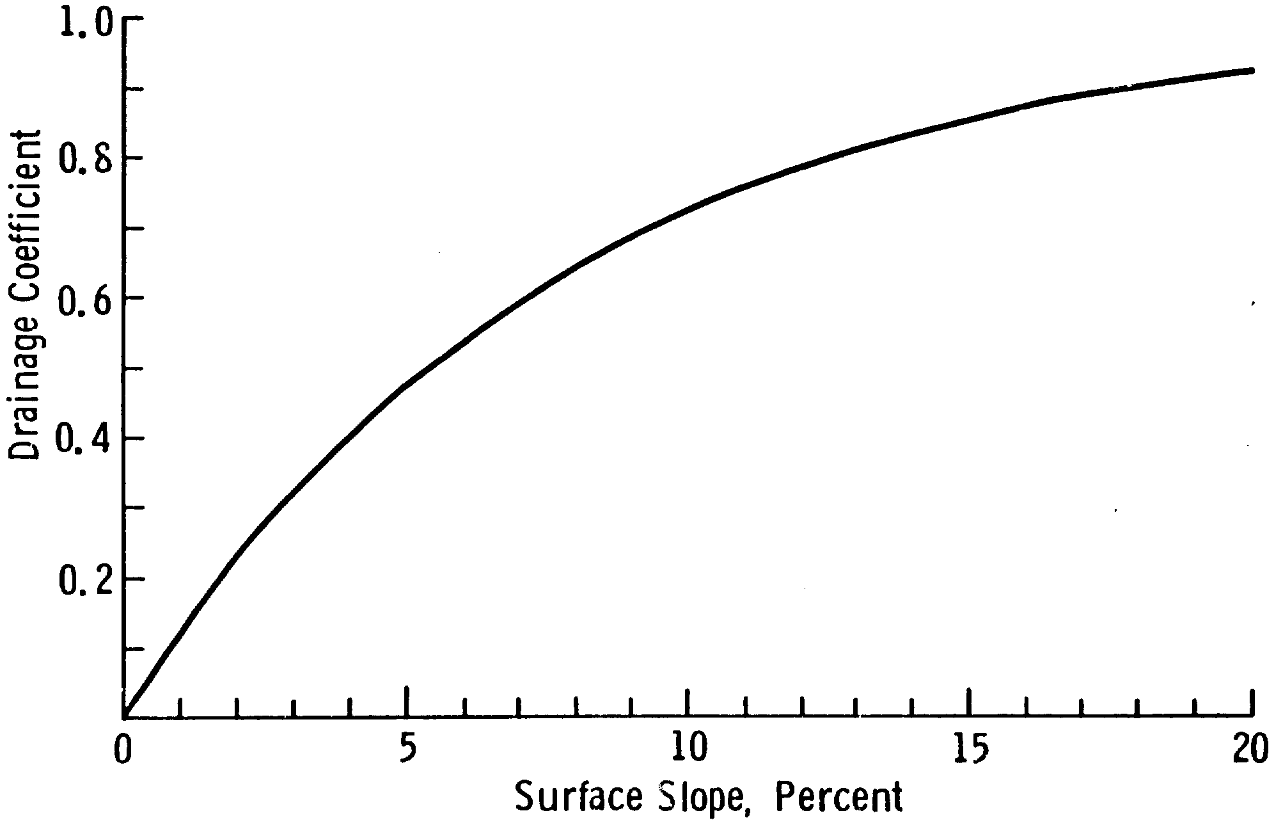

Figure 2.5. Variation in drainage coefficient as a function of soil surface slope in the soil water accounting model (SWAM).

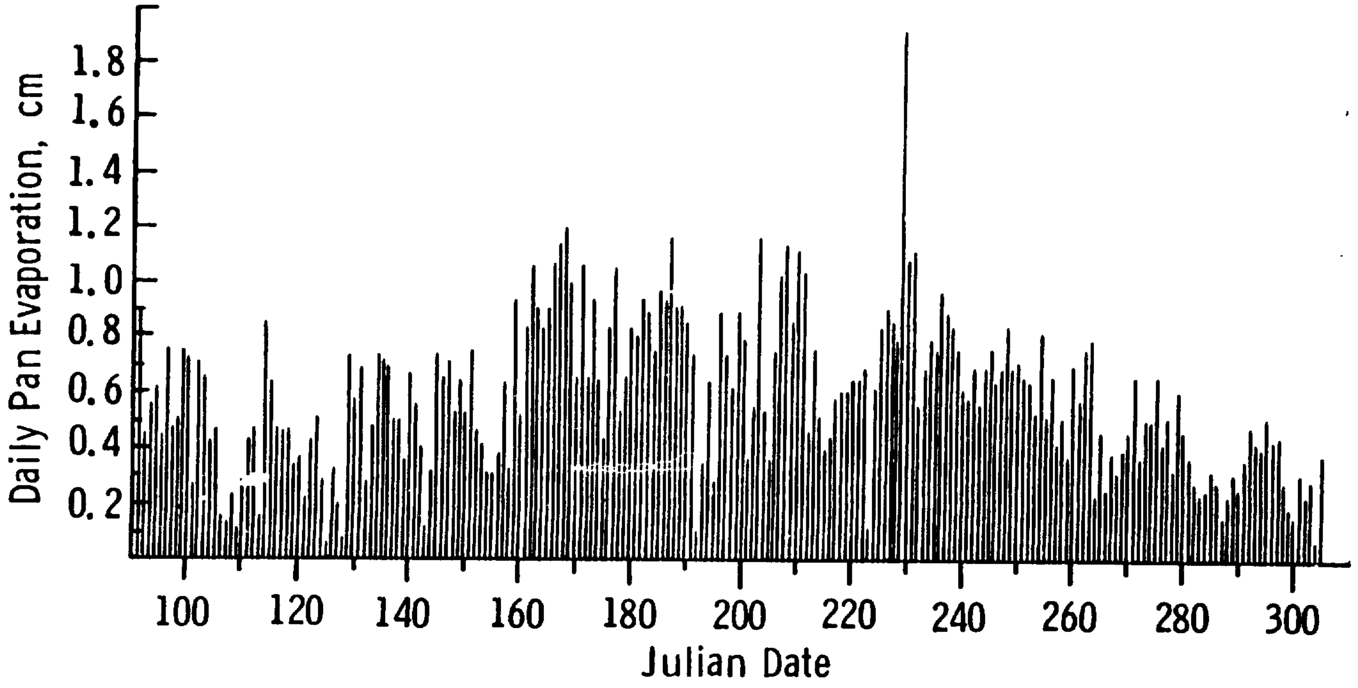

Figure 2.6. Daily pan evaporation recorded at Clinton Reservoir, Kansas during 1978.

$$AE = PE[A + B(MR) + C(MR)^2 + D(MR)^3] \quad (2.6)$$

where A, B, C, and D are empirically derived coefficients dependent upon PE [13], and the moisture ratio MR is given by

$$MR = (SM - WP)/(FC - WP) \quad (2.7)$$

where SM = the measured soil moisture,

WP = the wilting point of the soil, and

FC = the field capacity of the soil, and $0 \leq MR \leq 1.0$,

and the potential evaporation PE is

$$PE = k_p * E_{pan},$$

where k_p = pan coefficient and

E_{pan} = measured pan evaporation,

Regression fits of experimental data yield [13]:

$$A = -0.05 + 0.732/PE \quad (2.8)$$

$$B = 4.97 - 0.661\ PE \quad (2.9)$$

$$C = -8.57 + 1.56\ PE \quad (2.10)$$

$$D = 4.35 - 0.88\ PE \quad (2.11)$$

Thus, for a given day, all terms in Eq. 2.6 are constant for all grid cells except the moisture ratio, which is dependent on the antecedent soil moisture and the gross water-retention characteristics of each soil.

For vegetated soils, the actual evapotranspiration, ET_{crop}, is computed by a modification of the Blaney-Criddle formulation used in estimating crop irrigation requirements [8,21]. Although the method is designed for effective integration periods of weeks to months, the simplicity of its input requirements makes this a practical approach for such a large number of grid cells. Basically, crop consumption of water over the rooting depth varies with temperature, length of day, available soil moisture, crop type, crop stage of growth, relative humidity, and windspeed. To simplify the formulation, average measured values of temperature, day length, relative humidity, and windspeed are assumed on a seasonal basis for the simulation area. The resultant expression for ET_{crop} becomes [8]:

$$ET_{crop} = k_c * ET_o \qquad (2.12)$$

where kc = crop coefficient

ET_o = potential evapotranspiration.

While ET_o is generally computed on a mean monthly basis by the Penman equation, Eq. (2.12) becomes more sensitive to daily changes in root-zone soil moisture for $ET_o = AE$ as computed by Eq. (2.6) for the rooting zone.

Crop coefficient as adjusted for mean local climate is plotted in Figure 2.7 as a function of the number of days after planting for several of the crop covers included in the data base. Crop consumption of water is seen to be dependent on both crop type and stage of crop development.

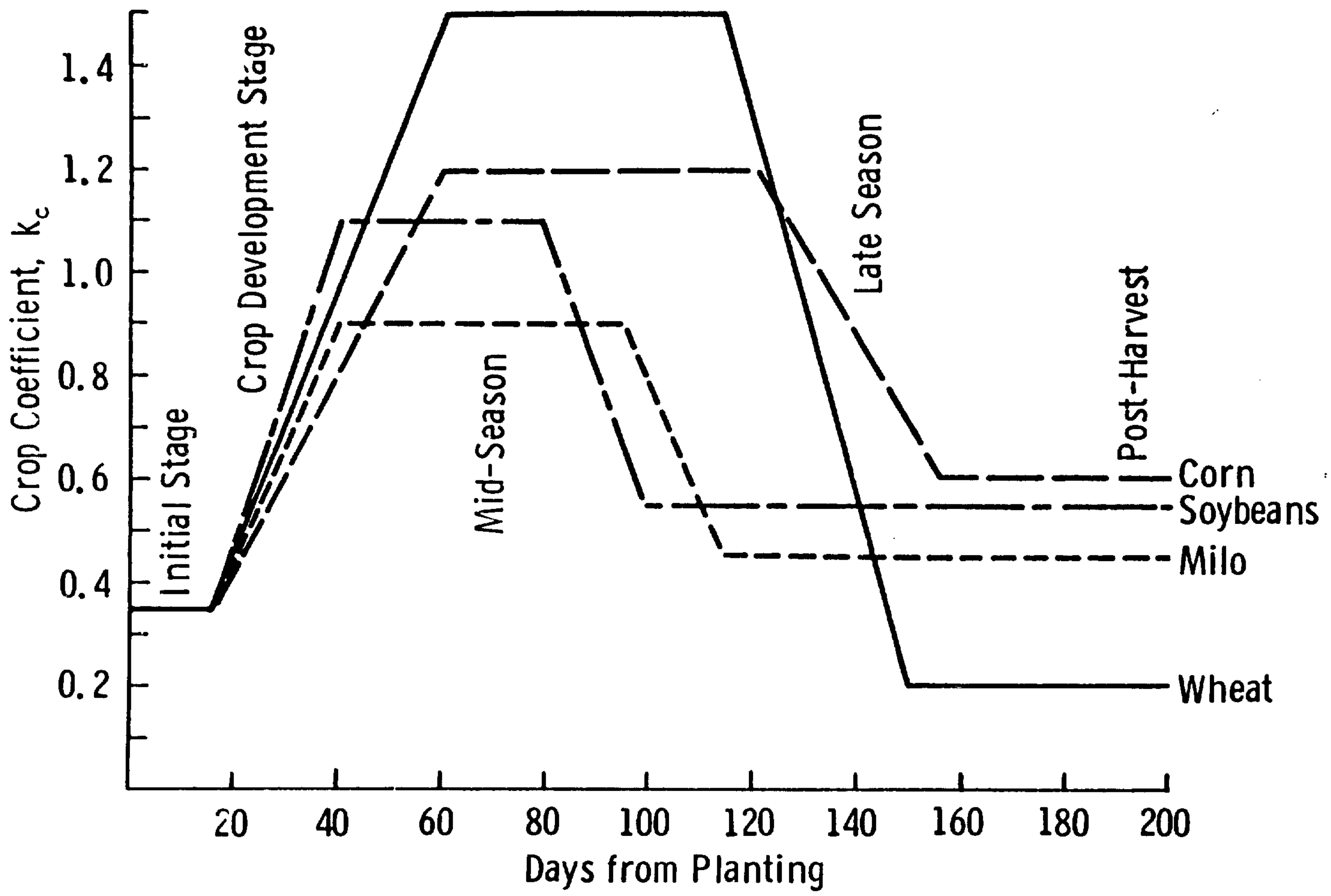

Figure 2.7. Crop transpiration coefficient as a function of time from planting for several representative crops found within the simulated area.

2.4 Crop Development Model

The lengths of time required for a given agricultural field in the simulation data base to progress from one crop-development stage to the next is established from data gathered by the Statistical Reporting Service of the United States Department of Agriculture. Figure 2.8 shows the crop reporting districts. The simulation area lies at the northern limits of the East Central reporting district of Kansas (No. 6). Figure 2.9 presents a summary of mean crop development over a 10-year period as enumerated by AgRISTARS [15] for this crop reporting district. These percentages are used to define crop development stage within the simulation on a field-by-field basis. Thus, each distinct agricultural field in the data base is assigned one of ten codes which allows that field to be individually allocated to one of 10 planting dates. Hence, there are ten different absolute crop calendars possible for each crop type identified in Table 1.3.

Planting dates are randomly assigned to field codes for a specific crop based upon Figure 2.9. This procedure results in the introduction of a significant source of between-field variance of soil moisture within a given crop type due to the effect of crop development stage on evapotranspiration. It also allows for a given field to have its target classification changed in Table 1.3, since a medium-rough bare field becomes a cropped field after emergence, and finally reverts to bare soil status after harvest. As implemented, this procedure gives the data base a dynamic crop-category mix that can be modified to match regional agricultural practices such as double cropping or dynamic soil surface roughness conditions.

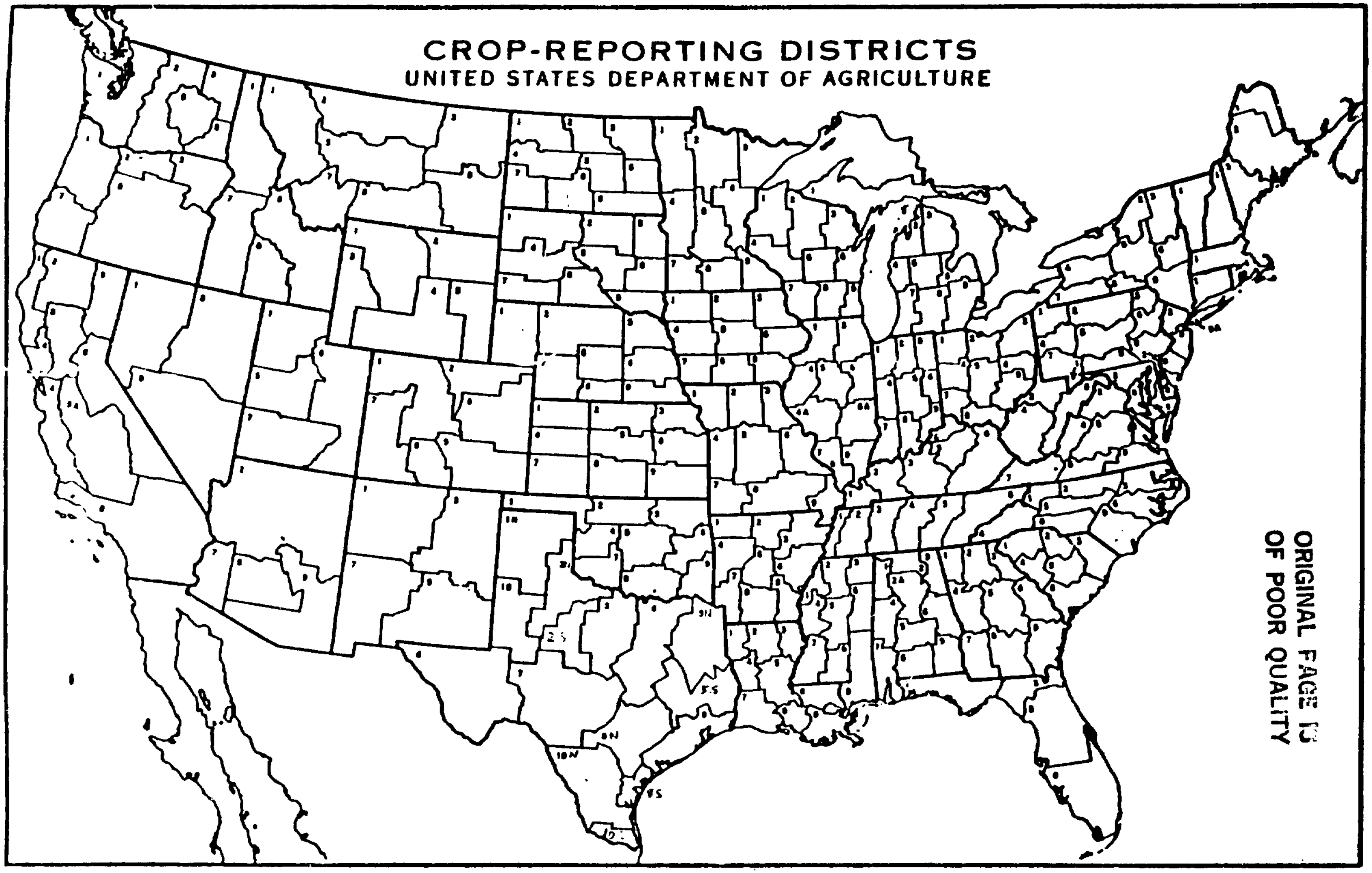

U. S. DEPARTMENT OF AGRICULTURE NEG. 24280 A Statistical Reporting Service

Figure 2.8. Crop reporting districts of the USDA from [14].

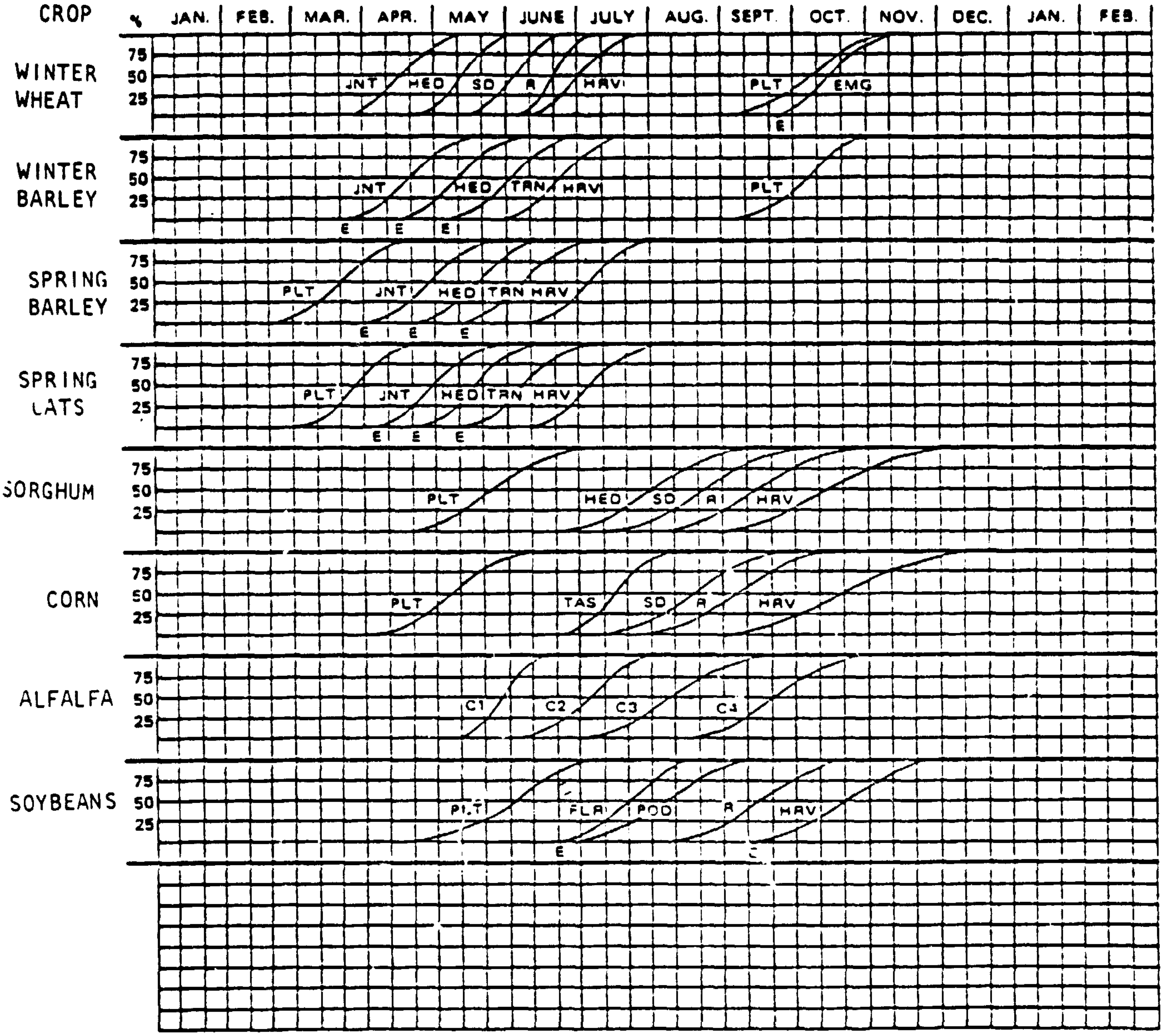

LEGEND

E	Under stage name, indicates rough estimate of date
EMG	Emergence
HED	Heading
HRV	Harvest
JNT	Jointing
PLT	Planting
R	Ripe
SD	Soft dough
TRN	Turning
FLR	Flowering
C	Cut
TAS	Tasseling

Figure 2.9. Percent of crop area in development stage by specified date for Kansas crop reporting district 6 average crop calendars from 1963 to 1973 [15].

2.5 Interlayer Water Redistribution

Infiltration of water into the surface layer, percolation of water into the root zone, and capillary recharge of surface layer moisture are controlled by the water-potential profile as limited by soil structure. Applying Darcy's formulation to the flow in unsaturated soils yields:

$$V = K(\theta) * \nabla H \qquad (2.13)$$

where

V = the flow velocity,

$K(\theta)$ = the hydraulic conductivity as a function of volumetric soil moisture θ, and

∇H = the gradient of the hydraulic head H.

For the soils included in the data base, the volumetric moisture θ is approximately known only at matric potentials of 1/3 bar and 15 bars, and no ready data source exists for $K(\theta)$ except at saturation. Therefore, the approach given by Eq. (2.13) for laboratory measurements or modifications based on field measurements [6] is not tractable. However, a rough first-order approximation of the effect of $K(\theta)$ on flow rate V is incorporated which allows K to decrease in a linear fashion from that measured at saturation as given by:

$$V = K_{sat} * \left(1.0 - \frac{\theta_{max} - \theta}{\theta_{max}}\right) \qquad (2.14)$$

where K_{sat} = measured saturated hydraulic conductivity

θ_{max} = porosity, and

$\theta_{max} = 1 - \rho_b/\rho_s$

ρ_b = soil bulk density, g/cm^3

ρ_b = soil specific density, g/cm^3

Assuming that all the soils in the data base have a specific density of 2.65 g/cm^3, Eq. (2.14) reduces to:

$$V = 2.65\theta K_{sat}/(2.65 - \rho_b) \cdot \qquad (2.15)$$

It is recognized that this approximation can seriously overestimate K(θ) of clays at low moisture contents as shown in Figure 2.10. However, since the function is uniformly applied to infiltration at the surface and to percolation into the root layer, the net effect of this error on surface-layer moisture will be reduced after several accounting periods inasmuch as water will readily drain, and it is the surface water content that drives the radar simulation model.

In addition, several limiting conditions are placed on percolation and capillary recharge. Percolation only takes place when surface-layer moisture exceeds field capacity and only to the extent that surface- layer moisture is reduced to field capacity. Also, capillary recharge is only considered as significant when evapotranspirative losses have reduced the surface-layer soil moisture below the wilting point, thus allowing for the formation of a discontinuity in moisture at the layer boundary that is related to the formation of a surface crust.

While the above approach is not rigorous, it allows for the ready calculation of approximate flows with the proper directionality and requires minimal inputs and computation for the very large number of

ORIGINAL PAGE IS
OF POOR QUALITY

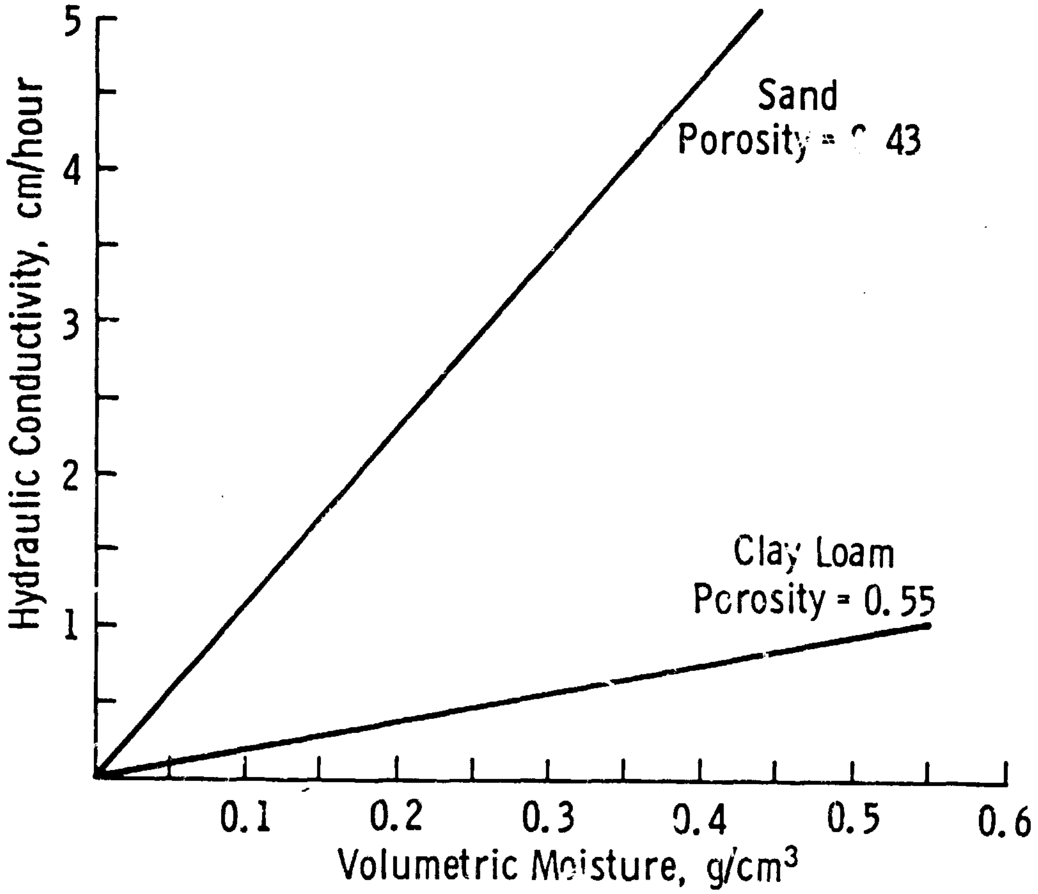

Figure 2.10. Hydraulic conductivity as a function of volumetric soil moisture.

grid cells in the data base. An alternate approach [19] can be used for soils where $K(\theta)$ is measured for each soil at a low value of moisture:

$$K(\theta) = K_{sat} * \exp[\alpha * (\theta-\theta_{max})] \qquad (2.16)$$

where α is a free parameter set to fit the measured values.

2.6 Within-Field Variability in Surface Soil Moisture

Prior to radar image simulation, the surface layer soil moisture values determined by SWAM for each 20-m x 20-m grid cell are randomized to approximate the natural variability in soil moisture measured within "homogeneous" fields. Rather than rely on field-based studies of moisture variance for various plot sizes as computed from point-sampling techniques [17-20], a variance estimate based on areal measurements of soil moisture at a scale close to 20 m x 20 m is deemed more appropriate.

The areal surface-moisture sampling instrument considered is the 4.75-GHz airborne scatterometer flown by NASA/JSC over a test site near Colby, Kansas in July and August 1978. The test site consisted of forty-two 40-acre agricultural fields selected because of their expected within-field homogeneity. While the 260-km^2 test site was overflown seven times, data from only the first six flights are used in this analysis; the last flight produced acceptable scatterometer data but suffered from a camera malfunction which makes ground referencing of the backscatter data uncertain. The 4.75-GHz fan-beam scatterometer was flown at a mean altitude of 460 m and the data was processed by

NASA/JSC and averaged over 0.5-second time intervals. At a typical aircraft ground speed of 278 km/hour, this yields a reported scatterometer fore-aft ground resolution of 37 m. Since the cross-track 3-dB beamwidth is 3 degrees for the 4.75-GHz scatterometer, at a 10-degree angle of incidence, the cross-track resolution becomes 25 m. The radar backscattering coefficient σ^0 from this 37-m x 25-m resolution element is the mean of 90 independent samples from frequency averaging as calculated by

$$N_f = 2(\Delta D)^2 \cos^3\theta/\lambda h \qquad (2.17)$$

where:

N_f = number of independent samples produced by frequency averaging,

ΔD = fore-aft ground resolution,

θ = angle of incidence,

h = aircraft altitude, and

λ = wavelength.

For 90 independent samples, the uncertainty in σ^0 due to fading is less than +/- 0.15 dB assuming Rayleigh fading statistics; hence, the scatterometer's measurement precision can be considered to be quite good.

For the 40-acre test fields at Colby, the variance in 0-5-cm soil moisture has a mean value of 6.5 percent on a gravimetric basis from 45 sampling locations in each of 154 field observations [22]. Ignoring fields with crop row direction orthogonal to the aircraft flight path, the least-squares linear correlation between 0-5-cm soil moisture and σ^0(dB) is found to be 0.80 when comparing field mean values of σ^0 with moisture at an incidence angle of 10 degrees and HH polarization [16], and 0.92 (Figure 2.11) when comparing σ^0 on a subfield basis with the nearest point measurements of soil moisture [23] at an incidence angle of 15 degrees. While both of the above sets of linear correlation results are based upon only the first two flights, the addition of data from all six flights does not significantly alter the strength of the linear correlation between σ^0 (dB) and near-surface moisture. In a comparison of field averages of moisture and σ^0, the linear correlation ρ is found to vary between 0.82 at 10 degrees and 0.87 at 15 degrees.

Due to the variability in sampled soil moisture found even within small plots, and due to sampling error [17 to 20], the maximum linear correlation coefficient attainable is limited, even for a perfect moisture sensor, by the variance in point-sampling error. For point-sampling error distributed with a zero mean and a variance of σ_n^2, and assuming moisture and sampling error to be independent, it can be shown that [24]

$$\rho(\sigma^0, \hat{M}_{SM}) = \left[\frac{1}{1 + \frac{\sigma_n^2}{\sigma_{SM}^2}}\right]^{\frac{1}{2}} \tag{2.18}$$

where

$\hat{M}_{SM}$ = mean soil moisture estimate,

σ_n^2 = sampling error variance, and

σ_{SM}^2 = true soil moisture population variance.

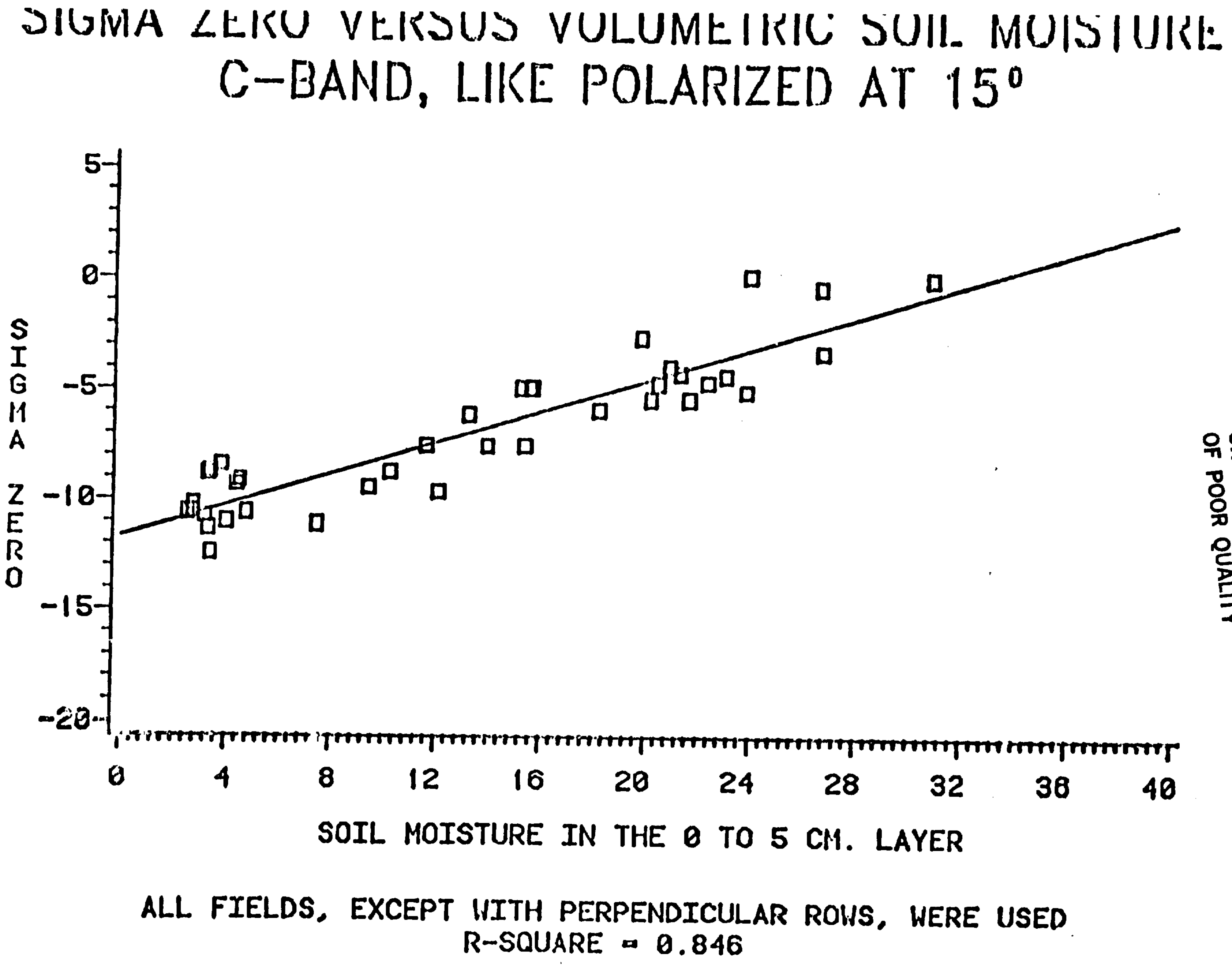

Figure 2.11. Aircraft scatterometer response to surface soil moisture from first two flights at Colby, Kansas from [23].

Equation (2.18) shows the correlation coefficient to be inversely proportional to sampling error variance and directly proportional to the true variance of soil moisture. Thus, assuming that the true soil moisture variance is that measured within the Colby test fields, σ^2_{SM} = 6.5%, and assuming that the sampling error variance is within the range found for dry soil sample weights less than 100 grams [20], $0.8\% \lesssim \sigma^2_n \lesssim 2.0\%$, then the maximum linear correlation coefficient calculated from Eq. 2.18 is $0.87 \lesssim \rho \lesssim 0.94$. As a result, it is not statistically unreasonable to assume that the scatterometer is a perfect moisture mapper.

Assuming for the moment that the intrafield variance in crop canopy conditions and random surface roughness is small enough to be negligible, and assuming that the variance in radar backscatter at 4.75 GHz, HH polarization at a 10-degree angle of incidence is solely dependent in a linear fashion on surface soil moisture, the Colby 4.75-GHz aircraft scatterometer data can be used to define an estimate of the natural variance in the true soil moisture population between sensor resolution cells of 37 m × 25 m. Figure 2.12 shows a measure of within-field variance in σ^o, CV, plotted as a function of σ^o.

$$CV = 10 \log \left(1 + \frac{SD_{\sigma^o}}{\bar{\sigma}^o}\right) \qquad (2.19)$$

where:

CV = variance coefficient,

SD_{σ^o} = within-field standard deviation in σ^o, m/m, and

$\bar{\sigma}^o$ = field mean σ^o, m/m.

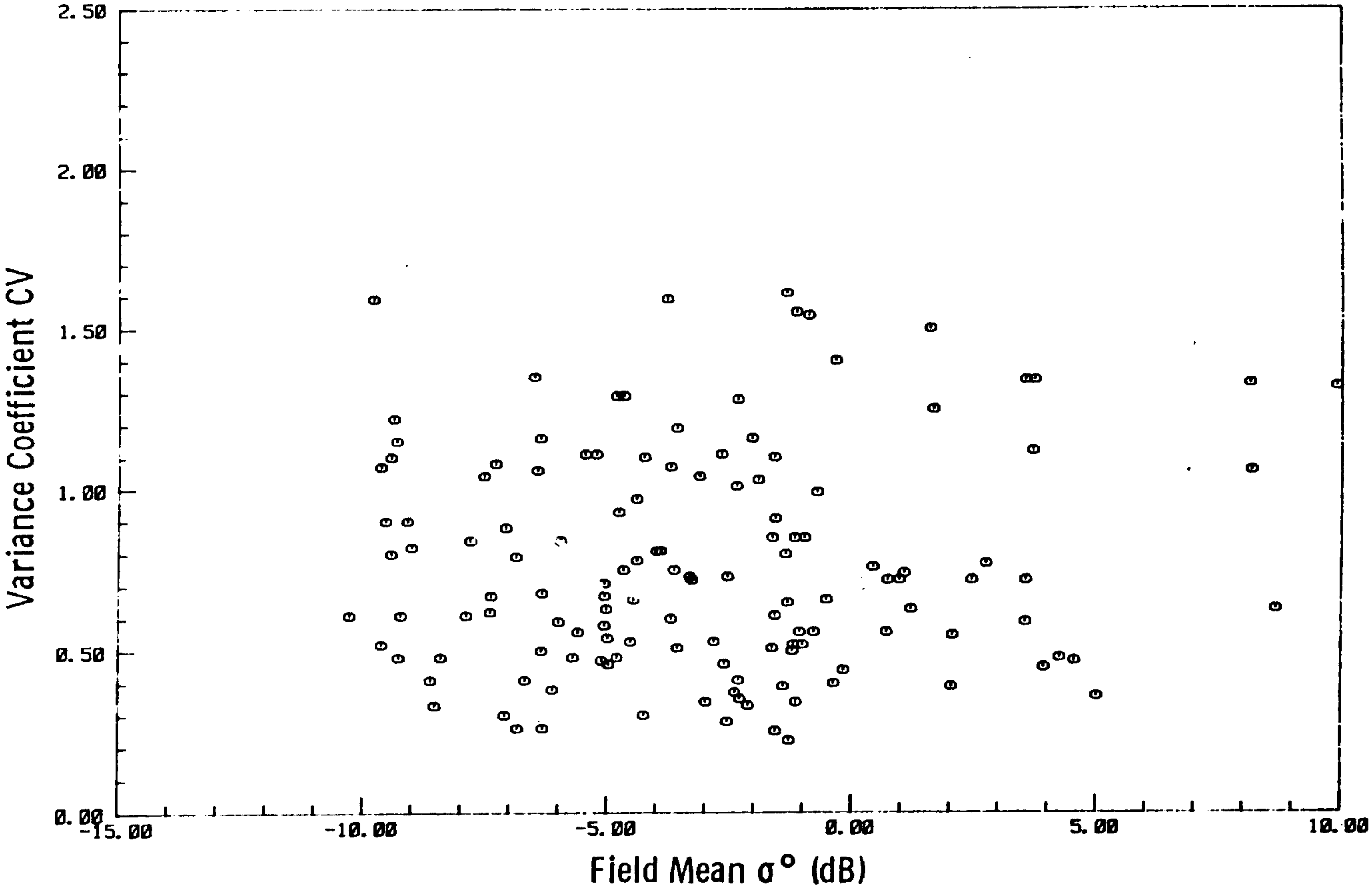

Figure 2.12. Variance in aircraft radar backscatter due to intrafield variability of moisture for "homogeneous" test fields at Colby, Kansas in 1978. Scatterometer characteristics are 4.75 GHz frequencies, HH polarization, 10° angle of incidence, and a nominal resolution of approximately 30 meters.

For sample sizes between 6 and 10, the within field variance of σ^o is seen to be independent of $\bar{\sigma}^o$ which, for a perfect soil moisture mapper, implies that CV is independent of soil moisture (which ranged from the wilting point to saturation over the course of the six flights at the Colby site). The mean value of CV is found to be 0.78, which corresponds to an average within-field uncertainty in $\bar{\sigma}^o$ of + 0.78 dB to - 0.95 dB. Application of these uncertainties to the empirical smooth bare soil regression equation between σ^o (dB) and 0-5-cm soil moisture

$$\sigma^o(\mathrm{dB}) = 0.149\, M_{FC} - 15.49 \qquad (2.20)$$

where:

M_{FC} = 0-5 cm percent of field capacity,

yields an uncertainty in M_{FC} of + 5.2% to - 6.4%.

The output of the SWAM budget model for the 0-5-cm soil layer is randomized on a grid-cell basis by a Gaussian random-number generator with a standard deviation of 6 percent M_{FC}. This within-field moisture variance is added by pixel for each moisture distribution prior to calculation of the mean grid cell σ^o in the target-sensor interaction model for radar image formation.

An image format example of the impact of the SWAM plus within-field variance in 0-5-cm soil moisture distribution is shown in Figure 2.13. The figure compares Moisture Condition 3 from the simple water budget [1] with the moisture distribution present over the same 3-km x 5-km portion of the data base as produced by SWAM on Julian day

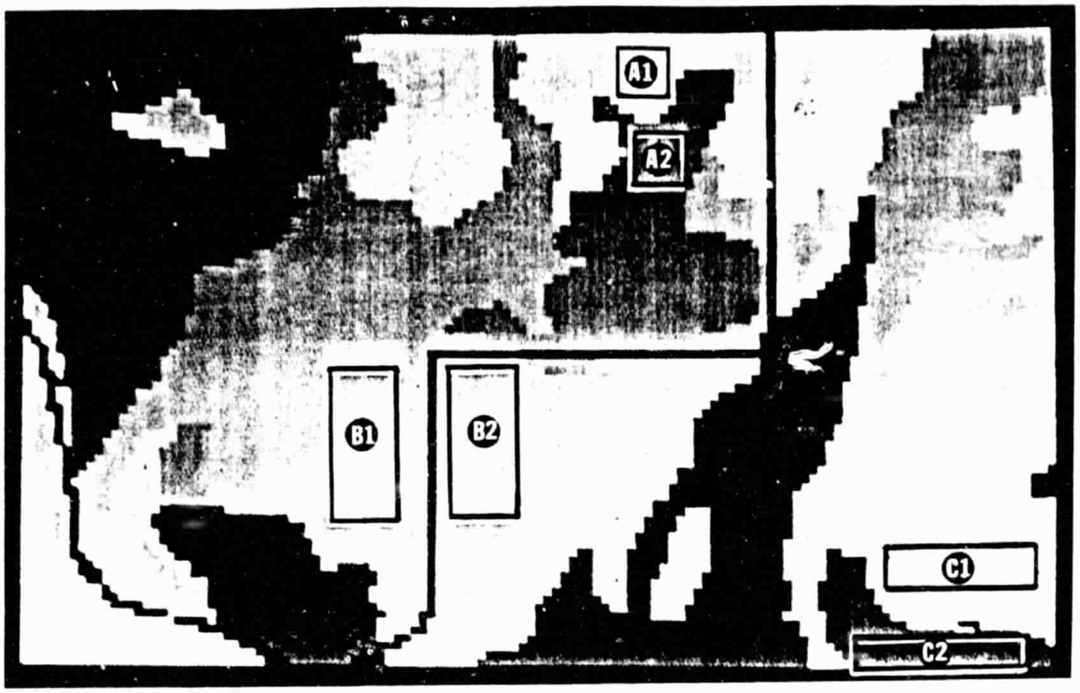

(a) Moisture Condition 3 from the simplified environmental model.

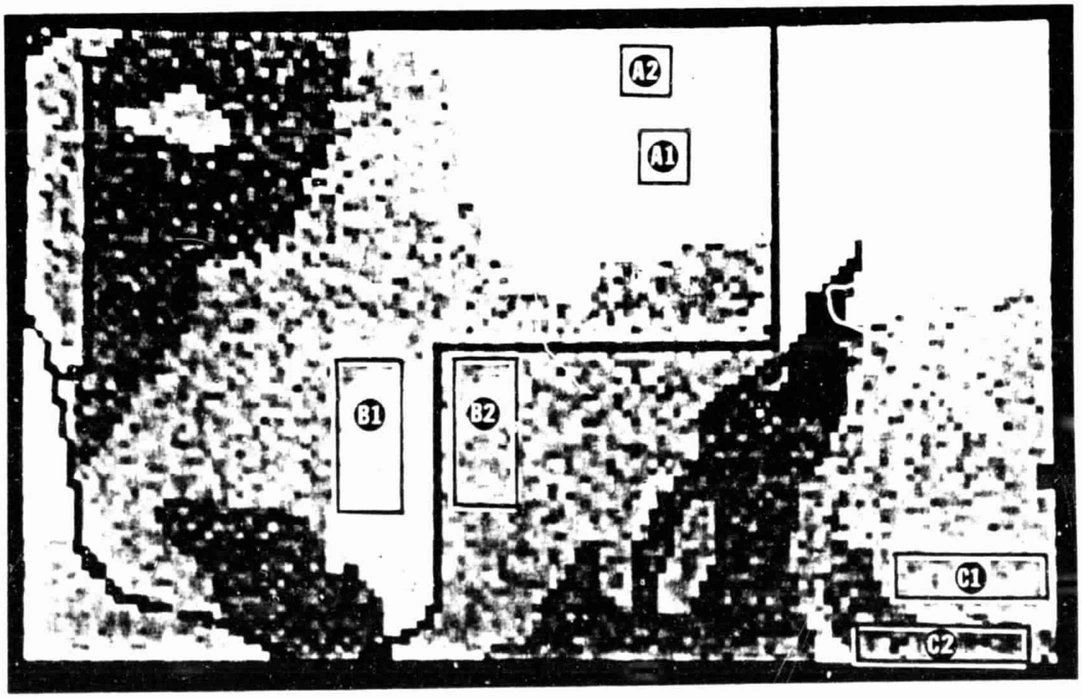

(b) Julian day 168 from the dynamic soil water accounting model (SWAM).

Figure 2.13. Comparison of the spatial distributions of soil moisture resulting from a) the simplified environmental model given by Table 1.3, and b) the dynamic soil water accounting model. The general soil moisture conditions are similar for both models and grey tone is proportional to moisture.

TABLE 2.1

Comparison of Mean Soil Moistures from the Simplified Environmental Model with those from the Dynamic Soil Water-Accounting Model for the Same Agricultural Fields Under Similar Regional Moisture Conditions

Field[*]	Soil	Crop	Moisture Map ∇	Mean % of Field Capacity	S.D.	Number of Pixels
A1	Loam	Pasture	MFC 3	32.0	0	36
A1	Loam	Pasture	Day 168	97.17	2.04	36
A2	Silty Clay Loam	Pasture	MFC 3	51.0	0	36
A2	Silty Clay Loam	Pasture	Day 168	97.17	1.94	36
B1	Silty Loam	Soybeans ⊥	MFC 3	52.0	1.98	180
B1	Silty Loam	Soybeans ⊥	Day 168	87.14	5.79	154
B2	Silty Loam	Smooth Bare	MFC 3	52.0	1.89	190
B2	Silty Loam	Smooth Bare	Day 168	66.40	5.50	170
C1	Silty Loam	Soybeans ⫫	MFC 3	57.0	0.55	114
C1	Silty Loam	Soybeans ⫫	Day 168	66.33	6.07	102
C2	Sandy Loam	Soybeans ⫫	MFC 3	25.0	0.0	60
C2	Sandy Loam	Soybeans ⫫	Day 168	44.90	4.97	60

[*] Field number corresponds to those noted on Fig. 2.9.

[∇] MFC "N"--"N" refers to moisture condition in Table 1.3.
Day "X"--"X" refers to Julian day in dynamic soil water-accounting model.

168. The means and standard deviations of the identified fields are given in Table 2.1. Image graytone is proportional to moisture content in Figure 2.13; the upper image from the simple water budget is comparable (M_{FC} 10% to 30% drier) in mean moisture to the lower image from Julian day 168 as produced by SWAM. The impact of the addition of within-field variance in moisture is immediately evident. The impact of crop type in SWAM is exemplified by comparing Fields B1 and B2 in both images. In Figure 2.13a, both fields have a mean 0-5-cm soil moisture of 52% of field capacity while SWAM yields a mean moisture of 87% and 66% for the soybean and bare fields respectively (with both fields having identical rain histories). The impact of soil type in both models is most apparent when comparing portions of the Soybean Field C, which is partly located on a silt loam (C1) and a sandy loam (C2).

The final moisture distributions for the radar image simulations detailed in Section 3 are shown in Figure 2.14. The dynamic soil water accounting model was initialized on Julian day 153 and the output sampled every five days. The resultant distributions were then examined and the three most closely approximating moderately dry, moist, and wet soil surface conditions were selected for radar image simulation. The distribution presented for day 173 in Figure 2.14 shows that a minimum of approximately 4.0% of all grid cells contain soils at saturation and are potentially under standing-water conditions. This does not seem unreasonable when considering that a minimum of 5 cm of rain fell across the data base on the previous day. In large part, the saturated conditions exist beneath the center of the storm track where rainfall approached 9 cm and for poorly drained clay

**ORIGINAL PAGE IS
OF POOR QUALITY**

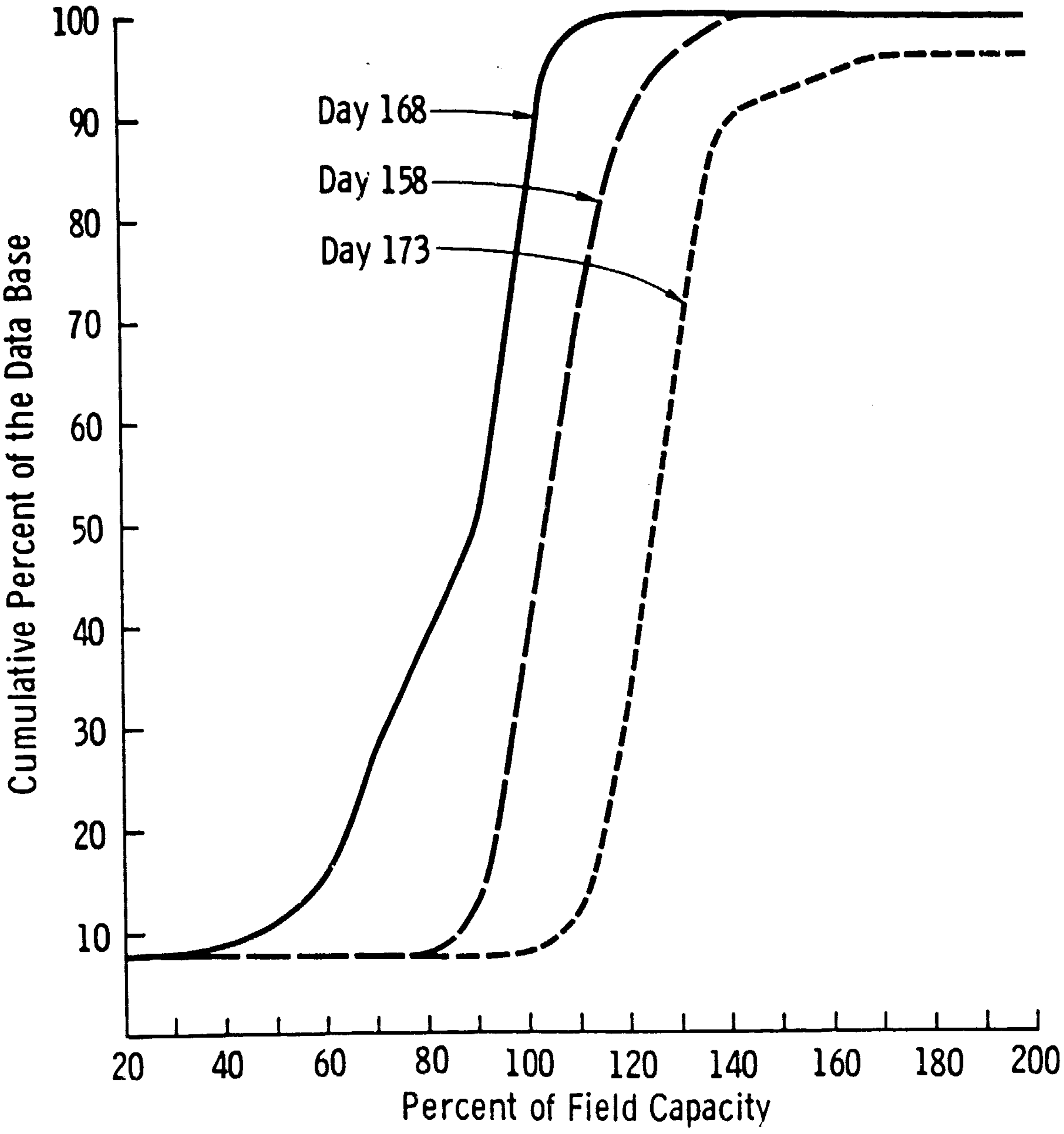

Figure 2.14. Actual soil moisture distributions as output by the dynamic soil-water accounting model on Julian days 158, 168, and 173 for 20 m grid cells.

soils. The effect of this local flooding is apparent on the simulated radar imagery in Section 3.0. Image presentations of 0-5-cm soil moisture distribution for Julian days 158, 168, and 173 are shown on Figure 2.15.

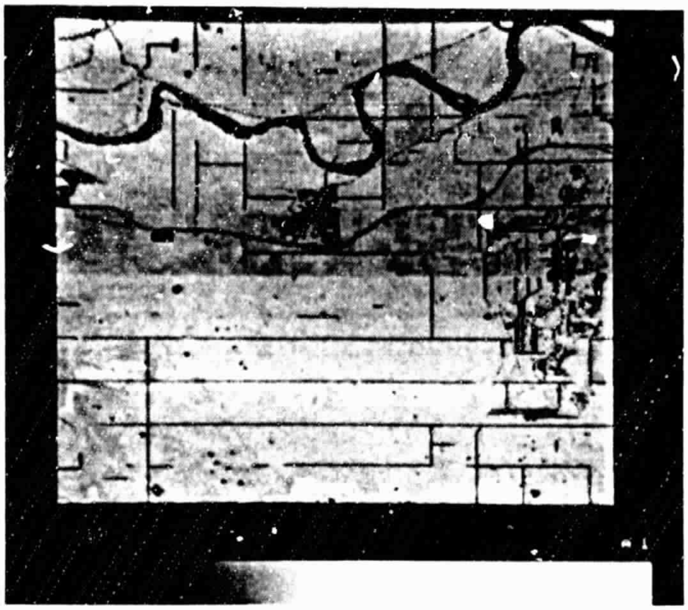

a) day 158

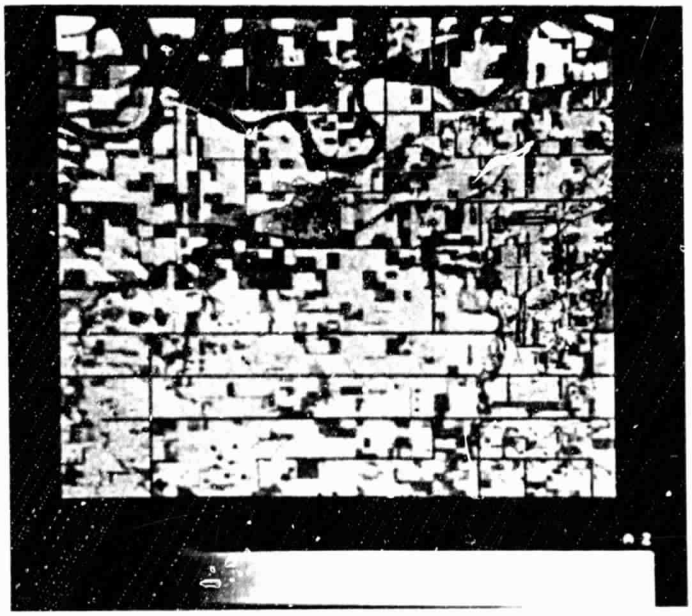

b) day 163

Figure 2.15. Image display of 0-5 cm soil moisture distributions established by the dynamic soil water accounting model on Julian days: 158, 163, and 1 3. Percent of field capacity is proportional to image intensity.

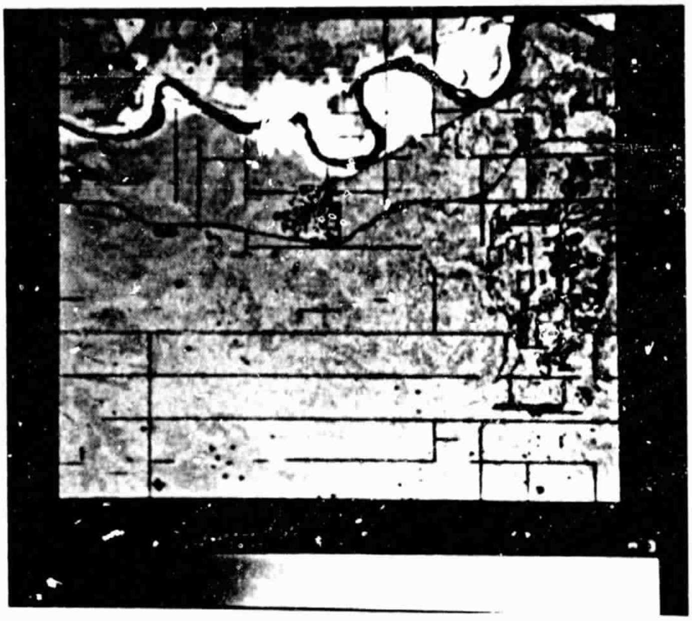

c) day 173

3.0 RADAR SIMULATION STUDY

The objective of this series of radar image simulations is to reexamine prior conclusions regarding soil moisture estimate accuracy [1,2] with respect to the resolution of an orbital C-band radar for the more complex spatial distributions of soil moisture generated by SWAM. In addition to the three SAR configurations previously modeled [1,2] with nominal resolutions of 20 m, 100 m, and 1 km (Cases 2, 4, and 8 respectively, in Table 1.2), an orbital real-aperture radar (RAR) with a nominal resolution of 3 km (Case 12 in Table 1.2) is also simulated.

The simulation's data base and procedures are identical to those detailed in the previous study [1,2] except for the terrain category reassignments and the variability in moisture distribution imposed by SWAM. The mean backscatter coefficient for each grid cell is computed from empirically determined functions for each target class relating local incidence angle, 0-5-cm percent of field capacity, surface roughness, and row direction to the mean radar backscatter coefficient. The effects of row direction on radar backscatter are defined as those that are experimentally measured for dry-land farming practices followed within the simulated region, and row directions are randomly distributed among fields with a 0.5 probability of being either parallel or perpendicular to the simulated radar look direction.

The Julian dates of simulated satellite overpasses and the system-design options of the simulated images are given in Table 3.1. The high-resolution SAR systems (20-m and 100-m resolutions) are simulated for all three moisture distributions (Figures 2.14 and 2.15) in order to examine the effects of moisture level and relative moisture distribution function on soil moisture estimate accuracy. The effects

TABLE 3.1

Simulated System Design Cases and Julian Dates of Satellite Overpasses

Approximate System Design Case from Table 1.2	Resolution at Mid-Range Angle $r_a \times r_y$ (m x m)	Angular Range θ	Simulation Label for Julian Dates of Satellite Overpasses		
			158	168	173
2	20 x 20	7.5°-9.3°	A1	A2	A3
4	93 x 100	7.5°-9.3°	B1	B2	B3
8	1000 x 1000	7.5°-9.3°	C1		
12	2600 x 3100	7.5°-9.3°	D1		

of varying radar resolution and the resolution of the resultant soil moisture estimate are examined for all system design configurations using the moderately moist soil water distribution on Julian day 158 as a standard for comparison.

The simulated images for each condition in Table 3.1 are presented in Figures 3.1 to 3.9. The image tone (brightness) is linearly scaled to received power in dB; the log transform is made in order to present the full dynamic range of received power such that point sources saturate the image and shadows are in the noise.

3.1 Effects of Changing Soil Moisture Conditions

This section will concentrate on an analysis of the images presented in Figures 3.1 to 3.6. An examination of Figures 3.1 to 3.3 from an orbital SAR with 20-m resolution for Julian days 158, 168, and 173 reveal several interesting features resulting from SWAM.

The storm model produced convective rainfall across the upper quarter of the image swath on Julian day 154 and across the lower half of the image swath on Julian day 156. Simulated radar observation of the data base on Julian day 158 (Figure 3.1) shows the path of the second storm cell as a generally brighter image tone while the passage of the first storm cell is no longer discernable on the image after four days of evapotranspiration. In the moist areas in the lower half of the image, the field patterns are not as distinct as they are in the drier upper portion of the image. This is due in part to the fact that interfield variance in soil moisture becomes greater with drying conditions since SWAM responds differentially to crop type and crop stage. Also, the effects of local slope on radar backscatter act to

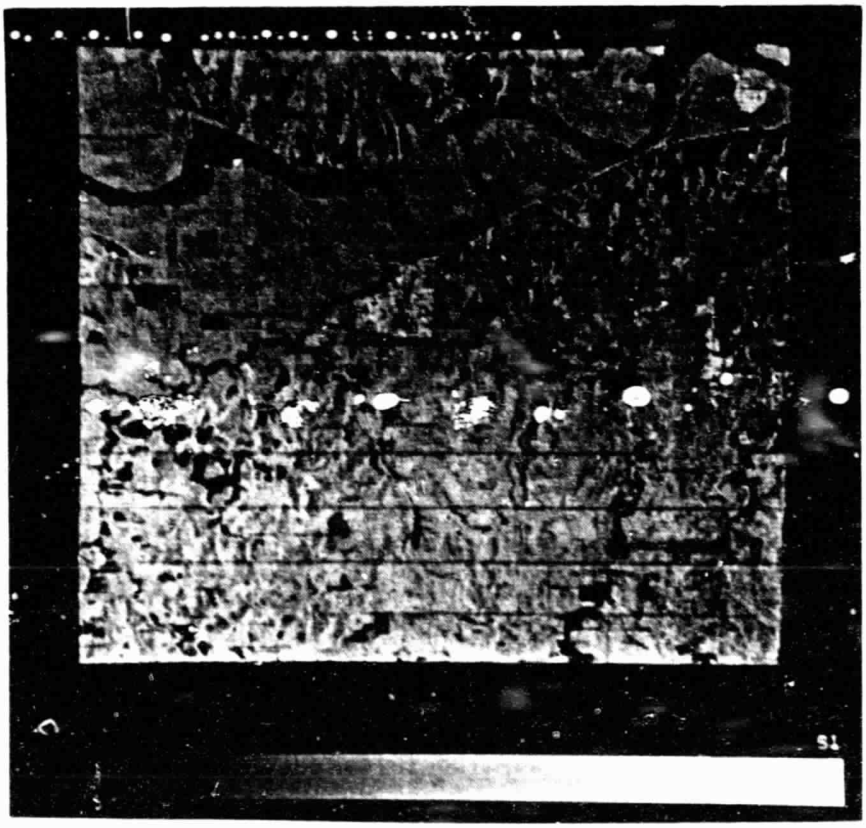

Figure 3.1. Simulated radar image A1 for 20 m resolution on Julian day 158.

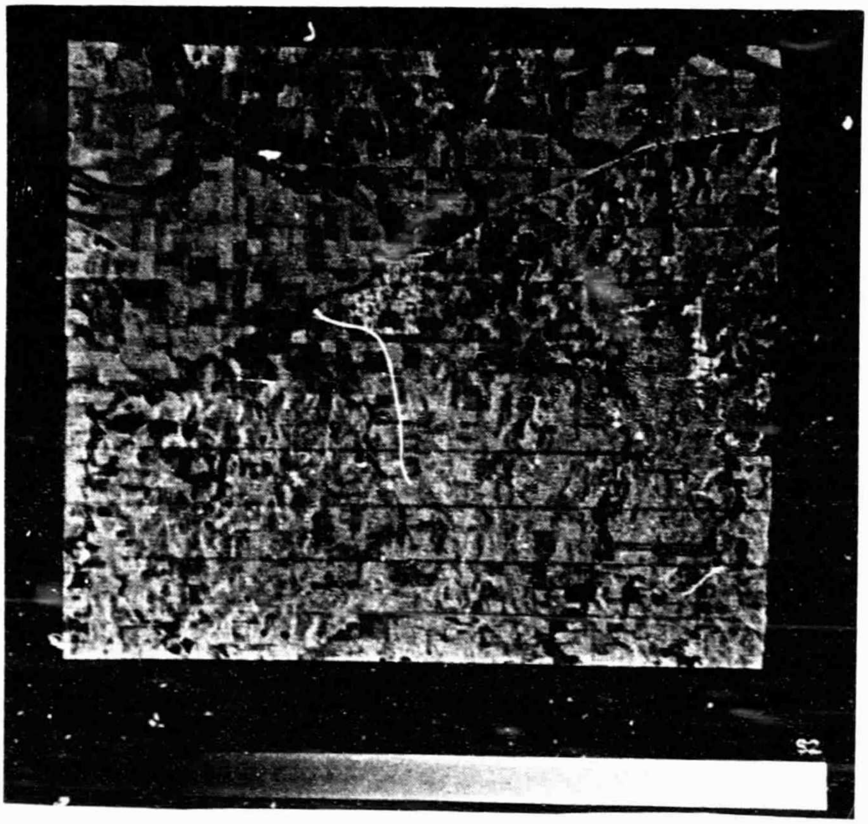

Figure 3.2. Simulated radar image A2 for 20 m resolution on Julian day 168.

Figure 3.3. Simulated radar image A3 for 20 m resolution on Julian day 173.

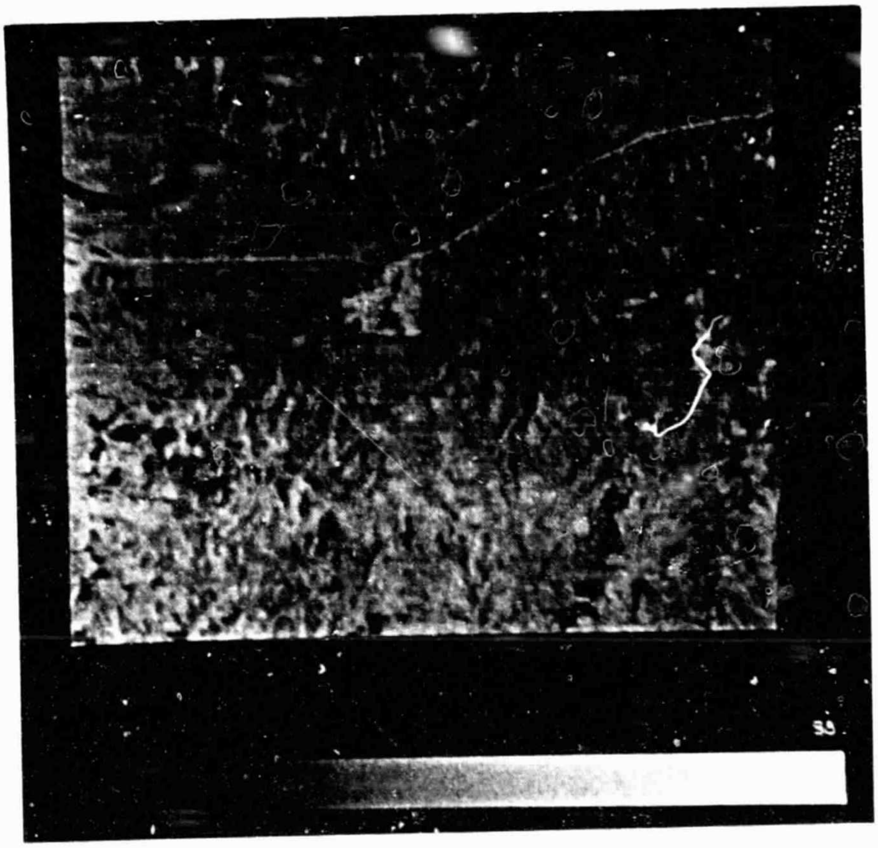

Figure 3.4. Simulated radar image B1 for 100 m resolution on Julian day 158.

ORIGINAL PAGE IS
OF POOR QUALITY

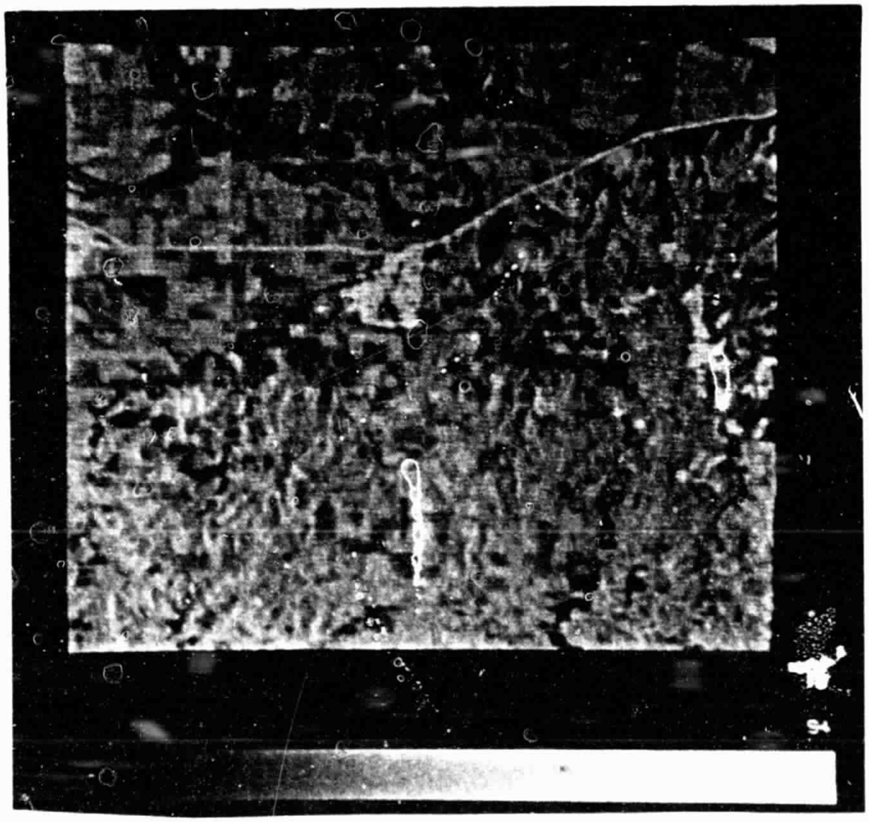

Figure 3.5. Simulated radar image B2 for 100 m resolution on Julian day 168.

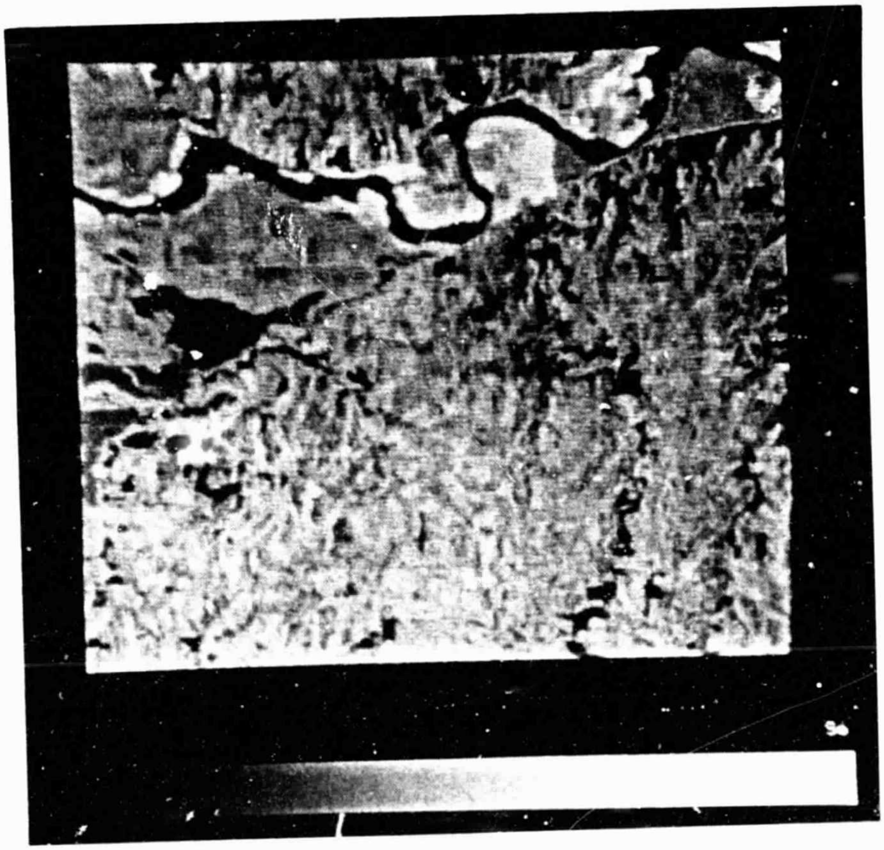

Figure 3.6. Simulated radar image B3 for 100 m resolution Julian day 173.

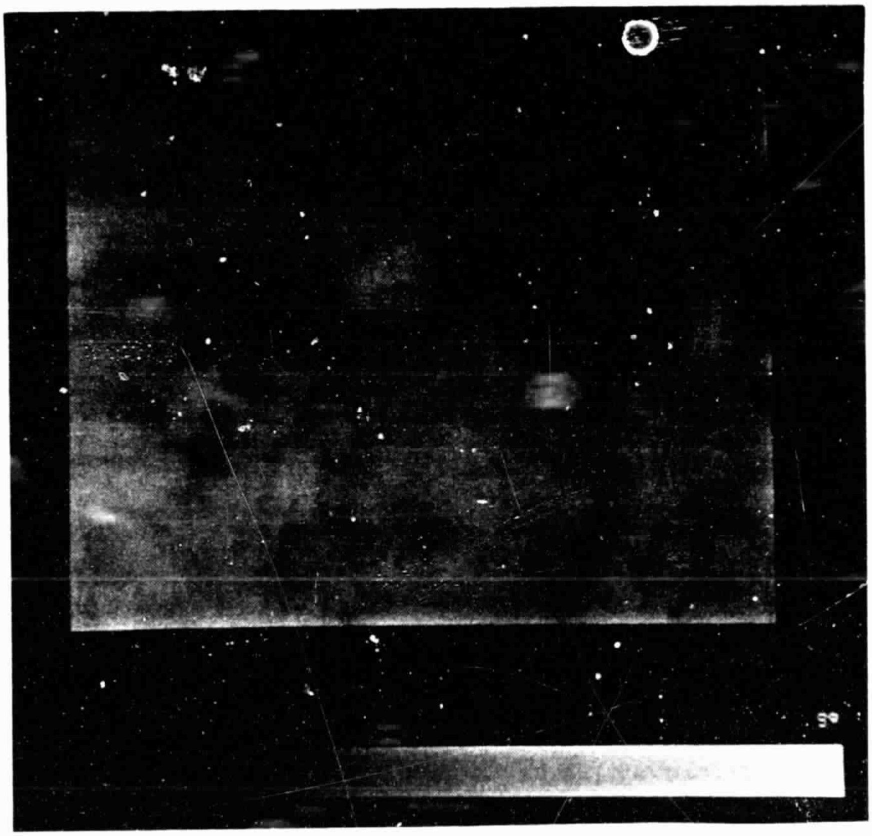

Figure 3.7. Simulated radar image C1 for 1 km resolution on Julian day 158.

ORIGINAL PAGE IS
OF POOR QUALITY

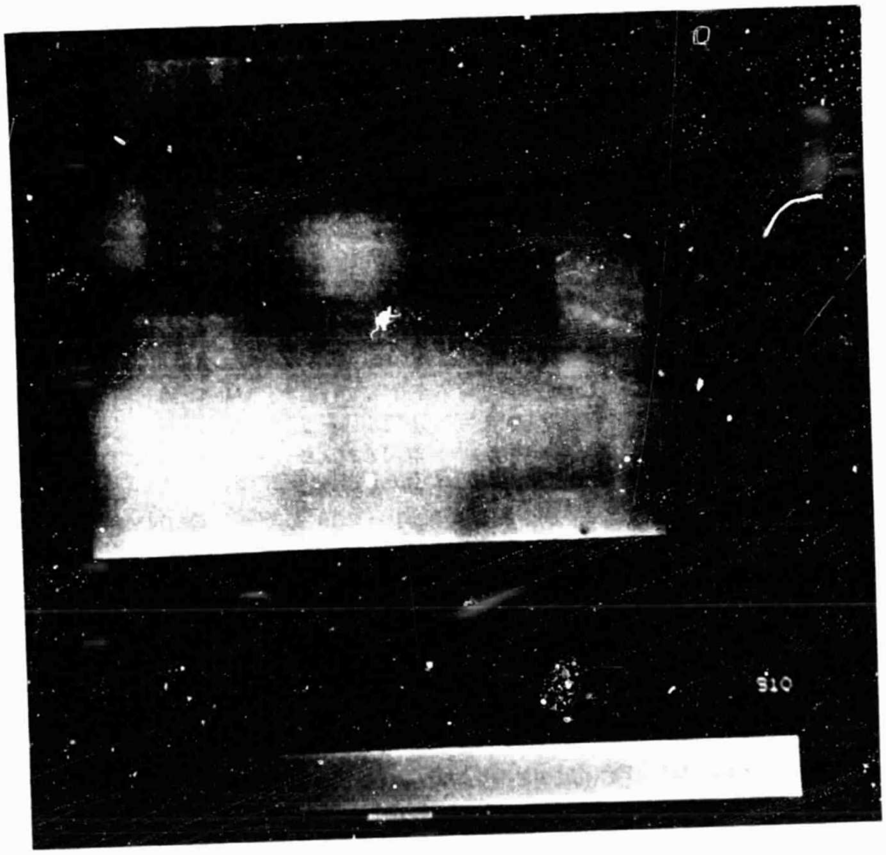

Figure 3.8. Simulated radar image D1 for 3 km resolution on Julian day 158.

reduce the discrimination of field boundaries in the hilly lower half of the image. This latter explanation is also applicable to Figure 3.2 for simulated imagery for which 10 days of drying have caused modal soil moisture to be reduced by 20 percent of field capacity.

On Julian day 172, a rather extensive storm has added 5 cm to 9 cm of rainfall over the test site, and simulated radar observation on the next day (Figure 3.3) shows that within the relatively flat region of the Kansas River floodplain (upper-left third of the image) the radar response is sensitive to conditions related to soil type and also is dependent upon field-controlled conditions. The roughly triangular dark region in the left center of the image is caused by the more specular reflection from poorly drained clay soils which are at saturation in the surface layer or are covered with standing water. This is interesting in that a "blind" moisture estimation algorithm (such as the one used [1,2]) which requires only received power and range to estimate soil moisture will predict that this area is dry soil when, in fact, it is saturated or flooded soil. This effect has been experimentally observed by truck-mounted scatterometers for these soils after rains of similar magnitude in 1977 [25]. Application of the moisture prediction algorithm given by Eq. 3.1 to Figure 3.3 shows this to be the case. In Figure 3.9, 20-m resolution radar estimates of soil moisture distribution are plotted for Julian days 158, 168, and 173. For Julian day 173, a comparison of actual and predicted moisture distributions, Figures 2.14 and 3.9 respectively, reveals that roughly 15% of the 20-m x 20-m grid cells reflect serious underestimates of 0-5-cm soil moisture. The clay loam soil with poor drainage occupies 13% of the 20-m x 20-m grid cells, and between Julian days 168 and 173

ORIGINAL PAGE IS
OF POOR QUALITY

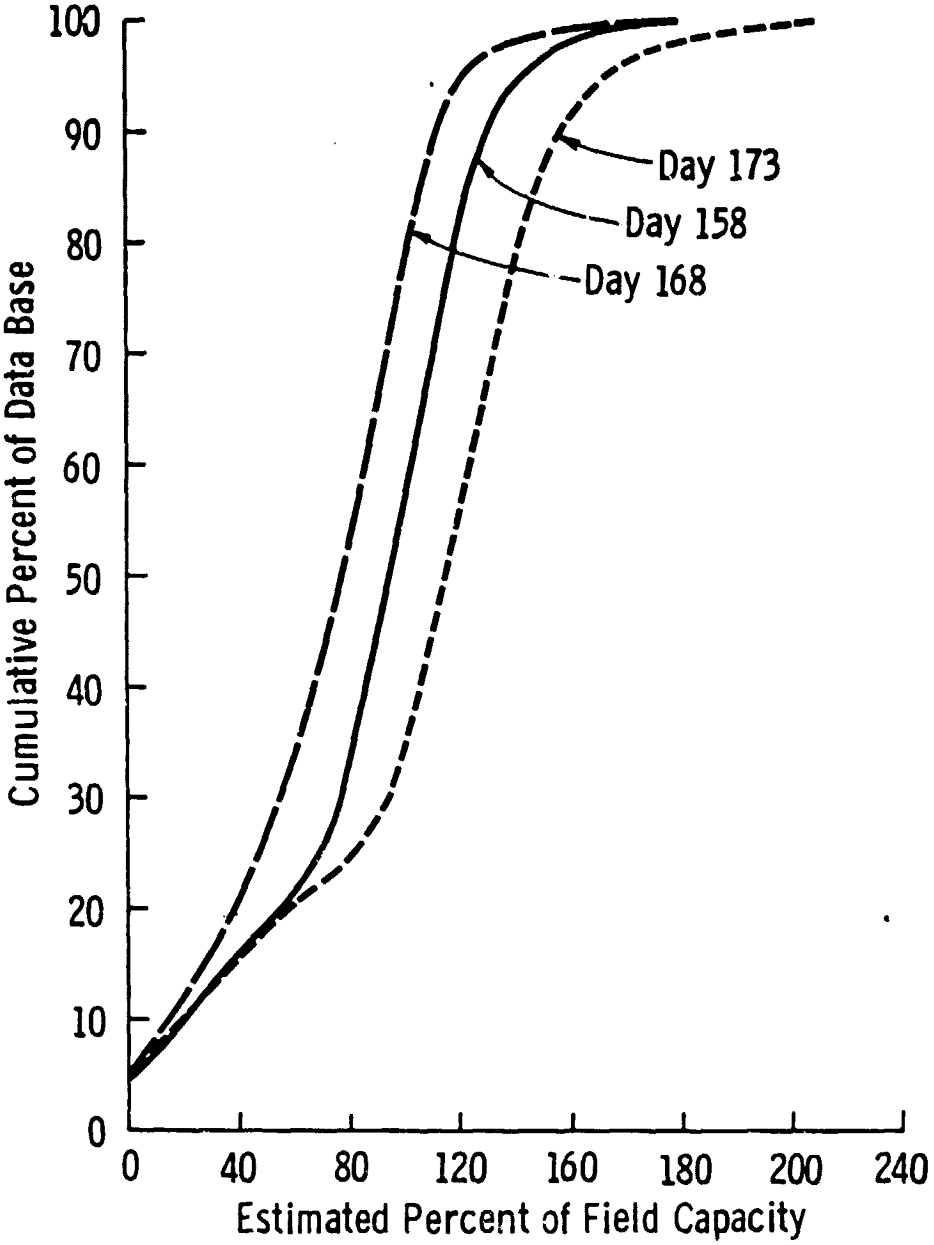

Figure 3.9. Distributions of 0-5 cm soil moisture estimated from 20 m resolution radar images (Case A) on Julian days 158, 168, and 173.

the number of grid cells classified as water doubles from 2.67% to 5.7% of the data base, reflecting the magnitude of local flooding within poorly drained fields.

The absolute difference between the estimated soil moisture $\hat{M}_{FC}$ predicted by Eq. 1.1 and the "actual" moisture M_{FC} as produced by SWAM on a given day is defined as estimate error E. The cumulative distribution of E as calculated for each 20-m x 20-m grid cell element is plotted versus the magnitude of E in Figures 3.10 to 3.13 for each simulated satellite overpass date. Thus, for a 20-m resolution SAR, Figure 3.10 shows that between 67% and 71% of all 20-m x 20-m grid cell elements (of 800,000 comparisons) have absolute estimate error E less than 30% depending on the overpass date. In Figure 3.10, the lack of a significant difference between overpass dates (moisture conditions) for E < 40% can be attributed to the compound impact of positioning errors (in matching $\hat{M}_{FC}$ to M_{FC} with a +/- 100-meter accuracy), the effects of local slope on radar moisture estimate, and the mechanics of the blind comparison procedure wherein the error function is derived from all 800,000 comparisons regardless of land-use class. In such a comparison, all grid cells containing non-agricultural or non-forest categories will have a large E by definition, since actual moisture is undefined for such categories (roads, buildings, water, etc.) and these kinds of categories comprise approximately 8% of the data base.

Perhaps a more realistic evaluation of radar soil moisture estimate accuracy is presented in Figure 3.11 for the same 20-m radar resolution and moisture conditions as those shown in Figure 3.10. In this case, all non-agricultural grid cell elements have been excluded from the calculation of the error distribution function. In addition,

ORIGINAL PAGE IS
OF POOR QUALITY

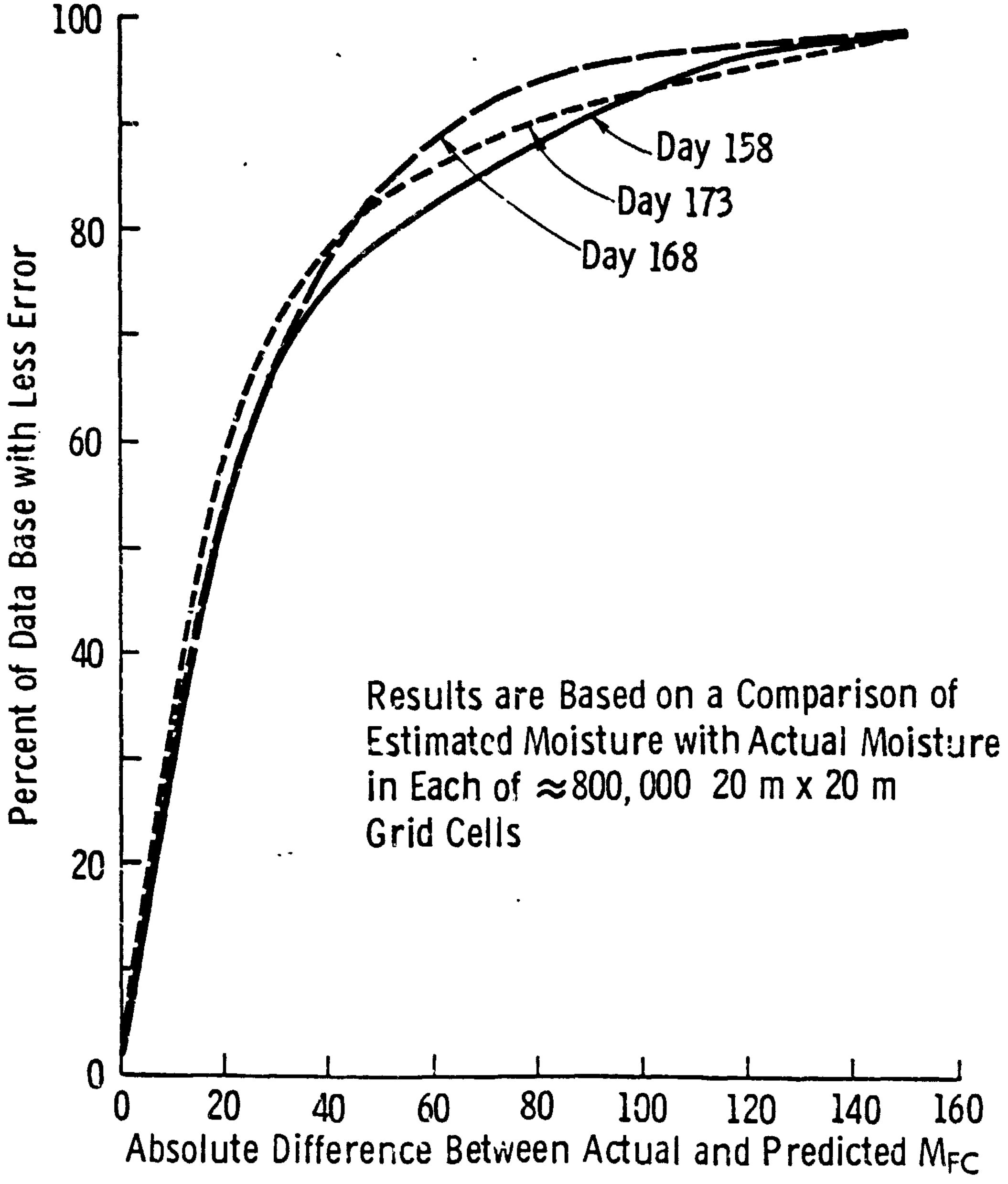

Figure 3.10. Soil moisture estimate accuracy for each overpass for radar with a 20 m resolution (Case A) when compared to mean 0-5 cm moisture present in 20 m x 20 m grid cells.

ORIGINAL PAGE IS
OF POOR QUALITY

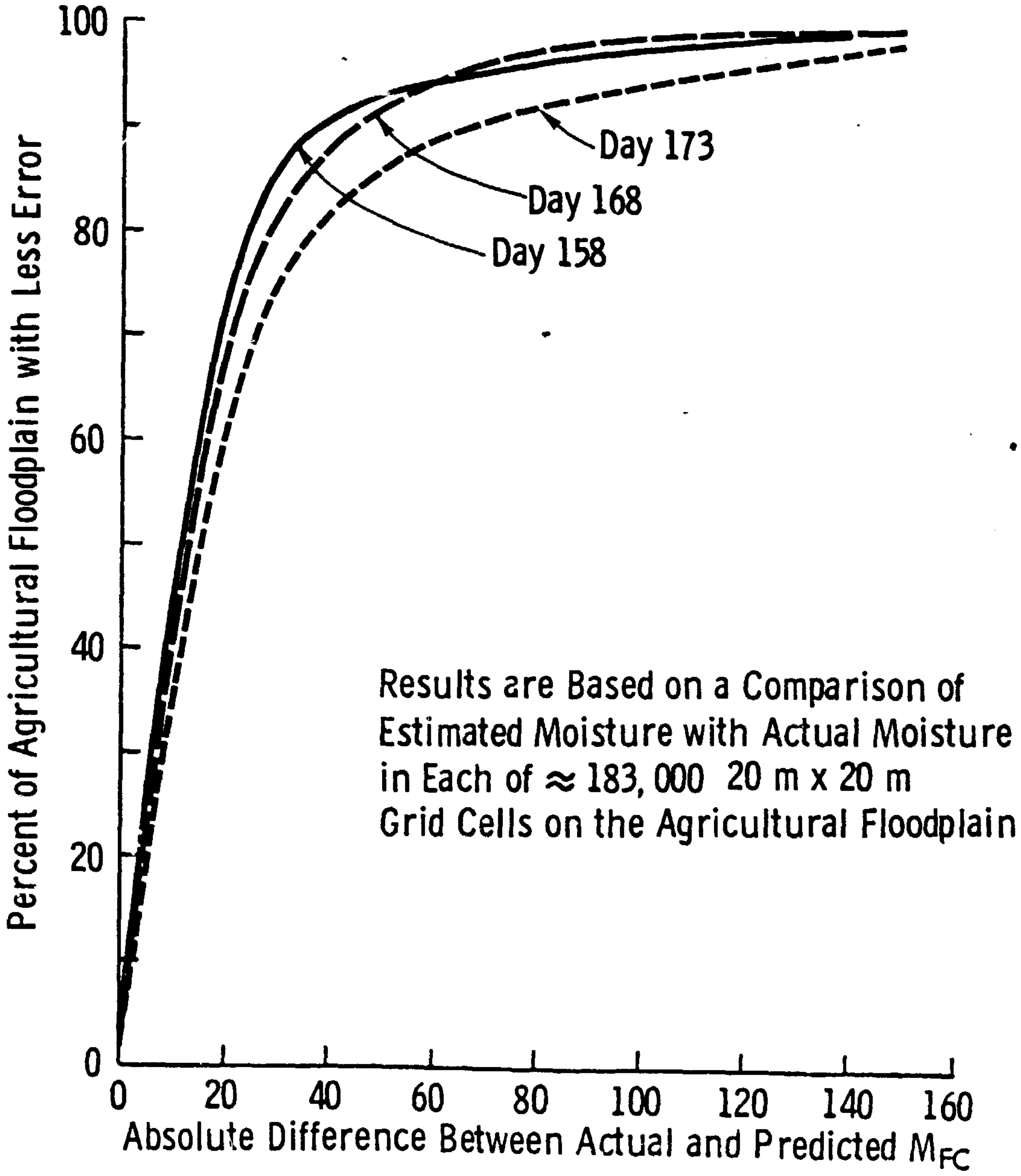

Figure 3.11. Soil moisture estimate accuracy for agricultural categories on the floodplain for each overpass of a simulated radar with 20 m resolution (Case A) when compared to mean 0-5 cm moisture present in 20 m x 20 m grid cells.

the comparison is limited to the relatively flat floodplain where mean registration error between M_{FC} and M_{FC} images is observed to be +/- 20 m. For the remaining 183,000 20-m x 20-m grid cell comparisons, between 75% and 86% have an absolute estimate error of $E < 30\%$. When expressed in terms of gravimetric moisture, an estimate error E of 30% corresponds to +/- 2.7%, +/- 7.3%, and +/- 9.2% for loamy sand, silt loam, and silty clay loam, respectively (Table 3.2).

Figures 3.12 and 3.13 show comparable results for the accuracy of soil moisture estimates using a 100-m resolution radar (System Case 4). The general level of the cumulative function shows that roughly 10% more 20-m x 20-m grid cells are correctly estimated for a given error threshold than can be correctly estimated from the 20-m resolution radar (System Case 2). This result confirms that found for the simplified, low spatial frequency moisture conditions obtained before the addition of SWAM [1,2] as shown in Figures 1.2 and 1.3.

In addition, the highest estimate accuracies are obtained for the intermediate moisture condition present on Julian day 158. This is most apparent in Figures 3.11 and 3.13 which consider only agricultural grid cells on the river floodplain. In both figures, the difference in cumulative percent between Julian days 158 and 168 is not statistically significant; however, estimate accuracy is shown to be considerably less for day 173. This is a consequence of the previously noted local saturation and partial flooding of some regions of the floodplain, with these areas apparently accounting for about 10% of the total region.

TABLE 3.2

Estimate Accuracy Levels: Comparison of Absolute Error in Percent of Field Capacity to Percent Gravimetric Moisture for Loamy Sand, Silt Loam, and Silty Clay Loam

± Estimate Accuracy in Percent			
	Gravimetric Moisture		
Field Capacity	Loamy Sand	Silt Loam	Silty Clay Loam
10%	0.9	2.4	3.1
20%	1.8	4.8	6.2
30%	2.7	7.3	9.2

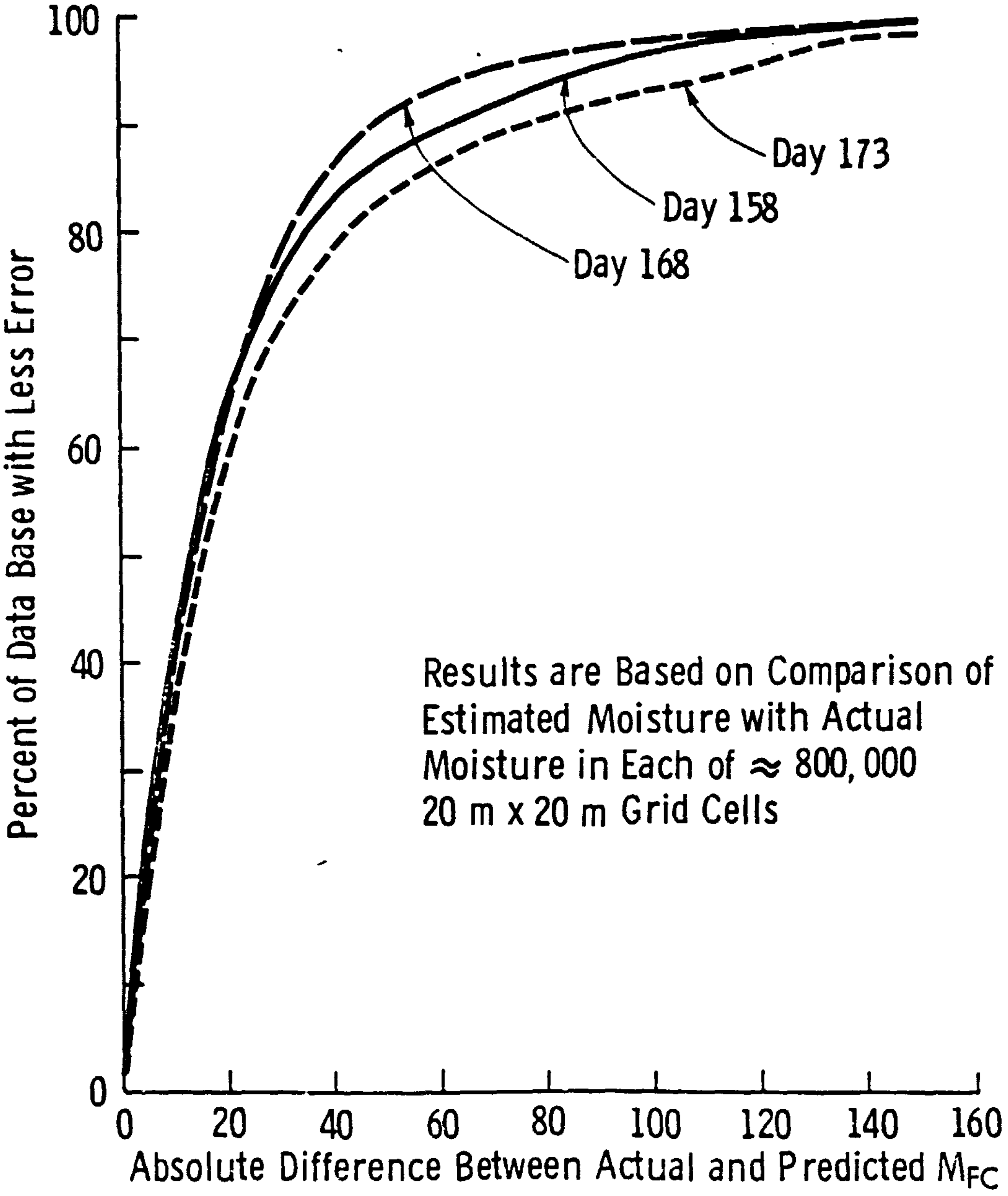

Figure 3.12. Soil moisture estimate accuracy for each overpass for a simulated radar with 1[illegible]m resolution (Case B) when compared to mean 0-5 cm moisture present in 20 m x 20 m grid cells.

ORIGINAL PAGE IS
OF POOR QUALITY

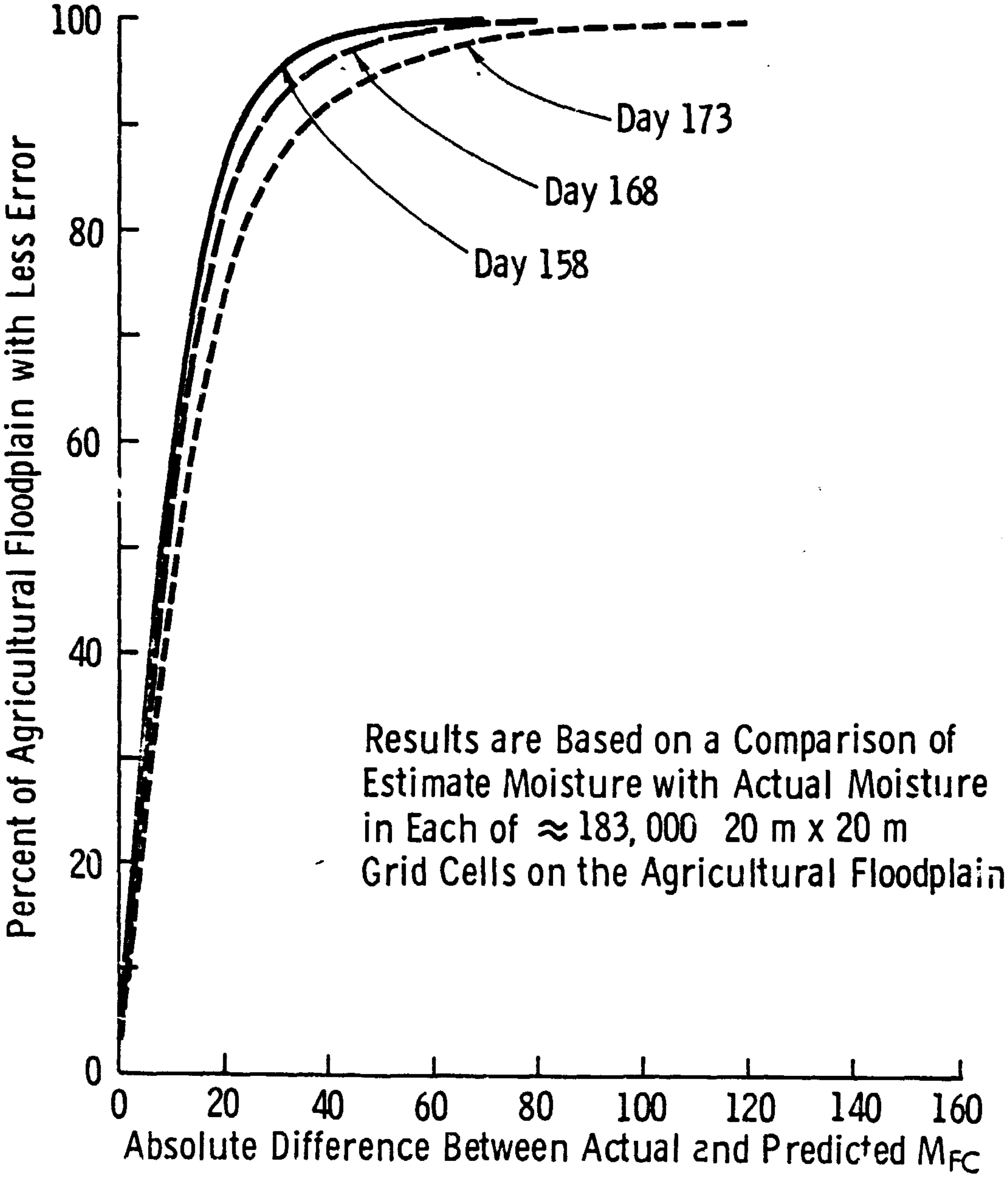

Figure 3.13. Soil moisture estimate accuracy for agricultural categories on the floodplain for each overpass of a simulated radar with 100 m resolution (Case B) when compared to mean 0-5 cm moisture present in 20 m x 20 m grid cells.

3.2 Impact of Radar Resolution and Estimate Resolution on Soil Moisture Estimate Accuracy

The simulation procedure allows the prediction of an estimated soil moisture $\hat{M}_{FC}$ for any desired grid-cell size from the radar imagery (even if the estimate is invariant over distances less than the sensor resolution). The result is two dimensionalities of resolution which can be evaluated with respect to estimate accuracy. The first considers only the effect of changing the radar resolution with respect to a fixed concept of the "ground-truthed" data base (actual M_{FC}) while the second considers the effects of changing the resolution of the moisture estimate to conform to a redefined actual moisture distribution (as averaged into larger effective grid cells -- 100 m x 100 m, 1 km x 1 km, or 3 km x 3 km).

When the soil moisture estimated from simulated radar imagery $\hat{M}_{FC}$ on Julian day 158 at radar resolutions of 20 m, 100 m, and 1 km is compared to the actual moisture M_{FC} from SWAM within each of 800,000 20-m x 20-m grid cells, the resultant error distribution functions are found to be those shown in Figure 3.14. The estimate error is shown to be the most tightly distributed around zero error for the 1-km resolution radar and most broadly distributed for the 20-m resolution radar.

The shapes of the distributions in Figure 3.14 also exhibit instructive trends. The finer resolution radars (20 m and 100 m) exhibit broad shoulders where soil moisture is underestimated; examination of the position of these errors reveals that they are spatially related to the shadowed, backslopes of steep hillsides and to the presence of deciduous trees (no penetration of deciduous trees is

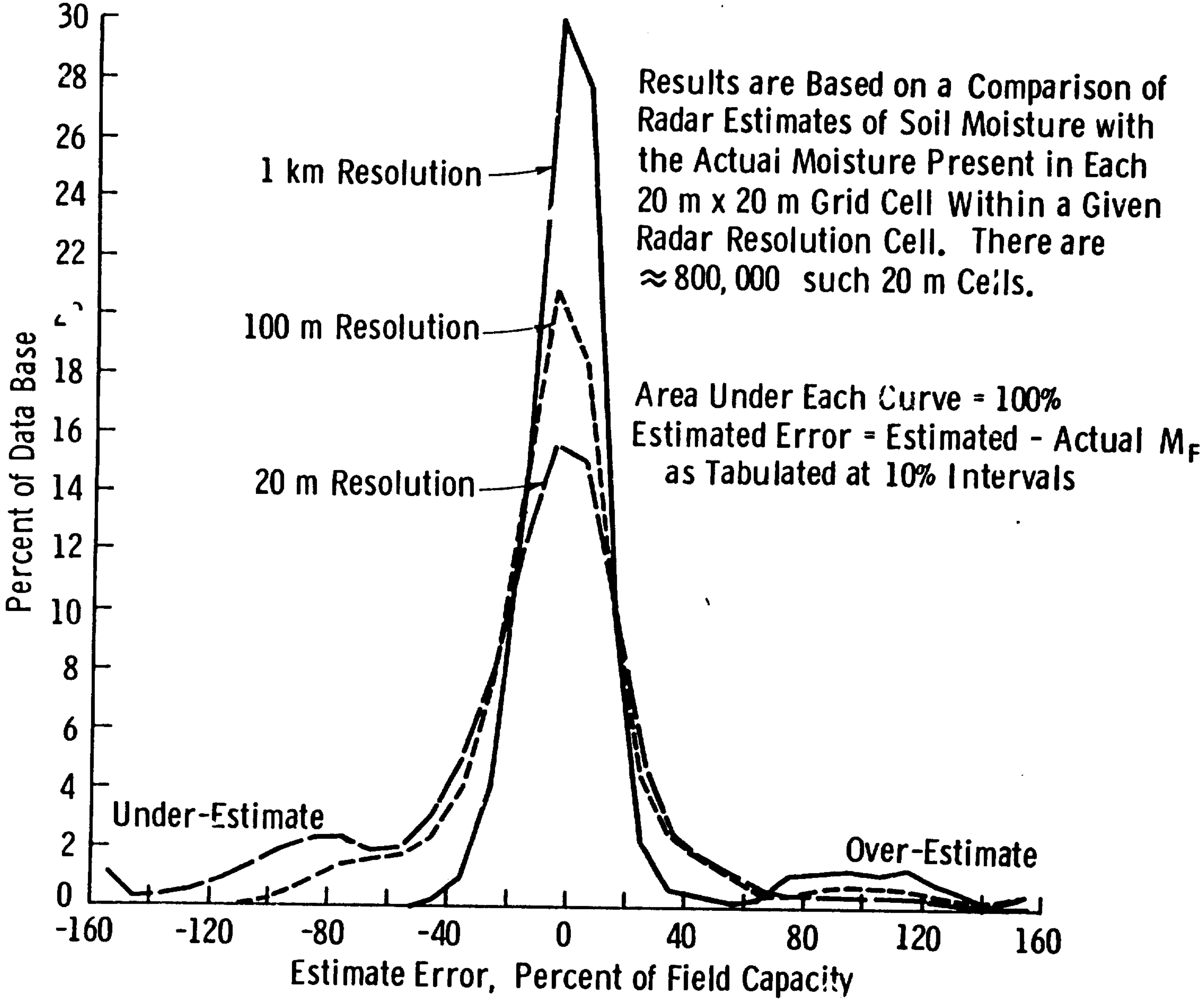

Figure 3.14. Soil moisture estimate error resulting from comparing moisture estimates on Julian day 150 from simulated radar with resolutions of 20 m, 100 m, and 1 km with mean 0-5 cm moisture in all 20 m x 20 m grid cells.

assumed for the target-sensor interaction model at 4.75 GHz in summer). These errors are not observed at the 1-km resolution, which reflects the fact that these target conditions (which result in a decrease of local σ^o) are generally much smaller than approximately 1 km^2 in extent. On the other hand, the 1-km-resolution radar yields a small, but broad, secondary maximum in the error distribution for an overestimate of soil moisture. This peak is related to the presence and distribution of point targets and cultural features, which behave in a fashion similar to corner reflectors and saturate the received signal. For a coarse resolution system, the impact of these targets is averaged over a correspondingly larger area and hence the estimate error attributed to such features includes more pixel elements than are occupied by the actual feature.

Thus, a reasonable conclusion is that adequate resolution for soil moisture sensing is limited, at the fine resolution end, by the size and slope distribution functions of hills and the size and shape distributions of woodland; and limited at coarse resolutions by the distribution functions of hard point targets which have a large radar cross-section.

The absolute error (distance from zero error in Figure 3.14) in the soil-moisture estimate as computed from 20-m x 20-m grid cell comparisons is shown for 20-m, 100-m, and 1-km radar resolutions in Figures 3.15 and 3.16 for the full data base containing 800,000 grid cells and the agricultural floodplain containing 183,000 grid cells, respectively. When compared to Figures 1.2 and 1.3, these figures show that the addition of within-field variance of soil moisture produces a negligible effect on the resultant error functions. The spatial

ORIGINAL PAGE IS
OF POOR QUALITY

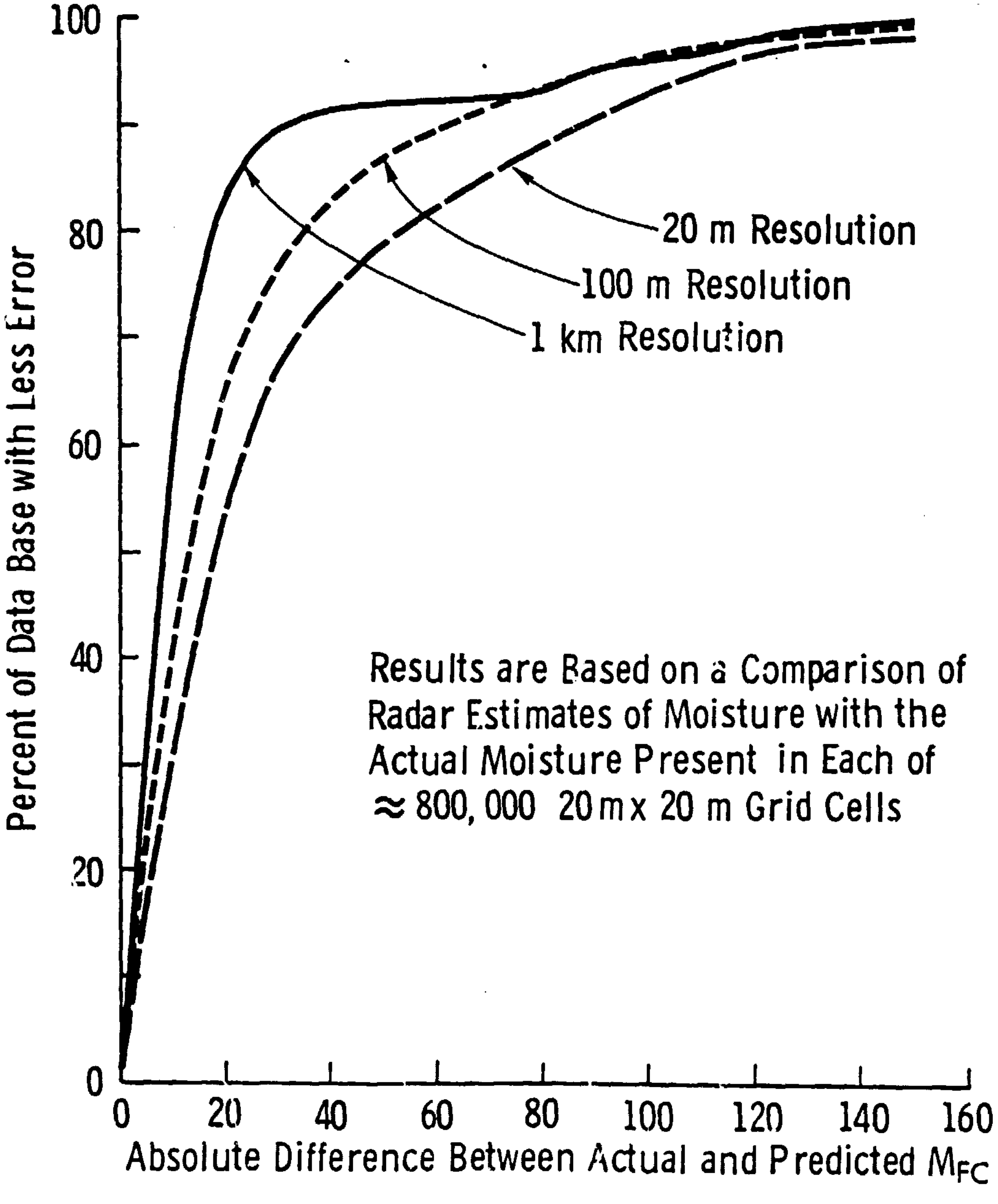

Figure 3.15. Soil moisture estimate accuracy for a satellite overpass on Julian day 158 for radar resolutions of 20 m, 100 m, and 1 km when compared to mean 0-5 cm moisture present in 20 m x 20 m grid cells.

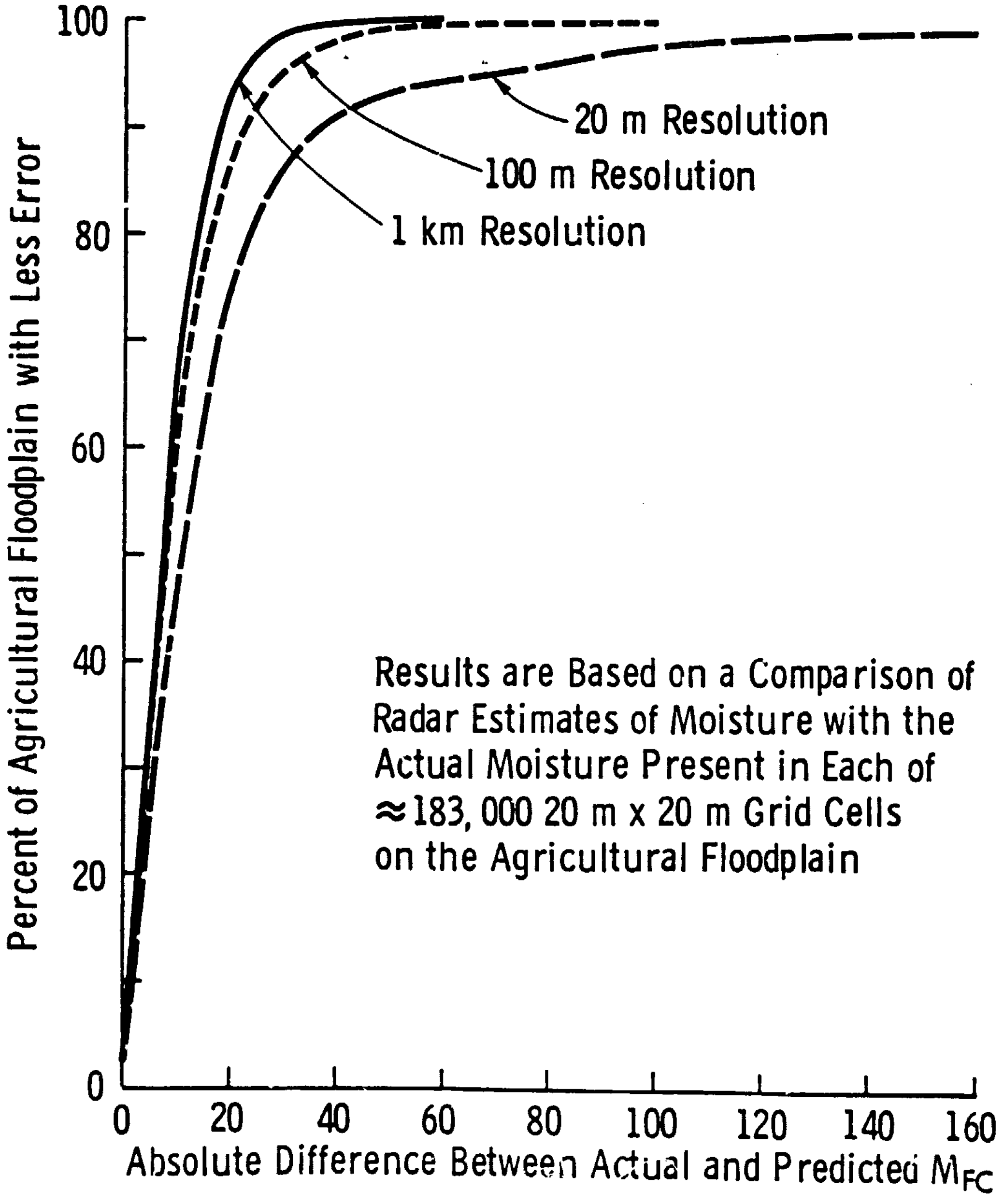

Figure 3.16. Soil moisture estimate accuracy for a satellite overpass on Julian day 150 for radar resolutions of 20 m, 100 m, and 1 km when compared to mean 0-5 cm soil moisture present in 20 m x 20 m grid cells.

averaging of the 100-m and 1-km resolution SAR is sufficient to offset the impact of the high-frequency spatial variability in M_{FC} (with a standard deviation of 6% around a zero mean). Furthermore, the effect of within-field variance in soil moisture is not discernable at a radar resolution of 20 m, even when considering only the 183,000 grid-cell comparisons on the agricultural floodplain in Figures 1.3 and 3.16. This may, however, be a spurious result due to the relative positioning accuracy of $\hat{M}_{FC}$ to M_{FC} on the order of +/- 20 m on the floodplain to +/- 100 m in hilly areas. In addition, the effects of signal fading at a 20-m radar resolution with 12 looks lead to a greater estimate uncertainty than that due to the local variance in soil moisture.

The above conclusions are also confirmed at a radar resolution of 3 km for the RAR system (Case 12 in Table 1.2). The cumulative percent of the total data base as a function of absolute estimate error is shown in Figure 3.17 from 100-m resolution SAR, 1-km resolution SAR, and 3-km resolution RAR; estimated moisture $\hat{M}_{FC}$ is compared to M_{FC} on a 100-m x 100-m grid cell basis. For the moderate soil moisture conditions prevailing on Julian day 158, the estimate accuracy of the 3-km system is effectively equivalent to that of the 1-km resolution system.

The effects of changing the grid-cell scale of the estimated soil moisture are shown in Figure 3.18. All results are for the 1-km resolution SAR on Julian day 158, the only difference being the effective resolution at which soil moisture prediction is being compared to the actual moisture distribution produced by SWAM. As the size of the comparison grid cell increases from 20 m x 20 m to 100 m x 100 m, the net estimate accuracy increases and the distribution becomes

ORIGINAL PAGE IS
OF POOR QUALITY

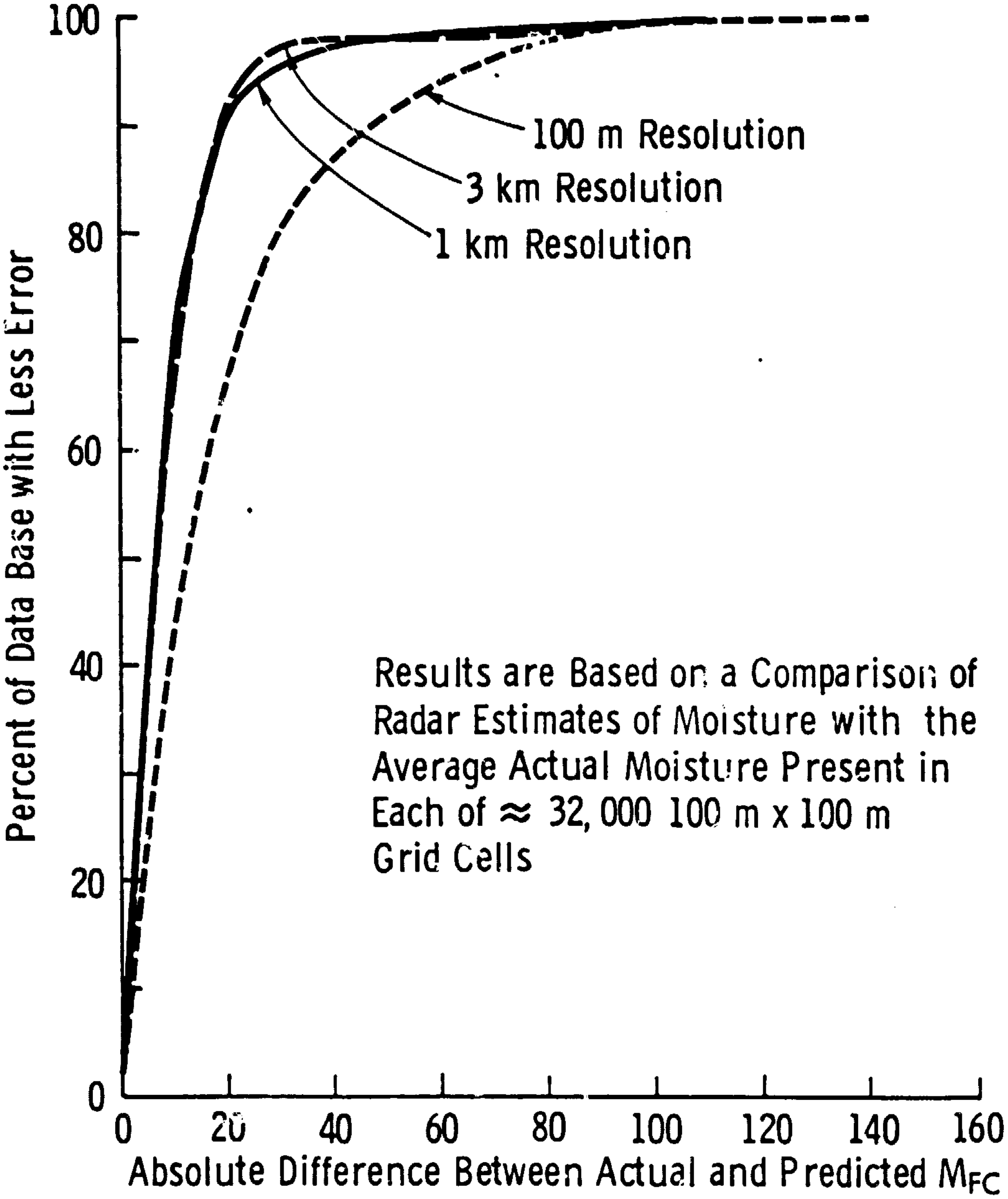

Figure 3.17. Soil moisture estimate accuracy for a satellite overpass on Julian day 158 for radar resolutions of 100 m, 1 km, and 3 km when compared to mean 0-5 cm moisture present in 100 m x 100 m grid cells.

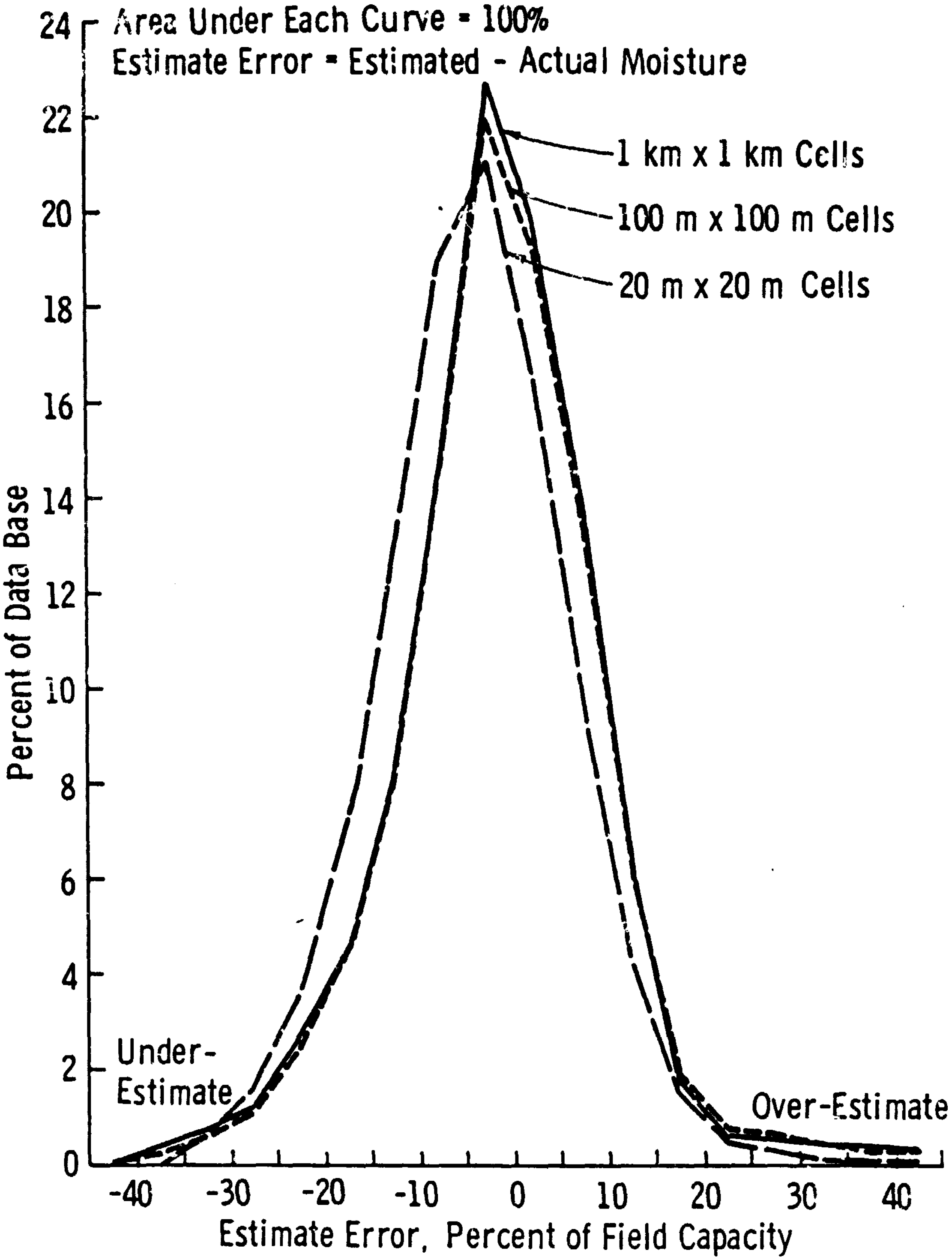

Figure 3.18. Soil moisture estimate error resulting from comparing that moisture estimated by a 1 km resolution radar on Julian day 158 (Case C1) to the mean 0-5 cm moisture present in 800,000 20 m x 20 m grid cells; in 32,000 10 m x 100 m grid cells; or in 325 1 km x 1 km grid cells.

less skewed with respect to zero estimate error. Further change in the distribution as comparison grid-cell size is increased from 100 m x 100 m to the sensor resolution size of 1 km x 1 km is in the same direction but is not significantly different in magnitude. The cumulative effect of changing the soil-moisture estimate scale is seen in Figure 3.19 for the same data as is plotted in Figure 3.18. Thus for a 1-km resolution radar, the most accurate estimate is obtained relative to the actual moisture distribution when estimated soil moisture is considered as applying to the mean moisture existent within grid cells no smaller than 100 m x 100 m. For the given spatial distributions of land cover classes in the data base, as representative of dry-land farming in east-central Kansas, the use of a 1-km resolution SAR to estimate moisture at a scale of 100 m x 100 m results in a loss in accuracy of only 1% to 3%, for a given acceptable error threshold as compared to using a 1-km x 1-km scale to estimate soil moisture.

In a statistical sense, this result is shown to be valid also for the 3-km RAR as shown in Figure 3.20. The reasons for this are not clear to the authors; however, it is felt to be related to the scales of natural variability in the constituent scene components. Agricultural fields have dimensionalities on the order of hundreds of meters, the magnitude of local slope varies over lateral dimensions of tens to hundreds of meters in the data base area, wooded areas within the data base have lateral extents that range from tens to hundreds of meters, mappable soil-type typically varies at scales of hundreds to thousands of meters. In response, near-surface soil moisture is observed to vary at all scales from millimeters to kilometers as controlled by the above conditions as well as microenvironmental

C-2

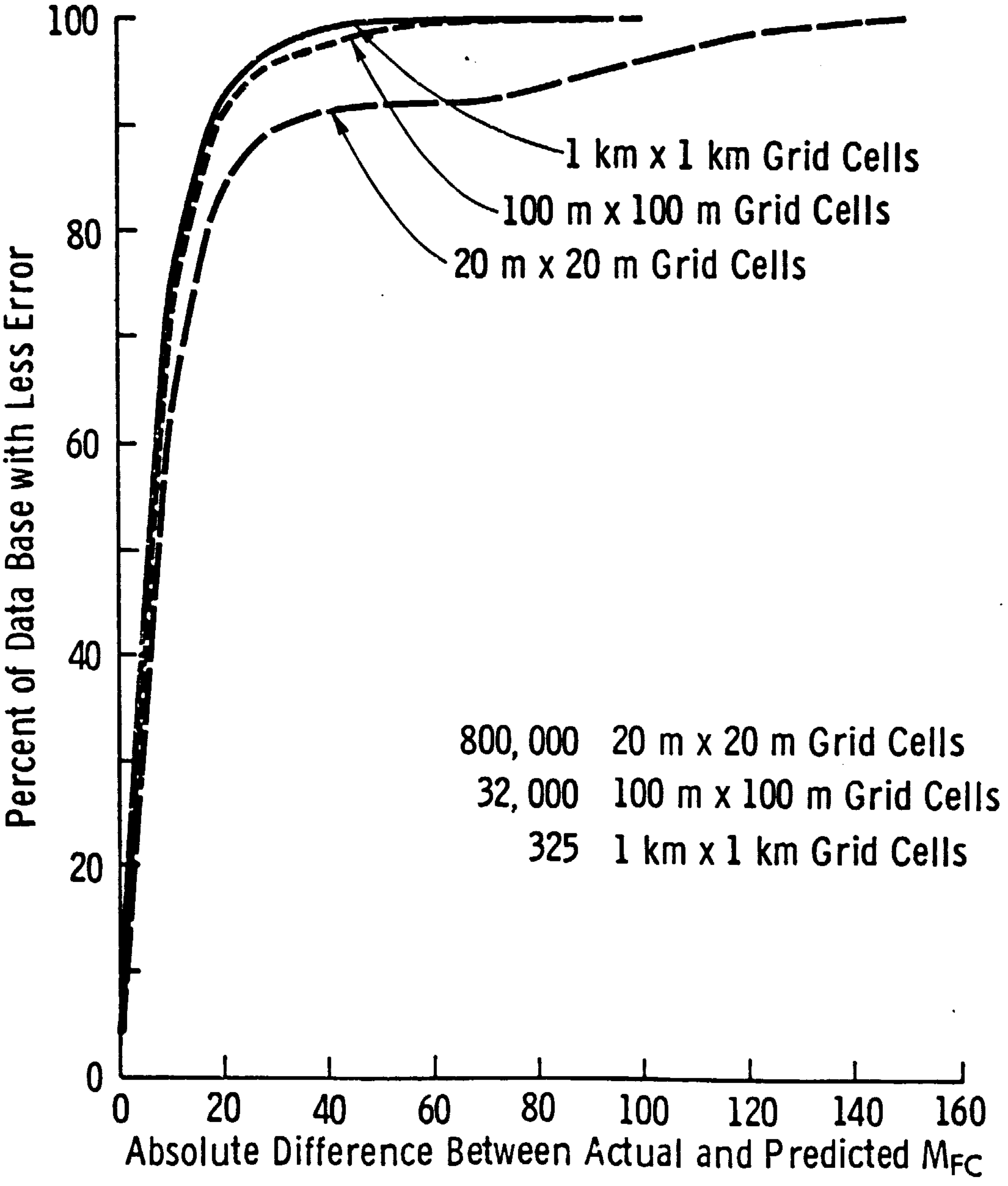

Figure 3.19. Cumulative effect on moisture estimate accuracy of changing the size of prediction grid cell from 20 m x 20 m to 1 km x 1 km for radar resolution of 1 km (Case C) on Julian day 158.

ORIGINAL PAGE IS
OF POOR QUALITY

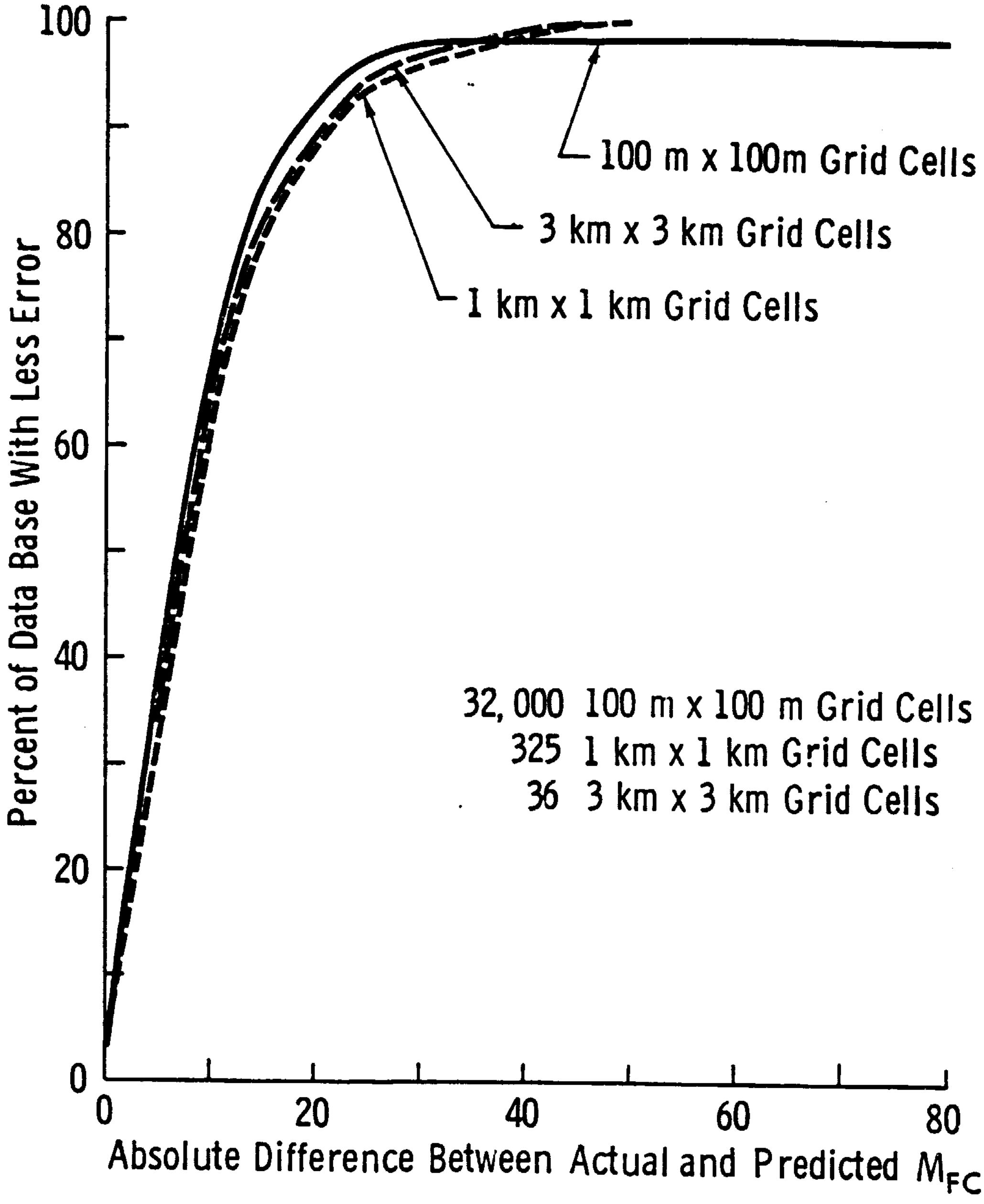

Figure 3.20. Effect on soil moisture estimate accuracy of changing the size of the prediction grid cell from 100 m x 100 m to 3 km x 3 km for a radar resolution of 3 km on Julian day 150 (Case D).

conditions such as surface roughness, shading, etc. (whose net effects are modeled as a random local variance with a standard deviation of 6% of field capacity).

3.3 Effects of Variance in Soil Moisture on Sensor Resolution

For any given area or moisture condition, the optimum sensor resolution appears to be the one that most closely matches the ground scale at which soil moisture becomes laterally decorrelated. When moisture is controlled largely by regional factors such as climatic events (rainfall) and soil-type distribution, the coarse resolution systems (1-km SAR and 3-km RAR) seem to provide optimal estimate accuracy. Within the closed system described by the simulation data base and according to the assumptions inherent in SWAM, this condition is well approximated by the saturated-to-very-moist soil conditions that can be expected to prevail for several days after a significant rainfall event. As time progresses, more localized environmental factors such as surface slope, crop type, and stage of growth play an increasingly significant role in controlling the spatial distribution of soil moisture; hence, the optimal sensor resolution for soil moisture mapping can be expected to be on the order of hundreds of meters.

Indeed, this is shown to be the case for this series of radar image simulations. Figure 3.21 shows that for the moderately moist to wet moisture conditions (M_{FC} from 85% to 120%) present on Julian day 158, the actual moisture conditions are most accurately reproduced by the coarsest resolution systems (1-km SAR and 3-km RAR) at the high end of the moisture range and by the 100-m resolution SAR over the median

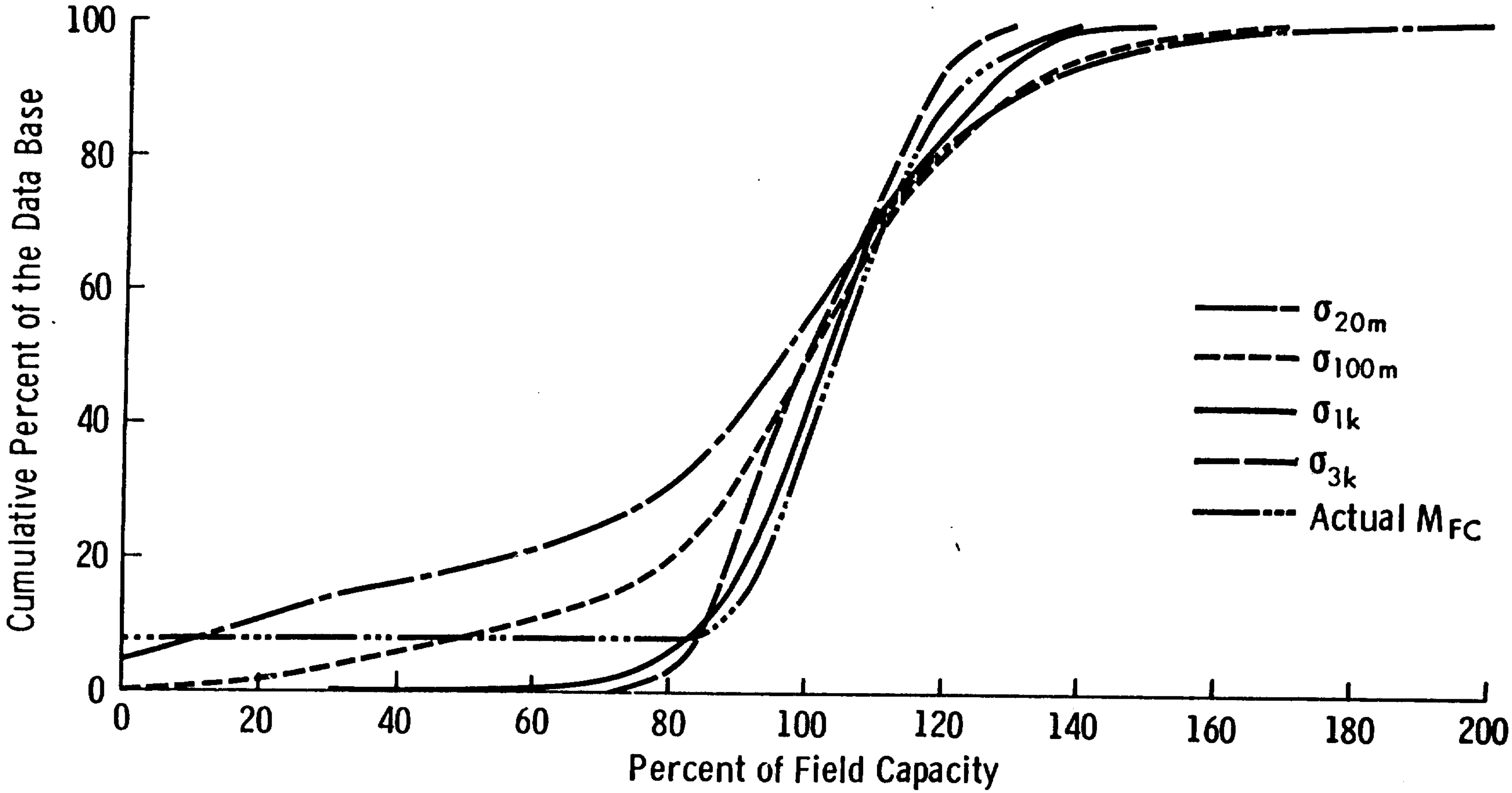

Figure 3.21. Comparison of actual percent of field capacity on Julian day 158 with that estimated from radar with resolutions of 20 m (Case A1), 100 m (Case B1), 1 km (Case C1), and 3 km (Case D1).

moisture range. The 20-m-resolution SAR is far too sensitive to local target-sensor interactions which introduce "noise" components into the resultant soil moisture estimate,and when combined with procedural problems in accurately registering the moisture estimate relative to the input M_{FC} distribution, yields the relatively lower estimate accuracy observed in Figures 3.14 to 3.16.

However, regardless of radar resolution, the impact of local within-field variability in soil moisture seems to have a negligible impact on soil moisture estimate accuracy. This apparently results from the fact that

- local within-field variance in soil moisture is normally distributed with a zero mean,
- Rayleigh fading is a larger source of local (20-m x 20-m) soil moisture estimate error for a small number of looks ($N < 23$), and
- other local effects (such as the presence of hills, canopy cover types, and row direction effects) are more significant sources of soil moisture estimate error from radar imagery.

4.0 CONCLUSIONS

The major conclusions of this study may be summarized as:

1) Local near-surface soil-moisture content was estimated with the greatest accuracy from radar imagery produced by systems with resolutions coarser than 100 m. Of the three such system configurations tested (100-m resolution SAR, 1-km resolution SAR, and 3-km resolution RAR) the optimal resolution was found to be linked to

the interaction between general soil moisture level and the spatial distributions of environmental factors controlling soil moisture dynamics. Thus, the coarsest resolutions (1 km and 3 km) performed best for very moist soil conditions where surface moisture content is primarily determined by soil type and drainage characteristics, while a sensor resolution of 100 m displayed equivalent or better moisture estimate accuracy during drying conditions as differential dry-down rates of various crop canopies introduced significant interfield variability into the soil-moisture distribution.

2) The effects on soil moisture estimate accuracy of high-frequency spatial variance in true soil moisture are negligible for radar resolutions of 100 m or larger if the variance is randomly distributed with a zero mean. For a radar resolution of 20 m with 12 looks, the uncertainty in moisture estimate as related to fading confidence interval is greater than that due to local target variability modeled as a Gaussian with a standard deviation of +/-6 percent of field capacity.

3) The upper limit of desirable resolution should be bounded by considerations of field-size distribution for a given agronomic region, the soil moisture range of interest for a specific application, and the spatial density of non-distributed targets with a large radar cross-section. Thus, the radar resolution cell should be less than the modal agricultural field size of interest, and small enough to allow the discrimination of point targets as sources of soil-moisture estimate error (especially for dry soil-moisture conditions).

The significance of the above conclusions is, of course, limited by the authenticity of the closed system described by the dynamic environmental model, the static terrain model, the target-sensor interaction model, the radar image formation process, and the evaluation procedures applied to the resultant images. The static terrain model is certainly appropriate for the simulated area, except that the inclusion of certain types of scattered point targets is somewhat arbitrary at a 20-m x 20-m grid-cell size. The dynamic soil water accounting model, while not rigorous, correctly predicts the direction and gross magnitude of changes in near-surface soil moisture. The radar backscatter models have been found to be statistically accurate descriptors of mean conditions; the explicit addition of crop growth stage to backscattering models is a planned improvement that will require more detailed empirical evidence as well as a better theoretical understanding of the impact of crop phenology on scattering and absoprtion. The image formation models have been found to be quite good for side-looking airborne and orbital radar, which incorporate Rayleigh fading statistics for images containing a small number of independent samples [26,27].

Thus, the results are expected to represent fairly the conditions applied. It is, however, recommended that the geographic extensibility of these conclusions be tested for a larger or geographically dissimilar data-base, especially with respect to these conditions.

- agricultural field-size distributions with mean field-size larger and/or smaller than that modeled,
- more intricate spatial distribution of agricultural fields and woodlands such as those characteristic of agronomic areas in the more humid eastern half of the United States and Europe,
- denser spatial distributions of cultural features and point targets characteristic of more densely populated yet

agriculturally significant regions.

Also, given the apparent adequacy of coarse-resolution radar systems with low power requirements, consideration should be given to modeling both a cross-polarized system and a combined radar/radiometer system for purposes of estimating soil moisture.

REFERENCES

[1] Ulaby, F. T., M. C. Dobson, J. Stiles, R. K. Moore, and J. Holtzman, "A Simulation Study of Soil Moisture Estimation by a Space SAR," Photo. Eng. and Rem. Sens., Vol. 48, No. 4, pp. 645-660, April 1982.

[2] Ulaby, F. T., J. Stiles, M. C. Dobson, J. Holtzman, and R. K. Moore, "Simulation of Space Radar Imagery for Soil Moisture," RSL Technical Report 429-1, University of Kansas Center for Research, Inc., Lawrence, Kansas, February, 1981.

[3] Peck, A. J., R. J. Luxmoore, and J. L. Stolzy, "Effects of Spatial Variability of Soil Hydraulic Properties in Water Budget Modeling," Water Resources Research, Vol. 13, No. 2, pp. 348-354, April, 1977.

[4] Peak, A. J., R. McQuivey, T. Keefer, E. R. Johnson, and J. Erekson, "Review of Hydrologic Models for Evaluating Use of Remote Sensing Capabilities," NASA CR 166674, Hydrex Corp., Fairfax, Virginia, March, 1981.

[5] Hildreth, W. W., "Comparison of the Characteristics of Soil Water Profile Models," NASA - 15800, Lockheed Eng. and Management Services Co., Inc., January, 1981.

[6] Jackson, R. D., "On the Calculation of Hydraulic Conductivity," Soil Sci. Soc. Amer. Proc., Vol. 36, pp. 380-382, 1972.

[7] Armstrong, B. L., "Derivation of Initial Soil Moisture Accounting Parameters from Soil Properties for the National Weather Service River Forecase System," NOA Technical Memorandum NWS HYDRO 37, National Weather Service, March, 1978.

[8] Doorenbos, J., and W. O. Pruitt, "Guidelines for Predicting Crop Water Requirements," FAO Irrigation and Drainage Paper 24, United Nations Food and Agriculture Organization, 1977.

[9] Mignogno, M. J., C. E. Duchon, A. G. Eddy, and A. D. Nicks, "An Investigation of the Dependence of Mesoscale Rainfall Parameters on Pixel Size," University of Oklahoma School of Meteorology, June, 1980.

[10] Harcy, K. R., S. H. Cohen, L. K. Rogers, H. K. Burke, R. C. Leupold, and M. D. Smallwood, "An Evaluation of the Spatial Resolution of Soil Moisture Information," ERT Doc. No. P-7505-F, Envir. Res. and Tech., Inc., Concord, Mass., March, 1981.

[11] Nicks, A. D., and M. A. Hartman, "Variation of Rainfall Over a Large Gauged Area," *Trans. of ASAE*, Vol. 9, pp. 437-439, 1966.

[12] Huff, F. A., and W. L. Shipp, "Spatial Correlations of Storms, Monthly and Seasonal Precipitation," *J. Applied Met.*, Vol. 8, pp. 542-550, 1969.

[13] Eagleman, J. R., "An Experimentally Derived Model for Actual Evapotranspiration," *Agr. Met.*, Vol. 8, pp. 385-394, 1971.

[14] Burkhead, C. E., R. C. Max, R. B. Karnes, and E. Reid, "Usual Planting and Harvesting Dates," Agr. Handbook No. 283, USDA Statistical Reporting Service, March, 1972.

[15] Hodges, T., "U.S. Crop Calendars in Support of the Early Warning Project," LEMSCO-14674, Lockheed Eng. and Management Services Co., Inc., July, 1981.

[16] Bradley, G. A., and F. T. Ulaby, "Aircraft Radar Response to Soil Moisture," RSL Technical Report 460-2, University of Kansas Center for Research, Inc., Lawrence, Kansas, October, 1980.

[17] Hills, R. C., and S. G. Reynolds, "Illustrations of Soil Moisture Variability in Selected Areas and Plots of Different Sizes," *J. of Hydrology*, Vol. 8, pp. 27, 1969.

[18] Bell, K. R., T. J. Schmugge, B. J. Blanchard, and M. W. Witczak, "Analysis of Surface Moisture Variations Within Large Field Sites," *Water Resources Research*, Vol. 16, No. 4, p. 796, 1980.

[19] Nielson, D. R., J. W. Biggar, and K. T. Erh, "Spatial Variability of Field Measured Soil Properties," *Hilgardia*, Vol. 42, No. 7, p. 215, 1973.

[20] Hawley, M. E., R. H. McCuen, and T. J. Jackson, "Volume-Accuracy Relationship in Soil Moisture Sampling," *Proc. Amer. Soc. Civ. Eng.*, Vol. 108, No. IR1, pp. 16933, 1982.

[21] United States Department of Agriculture, "Irrigation Water Requirements," Technical Release No. 21, USDA/SCS, September, 1970.

[22] Milstead, B. W., "Agricultural Soil Moisture Experiment: 1978 Colby (Kansas); Data Catalog and Documentation," NASA/JSC Technical Report JSC-16229, September, 1979.

[23] Richter, J., and J. F. Paris, "Preliminary Results of the Colby Agricultural Soil Moisture Experiment Scatterometer Data Analysis," Soil Moisture Workshop, Minutes of the Quarterly Technical Interchange Meeting, April 26-30, 1982, NASA/JSC.

[24] Batlivala, P. P., and F. T. Ulaby, "Feasibility of Monitoring Soil Moisture Using Active Microwave Remote Sensing," RSL Technical Report 264-12, University of Kansas Center for Research, Inc., Lawrence, Kansas, January, 1977.

[25] Dobson, M. C., and F. T. Ulaby, "Soil Textural Effects on Radar Response to Soil Moisture," RSL Technical Report 264-30, University of Kansas Center for Research, Inc., Lawrence, Kansas, October, 1979.

[26] Holtzman, J. C., V. S. Frost, J. L. Abbott, and V. H. Kaupp, "Radar Image Simulation," IEEE Trans. Geo. Elect., Vol. GE-16, No. 5, pp. 296-303, October, 1978.

[27] Stiles, J. A., V. S. Frost, J. C. Holtzman, and K. S. Shanmugam, "The Recognition of Extended Targets: SAR Images for Level and Hilly Terrain," IEEE Trans. Geo. and Rem. Sens., Vol. GE-20, No. 2, April, 1982.